Thermoelectric properties of Thallium Lanthanoid Tellurides, $Tl_{10-x}Ln_xTe_6$, $0.25 \leq x \leq 1.32$, Ln = La, Ce, Pr, Nd, Sm, Gd, Tb, Dy, Ho and Er

by

Savitree Bangarigadu-Sanasy

A thesis

presented to the University of Waterloo

in fulfillment of the

thesis requirement for the degree of

Doctor of Philosophy

in

Chemistry

Waterloo, Ontario, Canada, 2012

AUTHOR'S DECLARATION

I hereby declare that I am the sole author of this thesis. This is a true copy of the thesis, including any required final revisions, as accepted by my examiners.

I understand that my thesis may be made electronically available to the public.

Signature:

Abstract

Thermoelectrics can convert heat energy into electrical energy (Seebeck effect) and vice-versa (Peltier effect) without any sort of pollution. That is because there are no moving parts that can cause noise pollution and no liberation of gas or chemical residue that could degrade the environment. On the contrary, application of the thermoelectric concept will help to deal with two main global issues, the increasing demand for energy with all the developments (increasing number of vehicles on the road, construction of more building, urbanisation of rural areas in developing countries etc.) and the drastic climate changes which are a result of those developments. The application of thermoelectrics in Peltier coolers has already helped to decrease the ozone depletion problem by replacing the CFC's in the refrigerators.

The Seebeck effect could help fulfil the increasing global demand for fuel and decrease significantly greenhouse gases if applied to exhaust systems of vehicles to convert the lost heat energy into useful electricity. The efficiency of thermoelectrics depends on the dimensionless figure of merit, ZT ($ZT = T S^2\sigma/\kappa$, T = temperature, S = Seebeck coefficient, σ = electrical conductivity, κ = thermal conductivity); the higher the ZT value, the higher will be the efficiency. The best suited materials for thermoelectric are semiconductors as they have a compromised high S and high σ, however, κ depends on the materials themselves, some have low κ and some have high. Lots of research has been done on reduction of κ of semiconductors with good electronic properties.

This research is about investigating the structure and the thermoelectric properties of thallium lanthanoid tellurides. Thallium lanthanoid tellurides might be promising thermoelectrics exhibiting small κ, as selected thallium-based tellurides have outstanding properties. The ZT values of both Tl_9AgTe_5 and Tl_9BiTe_6 are 1.2 at 700 K and 500 K respectively; the state-of-the-art thermoelectric materials, SiGe, Bi_2Te_3 and LAST have a ZT value of ~ 0.5 at temperatures greater than 900 K, 0.6 at RT and ~ 1.7 at 700 K respectively. The low κ of ~ 0.4 W/(mK) is responsible for the good ZT value of Tl_9BiTe_6 and Tl_9AgTe_5. However, thallium based semiconductors might never be commercialized due to the toxicity of Tl element. Nevertheless, from a scientific point of

view, the study of the thallium lanthoid tellurides, $Tl_{10-x}Ln_xTe_6$, will still contribute in understanding the relation between the structure, stoichiometry and the properties of these thallium based semiconductors.

In the present study, thallium lanthanide tellurides, $Tl_{10-x}Ln_xTe_6$, Ln = La, Nd, Gd, Tb, Dy, Ho, Er; $0.25 \leq x \leq 1.32$ are investigated. All the thallium lanthanoid tellurides are isostructural to Tl_9BiTe_6, adopting the space group *I4/mcm* with mixed occupancy of Tl^+/Ln^{3+} at the *4c* site. Substitution of Tl by Ln at the *4c* site in the $Tl_{10}Te_6$ structure, changes the lattice parameters and unit cell volume of the compounds as expected. The unit cell volume increases as the lanthanide content increases within a particular phase (more of the f-block Ln elements incorporated in the structure) and decreases across the lanthanides series for a specific stoichiometry (across the Ln series, atomic size decreases due to lanthanide contraction). Thermoelectric property measurements on sintered pellet showed that the Seebeck coefficient, *S*, increase as the lanthanide content increases for a particular phase (carrier concentration in the compound decreases as more Ln is incorporated). On the other hand, electrical conductivity, σ, (due to decrease in carrier concentration) and thermal conductivity, κ, (due to decrease in carrier concentration, increase in mass fluctuation and lattice vibration) decrease as the lanthanide content increase. The opposite trend is true for $Tl_{10-x}Ln_xTe_6$, $x \approx 1$, across the lanthanide series, S decreases whereas σ and κ increase. Consequently, the dimensionless figures of merit increase within a particular phase but decreases across the lanthanide series, the highest *ZT* value of ~ 0.20 was obtained for Tl_9LaTe_6 and $Tl_{8.98}Nd_{1.02(6)}Te_6$ at 553 K.

Moreover, thermoelectric properties were studied on a hot-pressed pellet of Tl_9LaTe_6. The Seebeck coefficient for the cold-pressed and the hot-pressed pellets were almost same for the whole temperature range studied. A slight increase in the σ values for hot-pressed compared to the data of the sintered pellet was observed for the same temperature range. Similarly, κ values for the hot-pressed pellet were higher that of the cold-pressed pellet. The higher electrical and thermal conductivity of the hot pressed pellet with respect to the sintered pellet is due to improved compactness. The highest *ZT* for the hot-pressed pellet was ~ 0.32 around 555 K.

The second part of the project was to study the thermoelectric and magnetic properties on the Ce, Sm and Pr compounds of the $Tl_{10-x}Ln_xTe_6$ family. The thermoelectric properties of those compounds with temperature were in agreement to the observations made for other compounds studied in this thesis. As temperature increases, S increases while σ decreases, κ was basically temperature independent as for the rest of this study. However, the study of the thermoelectric properties of compounds of Ce, Pr and Sm phases did not correlate with the rest of the thallium lanthanoid tellurides both within the phases and across the lanthanide series.

The unit cell volume of Tl_9CeTe_6 was found to be unexpectedly smaller compared to the general decreasing tend ain the unit cell volume of Tl_9LnTe_6, across the Ln series. On the contrary, the unit cell volume of Tl_9PrTe_6 was found to be unexpectedly bigger compared to the general decreasing tend in the unit cell volume of Tl_9LnTe_6, across the Ln series. The physical properties of Tl_9CeTe_6 and Tl_9PrTe_6 compounds were anomalous as well, with respect to the rest of the Tl_9LnTe_6 series. There is a general increase in S from Tl_9CeTe_6 to Tl_9SmTe_6 compounds instead of a decreasing trend. Instead of an increasing tendency in the σ and κ values across the Tl_9LnTe_6 series, both parameters decrease from Tl_9CeTe_6 to Tl_9SmTe_6. Curie-Weiss Law and Modified Curie-Weiss Law were applied to their magnetic property measurement data. The magnetic property measurements revealed a magnetic moment of 2.02 μ_{eff}/μ_B for Tl_9CeTe_6 which is lower than the expected value of 2.54 μ_{eff}/μ_B. This points out towards the possibility of some Ce^{4+} in the structure unlike the Tl_9PrTe_6 compounds which had only Pr^{3+} ion in the structure. The magnetic data of Tl_9SmTe_6 was not conclusive as there was a temperature dependence of the magnetic field.

This study therefore reveals that the thallium lanthanoid tellurides, $Tl_{10-x}Ln_xTe_6$, $0.25 \leq x \leq 1.32$, Ln = La, Ce, Pr, Nd, Sm, Gd, Tb, Dy, Ho and Er, do have low κ (< 3 W/(mK)), especially when $x \sim 1$ ($\kappa < 0.5$ W/(mK)). The best ZT of this series is ~ 0.20 around 550 K exhibited by Tl_9LnTe_6, Ln = La, Nd, Sm compounds. The hot-pressed sample of Tl_9LaTe_6 exhibited a ZT value of ~0.32 in the around 550 K.

Acknowledgements

Firstly, I would like to sincerely thank to my supervisor, Professor Kleinke for his invaluable help and guidance throughout the making of this work during the past four years. Moreover, I wish to express my deep appreciation to him for his critical reading of the manuscript.

I express my gratefulness and thanks to my husband, Rishi, for his precious support and my daughter, Maansi, for her love and understanding. I also thank GOD for his blessings and for giving me this opportunity.

Many thanks to all the past and present members of Kleinke group for their support and guidance namely Jackie, Yangie, Annie, Mariya, Mykhailo, Maya, Raj, Bryan, Tingting, Donghee, Susan and Nagraj.

Special thanks to our crystallographer Dr. Abdeljalil Assoud for his priceless advice, guidance and friendship, our research associate Katja for always being there when we needed her and our exchange students Philipp and Anna for Germany for their help in this work.

Furthermore, I thank Tim Holgate and Professor Tritt for helping us with the hot-pressing of the Tl_9LaTe_6 sample. I wish to express my deepest gratitude to Professor Greedan and Paul for their help and guidance with the magnetic properties.

Last but not the least, I wish to express my sincere gratitude and thanks to my advisory committee members, Professor Nazar, Professor Radovanovic and Professor Soldatov for their expert comments and suggestions during the four years of my Ph.D study. Moreover, I sincerely appreciate my external examiner Professor Brock and internal-external examiner Professor Gu for their precious time to review my thesis and attend my defence.

Table of Contents

List of Figures

List of Tables

List of Schemes

1 THERMOELECTRICS

In the past years, the global energy consumption has increased continuously, in 2004 by 4.4% and in 2005 by 2.7%.[1] It is predicted that the growth in energy consumption would continue steadily as it has over the last two decades.[2] Another global issue related to the increasing energy consumption is the global warming.[2] The global reserve of non-renewable energy resources is limited, there is probably sufficient oil and gas for this century and coal for approximately two centuries.[1] Therefore, it is really important to look into alternate energy sources, especially cleaner forms of energy, to be able to deal with the problematic climate changes.[3] Thermoelectrics might help in this critical global situation as thermoelectric materials convert heat energy to electrical energy and vice versa without causing any pollution. It has already helped in the ozone depletion problem due to the fact that CFC's as thermoelectric coolers have replaced the compression system in refrigerators.[4] The thermoelectric phenomenon was discovered in the 19th century but its application became possible only after mid-20th century due to the poor efficiency of the thermoelectric materials in the early stage of the discovery.[5] Future development in this field would be utilisation of waste heat from industries and exhaust fumes in form of electrical energy; in industries, 30%[3] and in automotives, 40%[6] of the primary gasoline fuel energy are dissipated as waste heat energy. However, the challenges in the future developments in this field would be

- finding better performing low cost thermoelectric materials that could be used at higher temperatures for conversion of energy from various industrial heat sources.[3]
- develop novel thermoelectric materials and tune the various parameters involved in their performance to improve their efficiency.[3]

1.1 Introduction to the thermoelectric concept

Thermoelectric technology is basically an energy conversion technology whereby heat energy is converted to electrical energy and vice versa.[7-9] The conversion of heat energy to electrical energy was discovered by Thomas Johann Seebeck in 1821[8, 10] when he noticed the deflection of a compass needle that was near a closed loop formed from

two dissimilar metals and the junctions of the loop were at two different temperatures. Therefore this phenomenon is called the Seebeck effect (*Figure 1.1(a)*). The reverse effect is called the Peltier effect (*Figure 1.1(b)*); it was discovered by Jean Charles Peltier in 1834[8, 10] when he observed temperature changes in the vicinity of the junction between two dissimilar conductors upon passage of an electric current.

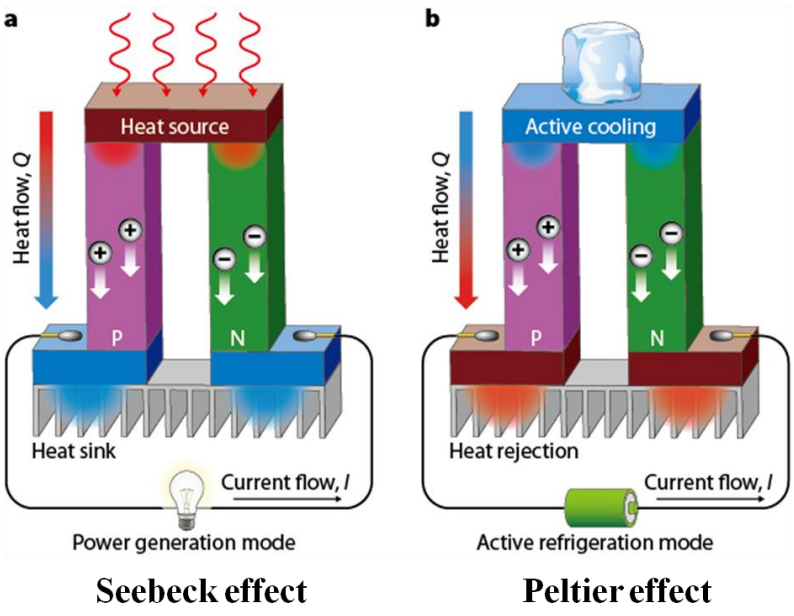

Figure 1.1[9]: (a) Power Generation through the Seebeck Effect (b) Refrigeration through the Peltier Effect

In *Figure 1.1*, P and N are *p*-type and *n*-type semiconductors respectively; they are responsible for the energy conversion and such materials are called thermoelectric materials. When used for the Peltier effect, devices are called thermoelectric coolers (TEC) and when used for the Seebeck effect, devices are called thermoelectric power generators (TEG). Commercial applications of these phenomena are made through thermoelectric module. A thermoelectric module consists of a number of thermocouples[3] (*Figure 1.2*) connected in series electrically and in parallel thermally When the module is connected in a complete circuit, at one side heat rejection occurs and at the opposite side heat absorption occurs as shown in *Figure 1.2*. The output voltage of TEG is proportional to the number of thermocouples and the temperature difference between the

cold and hot side, however, the efficiency depends on the materials (the *p*-type and *n*-type semiconductor).[3]

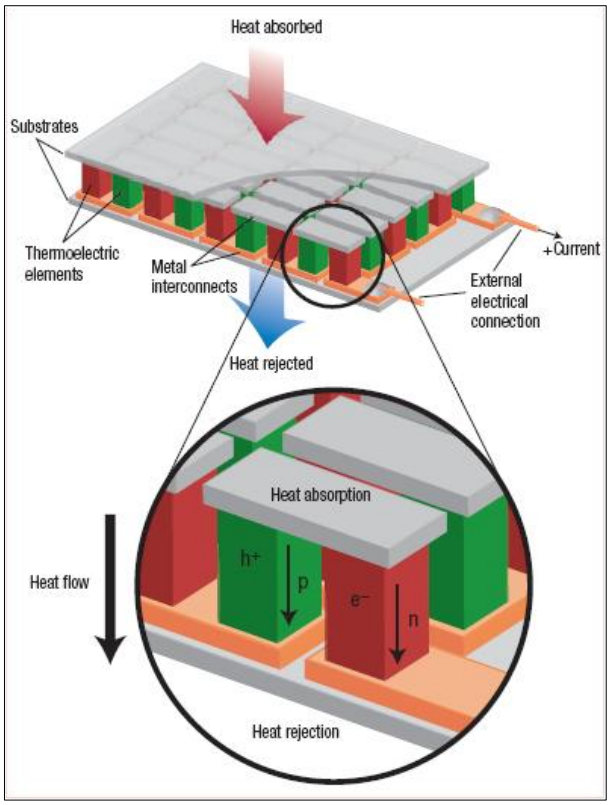

Figure 1.2[7]: Thermoelectric module

1.2 Applications and efficiency of thermoelectric materials

Thermoelectric machines work quietly over a wide range of temperature without any noise or environmental pollution, they require the least maintenance as they do not consist of any moving parts.[3, 11] These advantages make their application even more interesting. *Figure 1.3* shows some of the applications of the thermoelectric concept.

The Peltier effect has already been applied in thermoelectric coolers (TEC) like portable beverage and picnic coolers, and in wine storage cabinets.[8] Other applications include office water coolers, mini-refrigerators and in microelectronic systems, laser diodes, telecommunication and medical devices.[10, 12-14]

The Seebeck effect has been applied in thermoelectric power generators (TEG) in the communications industry, weather stations and as Radioisotope Thermoelectric Generators (RTG) to power navigational aids and space ships.[8] TEG are also used in remote areas of Northern Sweden to provide small amounts of electrical power.[3] However, Seebeck effect has not been applied in large scale despite their advantages due to the poor efficiency of the thermoelectric materials. The efficiency of heat pumps (for TEC in application of Peltier effect) or heat engines (TEG in application of Seebeck effect) is defined as the ratio of work output to work input.[11]

Thermoelectric CPU cooler

30 W Movable TEG which can be placed on top of a gas or wood stove

Thermoelectric cooler

Wine cooler and warmer

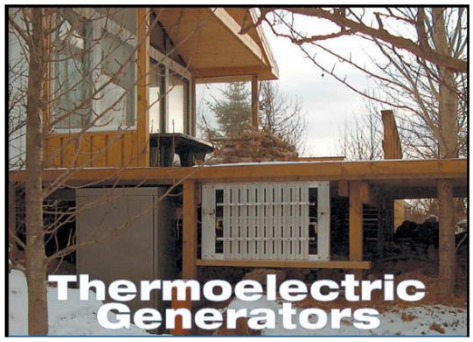

Thermoelectric generator for homes in Iceland

Figure 1.3[15-19]: TEC and TEG

In the Peltier effect, work is used to pump the heat from the cold to the hot reservoir; the efficiency, η, of the heat pump is represented by the coefficient of performance, COP.[11, 20] COP is the ratio of the heat pump to the work input, and at

Carnot efficiency, it is represented by ε_{max}.[11, 20] ε_{max} is given by the ratio of the temperature at the cold side to the temperature gradient.[11, 20] Therefore, the bigger the temperature gradient, the smaller is the efficiency as it would be easier to pump heat when the reservoirs are at equal temperatures.[11]

$$\varepsilon_{max} = \frac{T_C}{T_H - T_C} \tag{1.1}$$

On the other hand, in the Seebeck effect where work is extracted from the flow of heat from a hot to a cold reservoir, the Carnot efficiency, η_{max}, is the ratio of the work extracted to the heat leaving the hot reservoir. [3, 11] η_{max} is given by the ratio of the temperature gradient to the temperature at the hot side.[3, 11]

$$\eta_{max} = \frac{T_H - T_C}{T_H} \tag{1.2}$$

However, the thermoelectric efficiency is given by the product of the Carnot efficiency and the loss term.[11] The loss term is the degradation factor of the ideal thermodynamic efficiency and it depends on the dimensionless figure of merit, *ZT*. [8]

$$\text{Loss term for TEC} = \frac{\sqrt{1+ZT} - \frac{T_H}{T_C}}{\sqrt{1+ZT} + 1} \tag{1.3}$$

$$\text{Loss term for TEG} = \frac{\sqrt{1+ZT} - 1}{\sqrt{1+ZT} + \frac{T_C}{T_H}} \tag{1.4}$$

Hence, efficiency, η, of thermoelectric materials depends on *ZT* from the loss term and the temperature difference from the Carnot term. Unlike the case of TEC, for the same *ZT*, TEGs have greater efficiency for greater temperature difference. Moreover, the greater the *ZT* for the same temperature difference, the greater would be the efficiency, as shown in *Figure 1.4*. Up until now, available thermoelectric materials have an efficiency of about 5%.[3]

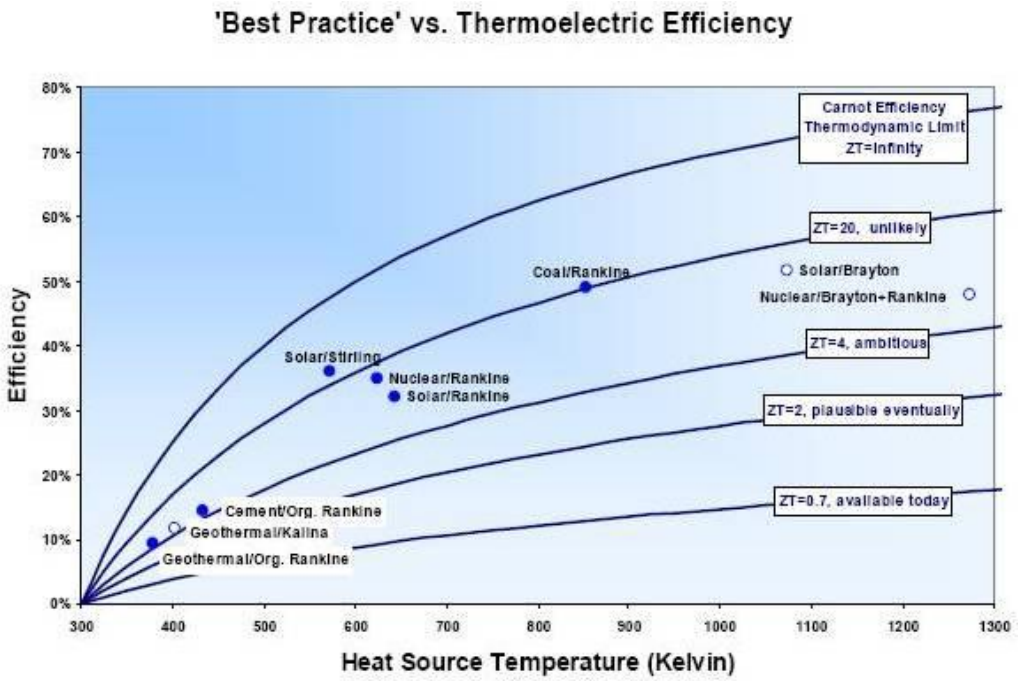

Figure 1.4[21, 22]: Efficiencies at different *ZT*

1.2.1 Criteria for efficient TE

As explained above, *ZT* plays a very important role in the efficiency of thermoelectric materials, therefore it is very important to understand the components of *ZT*. *ZT* of thermoelectric materials depends on the various parameters which are involved in the energy conversion: the Seebeck Coefficient (*S*), electrical conductivity (σ) and thermal conductivity (κ).

$$ZT = \frac{S^2\sigma}{\kappa}T \qquad (1.5)$$

A good thermoelectric material (*ZT* = 2 – 4), should have high *S*, about 200 μV/K - 250 μV/K, high σ greater than 1000/(Ωcm), and low κ (less than 1 W/(mK)).[23] These parameters and the conversion of heat energy to electrical energy are discussed below.

1.2.1.1 Seebeck coefficient

When a metal is heated at one end, the carriers of the materials (in the case of metal, the carriers are electrons) absorb the heat energy; this allows them to move faster from the hot end to the cold end. In so doing, heat is transferred from the hot end to the cold end and at the same time a potential difference is generated as negatively charged electrons are accumulated at the cold end resulting in a positively charged hot end (*Figure 1.5(a)*). The potential difference developed depends on the temperature difference between the two ends. The ratio of the potential difference to the temperature difference is called the Seebeck Coefficient value, *S*.

$$S = \frac{\Delta V}{\Delta T} \tag{1.6}$$

The Seebeck effect is the basic principle applied in thermocouples. *Figure 1.5(b)* shows how the potential difference (between metals A and B) generated by heating one of the two junctions joining the two dissimilar metals in a complete circuit can be measured. Since the potential difference developed is proportional to temperature difference, the temperature at the cold junction can be determined.

(a) (b)

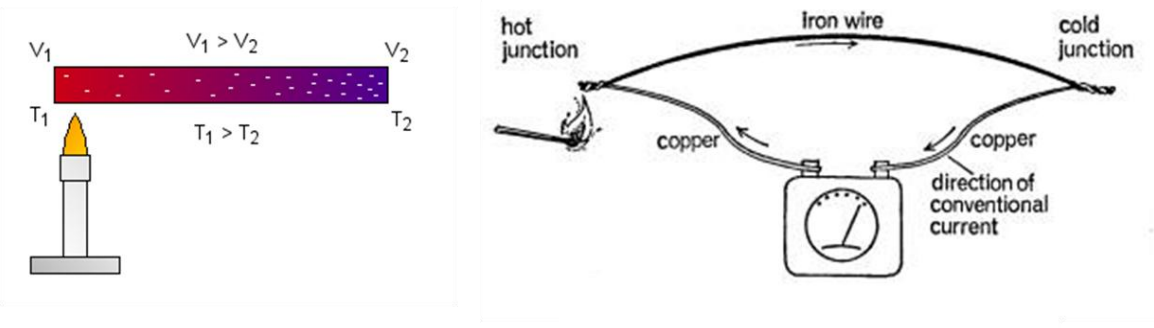

Figure 1.5[24, 25]: Schematic view of (a) generation of ΔV with ΔT (heat energy converted to electrical energy) (b) Measurement of ΔV

Since the transfer of heat is due to the movement of the carriers, the number of carriers (at the Fermi level) and how fast the carriers can move govern the diffusion of heat through the material. As a result, the carrier concentration and density-of-state

effective mass (as the mobility of a particle depends on its mass) are important parameters of *S* specially for highly doped materials (*Equation 1.7*).[7]

$$S = T\ \frac{8\pi^2\ k_B^2 m^*}{3eh^2}\ \left(\frac{\pi}{3n}\right)^{2/3} \qquad (1.7)$$

Where n = carrier concentration

m^* = density-of-state effective mass[7, 26]

K_B = Boltzmann constant

h = Planck's constant

Therefore, *S* has a linear *T* and $n^{-2/3}$ dependence, however, other than *T* and *n*, *S* also depends on m^*. Moreover, *S* also depends on the density-of-state (*DOS*) at the Fermi level as it is the carriers at the Fermi level that are involved in the whole process. The Mott Equation suggests that *S* is inversely proportional to the *DOS* at the Fermi level and directly proportional to the derivative of the *DOS* at the Fermi level.[27, 28]

$$S \propto -\ T\ \left\{\frac{1}{DOS(E)}\right\}\left\{\frac{\partial DOS(E)}{\partial E}\right\}|_{\mathrm{E = E_F}} \qquad (1.8)$$

DOS curves (plot of *E* vs. *number of states*) are derived from band structures (plot of *E* vs. *k*), the derivation of both plots is discussed in *Section 2.4*. For a large *S*, $DOS(E)|_{E=E_F}$ should be small, hence the band in the band structure should be flat as *DOS* $\propto \partial E/\partial k$ (for a flat band, $\partial E/\partial k$ is small). Furthermore, *S* also depends on the shape of the *DOS* at the Fermi level as suggested by the *Equation 1.8*; *S* is proportional to the slope.

1.2.1.2 Electrical conductivity

An electrical conductor offers a low resistance to the flow of an electrical current.[29] Hence, electrical conductivity, σ, is a measure of a material's ability to conduct an electric current.[29] σ of a material depends on its dimensions and resistance as per *Equation 1.9*.[29, 30]

$$\sigma = \frac{l}{R\,x\,A} \tag{1.9}$$

Where l = length of the material

R = resistance of the material

A = cross Section area of the material

Like the Seebeck effect, electrical conductivity too is due to movement of carriers, therefore, σ also depends on the carrier mobility, μ, and carrier concentration, n, as per Equation 1.10.[7]

$$\sigma = ne\mu \tag{1.10}$$

$$\mu = e\tau/m^* \tag{1.11}$$

Where τ = relaxation time and e = charge of the carriers

The relaxation time is the average time between two collisions of the carriers. It decreases with increasing temperature for any material due to increased scattering with phonons or impurities. In either case, the carrier mobility, μ, decreases with increasing T, this would result in decreasing σ with increasing T, like in the case of metals, unless the carrier concentration, n, increases as in the case of semiconductors.

Combining *Equations 1.10* and *1.11*, *Equation 1.12* is obtained according to which σ depends also on m^*.

$$\sigma = \frac{ne^2\tau}{m_*} \tag{1.12}$$

Since m^* is the density-of-state effective mass, just like S depends on the *DOS* at the Fermi level, so will σ as per the *Equation 1.13*.

$$\sigma \propto DOS(E)|_{\mathrm{E = E_F}} \tag{1.13}$$

For a material to have high σ, the *DOS* at the Fermi level should be high, implying that the derivative of the band $(\partial E/\partial k)$ in the band structure should be large,

hence, the band should be steep. This is completely opposite to the criteria for high *S*, this contradictory fact about *S* is discussed in *Section 1.2.1.1*.

1.2.1.3 Thermal conductivity

Thermal conductivity, κ, is a physical parameter that characterizes and quantifies the material's ability to conduct heat.[31] In solids, heat can be transferred by electrical carriers (electrons or holes), lattice waves (phonons), electromagnetic waves, spin waves or other excitations.[31] The heat conduction discussed in *Section 1.2.1.1* is mainly due to carriers and a small contribution from the lattice wave; this is the case for all pure metals. Thermal conductivity due to carriers is called electronic thermal conductivity (electronic kappa, κ_e) while the thermal conductivity due to lattice vibration is called the lattice thermal conductivity (kappa lattice, κ_l, or kappa phonon, κ_{ph}). The total thermal conductivity, κ, is the sum of the two contributions, this is the case for every other solid material.[31]

$$\kappa = \kappa_e + \kappa_l \tag{1.14}$$

Since one of the criteria for high *ZT* is low κ, it is important to understand the mechanism of the heat conduction via carriers and phonon. Both the κ_e and κ_l have temperature dependence, as whether it is the movement of carriers or lattice wave, both would be affected by increasing or decreasing temperature.

κ_e obviously depends on number of carriers, that is the carrier concentration, *n*, on which σ has a linear dependence. A constant *L* called the Lorenz number relates κ_e of pure metals to their σ by the Wiedemann-Franz Law (*Equation 1.15*).[30]

$$\kappa_e = L\sigma T \tag{1.15}$$

Therefore, κ_e, would behave as σ would with increasing or decreasing *n* and *T*. However, the Lorenz number, L[30, 31], which is often assumed to be the Sommerfeld value, 2.44×10^{-8} V^2K^{-2}, might differ from case to case. It has been observed that there are

factors like T and n which affect L, this might be an issue when calculating κ_l from κ. *Table 1.1* shows the values of L for some rare earth metals. In case of heavily doped semiconductors, L will be different from the Sommerfeld value due to resonance scattering of carriers.[32]

Table 1.1[31]: *L* of some rare earth metals

Metal	L (10^{-8} V^2/K^2)	T (K)
La	2.9	273
Pr	3.1	280
Nd	3.7	291
Sm	4.3	291
Tb	4.25	291

κ_l, which is due to the lattice wave, obviously depends on the speed of the sound wave (v), the mean free path (l_t) and the specific heat capacity (C_p).[31] Heat capacity is the amount of heat absorbed to increase the temperature of the material by 1 K.

$$\kappa_l = \frac{1}{3} c_v v l_t \tag{1.16}$$

Figure 1.6 shows a sketch of the temperature dependence of κ, C_v and l_t (T_D is the Debye temperature, it can be different for different solids), variation of v is negligible with T.[31] C_v is approximately constant at $T >> T_D$ and gradually decreases as T → 0 K, while l_t increases as T decreases until it approaches its limit somewhere $T > T_D$.[31] Therefore, $T > T_D$, $\kappa \propto T^{-1}$ for well-ordered solids unless the solid is porous or/and has defects where there will be deviation from the expected trend.[33-35]

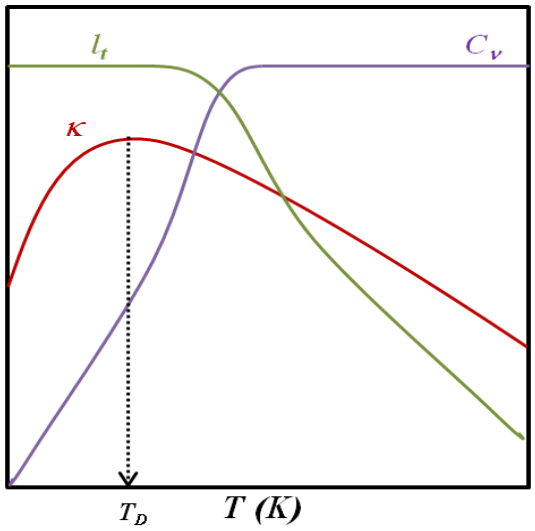

Figure 1.6: Temperature dependence of κ, l_t and C_v

Since for high ZT, κ must be small and σ must be high, the electronic contribution to the total thermal conductivity, κ_e, cannot be compromised as $\kappa_e \propto \sigma$ (lower κ_e would also mean lower σ). On the other hand, κ_l can be reduced; attempts are made to reduce κ_l to its minimum whereby all the phonons have l_t equal to interatomic spacing.[23] The most ideal thermoelectric material would be the 'Phonon Glass Electron Crystal', PGEC systems, whereby the material conducts electricity as a crystal and heat as a glass.[36] Such materials have high σ and low κ, the κ is reduced mainly through phonon scattering[23] like in the following cases:

- Systems with cage like structure whereby rattlers can be accommodated and act as scattering centers.[4]
- Ternary or quaternary compounds and solid solutions (random arrangement of different materials of the same structure in the system) can create phonon scattering as a result of mass fluctuation.[37]
- Materials with defects and impurities, which will again scatter phonons.[7]
- Nanostructured materials, which will have grain boundary scattering due to the presence of nanodomains.[38]
- Thin films or multilayer materials whereby the phonons will experience interface scattering.[39]

1.3 Potential TE materials

As discussed above, a good TE must have high *S* and σ but low κ, however, from *Sections 1.2.1.1* and *1.2.1.2*, this is quite contradictory. From *Equation 1.7*, $S \propto m^* n^{-2/3}$ and *Equation 1.12* suggests that $\sigma \propto n/m^*$, similarly, in *Equation 1.8*, $S \propto /DOS(\mathrm{E})|_{\mathrm{E}=\mathrm{E_F}}$ while $\sigma \propto DOS(E)|_{\mathrm{E}=\mathrm{E_F}}$ as per *Equation 1.13*, hence, if *S* has to be high, σ should be low and vice – versa. A compromise between these criteria is semiconductor as shown in *Figure 1.7*, the shaded area in the plot shows the range of carrier concentrations for heavily doped semiconductors which are the best candidate for thermoelectric applications.[7] Some examples are discussed below.

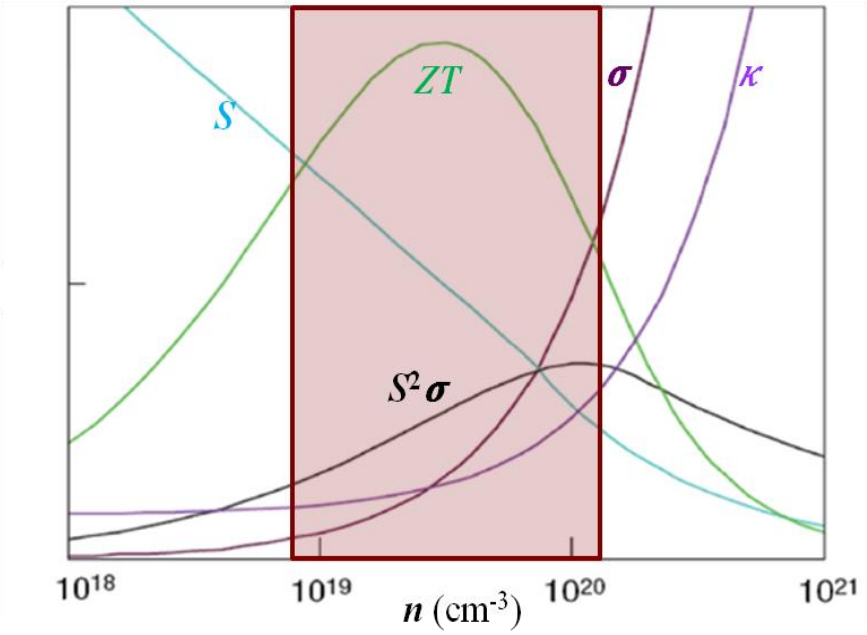

Figure 1.7[7]: General plot of *S*, σ, κ, $S^2\sigma$ (power factor) and *ZT* vs. *n*

1.3.1 Cage like semiconductors

Semiconductors having cage-like structures are skutterudites and clathrates, which can be considered as examples of Zintl materials. Zintl compounds have open complex structures and are semimetals or narrow gap semiconductors.[40]

Zintl phases consist of electropositive cations that donate their electrons to electronegative anions, the latter use the electrons to form bonds in order to satisfy valence.[41, 42] In these compounds, the atoms are arranged in a covalent network such that there are empty spaces which can be filled by guest atoms within the structure.[40] Phonon propagation through the lattice of partially filled systems will be interrupted due to the guest atoms in the cages acting as a scattering centre.[43] Therefore the covalent bonded regions provide 'electron crystal' properties as the carriers move easily in those regions.[41] The ionic regions provide 'phonon-glass properties' as the phonons get scattered.

1.3.1.1 Skutterudites

Binary skutterudites are cage like materials with general formula MX_3 where M is a metal atom and X is a pnictide.[44] Skutterudite type ($CoAs_3$-type) structure has a cubic unit cell that contains eight MX_6 octahedra linked through corners. The eight MX_6 octahedra sharing corners create a void in the centre of the $(TX_6)_8$ cluster, which sits at the (½, ½, ½) position of the cubic cell (*Figure 1.8*).[45]

Relatively large metal atoms can fill the void to give filled skutterudites, which are strong candidate for thermoelectric application due to their low κ. The low κ is a result of the strong phonon scattering by the 'guest' atoms as mentioned above. The smaller and heavier the 'guest' atoms, the larger will be the disorder and hence the greater will be the scattering of the acoustic phonons. Consequently, the reduction of the κ_l will be larger. Partially filled skutterudite, $Yb_{0.19}Co_4Sb_{12}$[43] exhibits a *ZT* value of approximately 1 at about 600 K and $Ba_{0.24}Co_4Sb_{12}$[46] demonstrated *ZT* greater than 1 above 800 K.

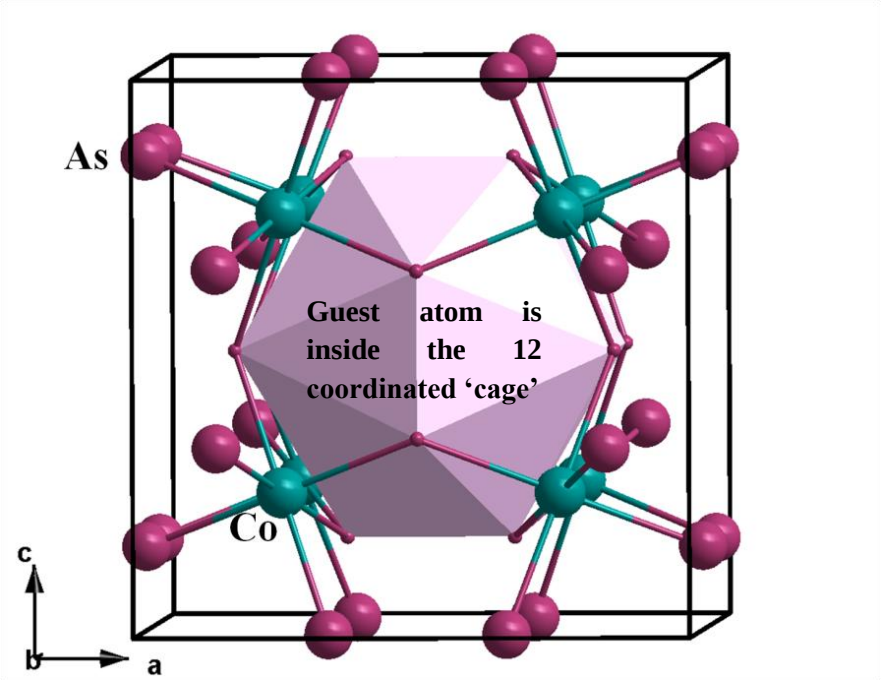

Figure 1.8[45]: Skutterudite crystal structure

1.3.1.2 Clathrates

Clathrates consist of frameworks forming cages whereby a guest atom can be enclosed.[45] They exhibit glass-like thermal conductivity due to the same mechanism as the skutterudites.[45] Clathrate compounds are formed in a variety of different structure types, type I is represented by general formula $X_2Y_6E_{46}$ or A_8E_{46} (where X and Y or A are alkali-metal, alkaline earth metal or rare earth metal and E is a Group 14 element, Si or Ge or Sn); type II is represented by $X_8Y_{16}E_{136}$ or $A_{24}E_{136}$.[31, 47] The difference between the two is that type I has 2 pentagonal dodecahedra (E_{20}) and 6 tetrakaidecahedra (E_{24}) per unit cell while type II has 16 dodecahedra (E_{20}) and 8 hexakaidecahedra (E_{28}).[31] Type III clathrate is a modified type I clathrates with 4 atoms removed from the E_{24} cages.[48] Other clathrates, which differ in their types and number of polyhedra per unit cell, exist.[49] *Figure 1.9* and *Figure 1.10* show type I and II clathrates respectively.

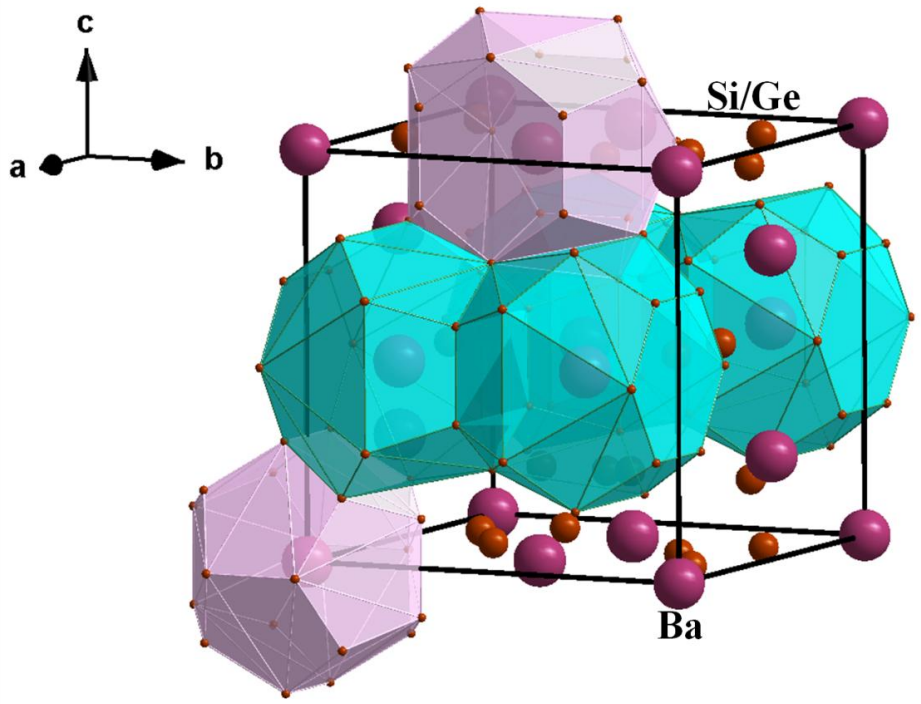

Figure 1.9[45]: Crystal structure of $Ba_8Ga_{16}Si_{30}$

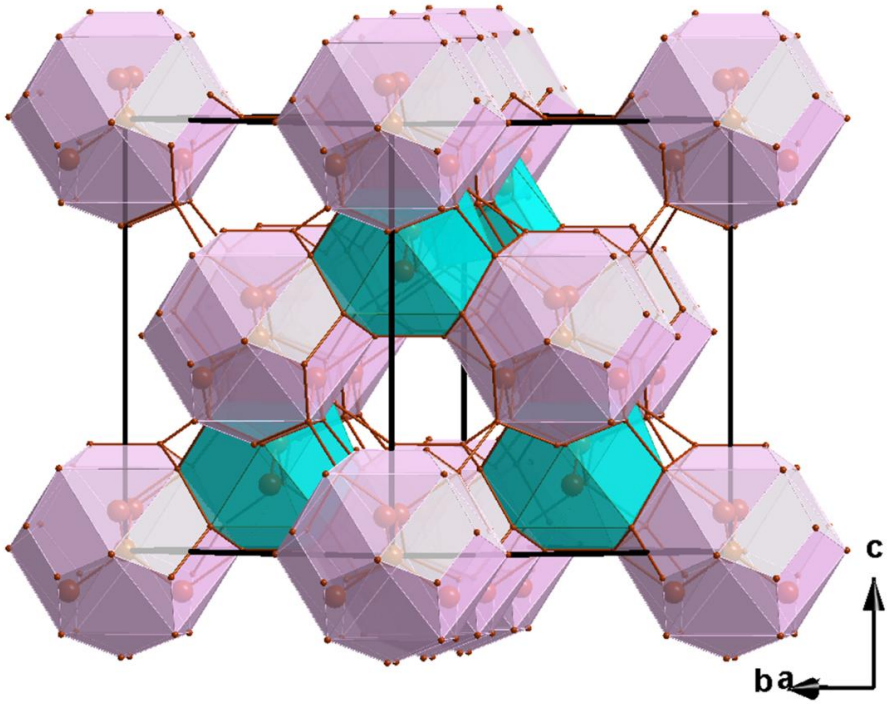

Figure 1.10[45]: Crystal structure of Si_{136} (type II clathrate without guest atoms)

The 'guest' atoms that are found inside the cages act as electrical dopants as they increase the electrical conductivity.[45] They also act as phonon-scattering centers as they lower the κ.[45] However, clathrate compounds without rattling guest atoms also have low thermal conductivity due to intrinsic vibrational properties of the framework and enlarged unit cell.[31] At room temperature Si_{136} (type II chlathrate) has κ close to amorphous silica while $Sr_8Ga_{16}Ge_{30}$ has κ very close to amorphous germanium. The lower κ in $Sr_8Ga_{16}Ge_{30}$ can be justified by the scattering of the low frequency heat carrying phonons by the rattling Sr atoms in the cages. On the other hand, in $Ba_8Ga_{16}Ge_{30}$, the guest atoms do not contribute in scattering the phonons but instead, they flatten the phonon band and avoid crossing of the acoustic phonon.[50] The flattening of the phonon bands decreases the velocities of the phonons.[47]

1.3.2 Layer structured semiconductors and solid solutions (defects)

The most popular thermoelectric material, which is considered as one of the state-of-the-art thermoelectric materials, is Bi_2Te_3.[7] It has a layered structure with a hexagonal unit cell as shown in *Figure 1.11*.

The layered structure consist of covalently bonded Bi and Te layers, adjacent Te layers are held by weak Van der Waals intermolecular forces of attractions, which can be broken easily along the *ab* plane.[23] As a result, Bi_2Te_3 has some anisotropic thermal properties. Along the *ab* plane, κ was found to be 1.5 W/(mK) while along the *c*-axis, the latter was found to be 0.7 W/(mK).[23] Both the *p*-type and *n*-type Bi_2Te_3 exhibit a κ of 1.9 W/(mK) at RT, giving a *ZT* of 0.6; doping the compound with Se and Sb resulted in $Bi_2Te_{2.7}Se_{0.3}$ and $Bi_{0.5}Sb_{1.5}Te_3$ respectively. Both of them had lower κ which improved the *ZT* value to approximately 1.[23] $Bi_{2-x}Sb_xTe_{3-y}Se_y$ solid solutions have been used for decades for room cooling applications due to their good *ZT* value of 0.95 at RT.[51] Such a good *ZT* value was obtained by optimising the composition.[52] The optimised composition was found to be $x = 0.5$, $y = 0.12$.[53]

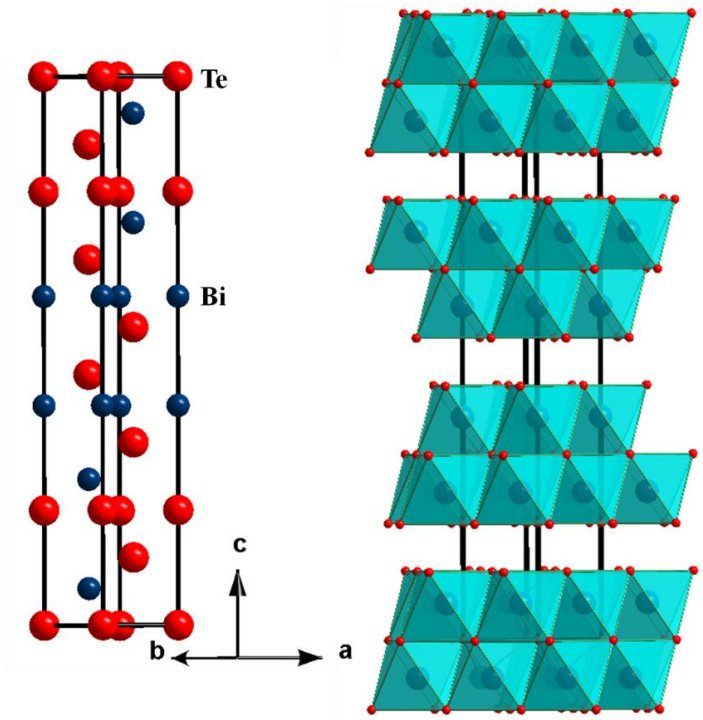

Figure 1.11[23]: Crystal structure of Bi_2Te_3

PbTe crystallizes in a cubic NaCl-type structure, *p*-type PbTe is obtained by doping the system with Na_2Te or K_2Te and *n*-type PbTe is obtained using donors PbI_2, $PbBr_2$ or Ge_2Te_3. The *ZT* value of PbTe solid solutions is about ~ 0.3 at 300 K due to its high κ_l of 2.3 W/(mK),[54] and ~ 0.7 at 700 K.[23]

Lots of solid solutions or thin films have been synthesized like this system, the most popular is $(AgSbTe_2)_{0.15}(GeTe)_{0.85}$ (TAGS).[7] TAGS exhibits κ_l as low as ~ 0.3 W/(mK) due to lattice strain in the structure and the presence of twin boundary defects, which further scatter phonons, the maximum *ZT* reached for the latter was ~1.2 at about 500 K.[7] Other solid solutions from the famous Bi_2Te_3 and PbTe systems are known some have better thermoelectric properties and are discussed in *Section 1.3.3*.

$CsBi_4Te_6$ is another thermoelectric with a layered structure and with good thermoelectric properties.[23, 51, 52] Doped $CsBi_4Te_6$ compounds have low κ values between 1.25 W/(mK) and 1.84 W/(mK) which are comparable to ~ 1.6 W/(mK), the κ values of $Bi_{2-x}Sb_xTe_{3-y}Se_y$.[52] The highest *ZT* value of $CsBi_4Te_6$ is 0.82 at 225 K, however, unlike $Bi_{2-x}Sb_xTe_{3-y}Se_y$, $CsBi_4Te_6$ exhibits a *ZT* value of only 0.65 at RT.[51]

1.3.3 Thin films, superlattices and nanostructured semiconductors

ZT of the above systems can be enhanced by the presence of nanostructures in thin films, which would improve *S* and decrease κ_l.[7] Such materials are promising thermoelectric materials as they exhibit high *ZT* (*ZT* > 1), the mechanism that is responsible for this differs from one case to another.[53]

$PbSe_{0.98}Te_{0.02}$/PbTe quantum-dot superlattices show a *ZT* of 0.9 at 330 K (κ_l as low as 0.34 W/(mK))[54] and 2 at 550 K due to the enhanced $DOS(E)|_{E=E_F}$ as a result of quantum-confinement effects.[53] In $Pb_{9.6}Sb_{0.2}Te_{10-x}$ (x = 0 – 10), other than atomic disorder between Te and Se atoms, there are nanocrystals of varying size and shapes embedded in the PbTe-rich matrix. Slight mismatch between regions with different composition (compositional fluctuation) results in crystal boundaries that will further scatter phonons. The max *ZT* for this series is 1.2 at 650 K for $x = 7$.[54]

n-Bi_2Te_3/$Bi_2Te_{2.83}Se_{0.17}$ and Bi_2Te_3/Sb_2Te_3 quantum dot superlattices were reported to exhibit a very high *ZT* of 1.4[53] and 2.4[53, 55] respectively at RT. The reason for such interesting *ZT* is their very low κ_l (~0.22 W/Km) which is a result of the phonon-blocking and electron-transmitting superlattices.[53] Another example of this scenario is 'Coessential'[38] nanocomposites of Bi_2Te_3, whereby Bi_2Te_3 nanotubes are added to Bi_2Te_3 based alloys. The latter shows a *ZT* of 1.25 (*Figure 1.12*) at about 420 K which is higher than that of the doped Bi_2Te_3 thanks to its low κ of ~0.8 W/(mK) due to the presence of the nanoscale phonon scattering centre.[38]

The most popular nanostructured system is $(AgSbTe_2)_x(PbTe)_{1-x}$ (LAST), which is the parent compound of many systems like LAST-*m*[23] and LASTT.[56] The low κ_l in those systems is attributed to the presence of Ag-Sb rich nanoparticles oriented randomly within the rock-salt crystal. This leads to different densities between different regions coexisting together in the system. As a result, phonon scattering occurs at the interfaces of those different regions.[7]

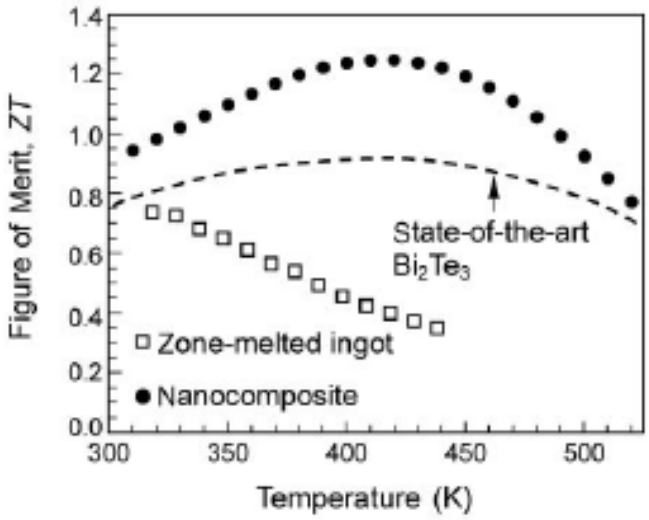

Figure 1.12[38]: *ZT* of Bi_2Te_3 nanocomposite and zone-melted sample

LASTT ($Ag(Pb_{1-y}Sn_y)_mSbTe_{2+m}$) have κ_l of ~ 0.70 W/(mK) at RT thanks to the nanodomains related to compositional fluctuations between Ag, Sb and Pb/Sn (*Figure 1.13(a)*). Just like $Pb_{9.6}Sb_{0.2}Te_{10-x}$, where the compositional fluctuation resulted in phonon scattering, $Ag_{0.5}Pb_6Sn_2Sb_{0.2}Te_{10}$ exhibited a high *ZT* of ~ 1.45 at 627 K for similar reason.

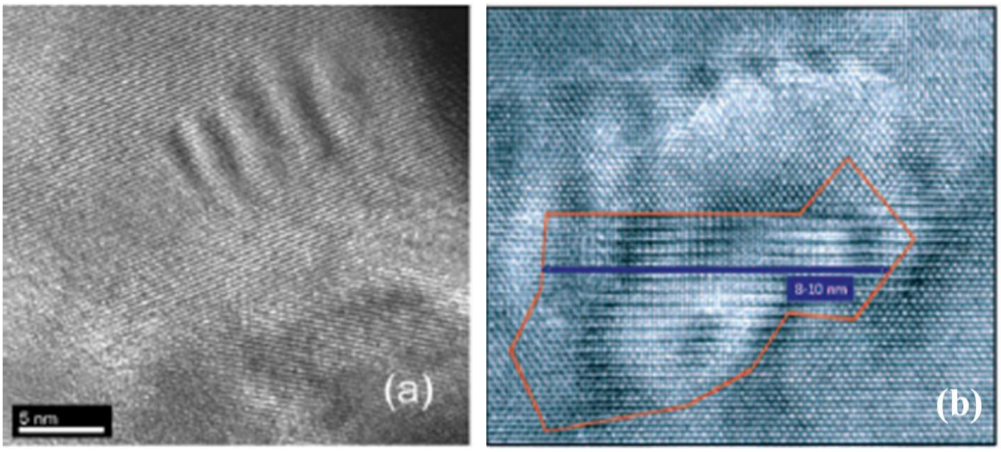

Figure 1.13[23, 56]: HRTEM image of (a) $Ag_{0.5}Pb_6Sn_2Sb_{0.2}Te_{10}$ showing a nanostructure (bright stripes) that is rich in Ag and Sb (b) a typical nanoscale inhomogeneity (indicated by the red outline) found in $Ag_{1-x}Pb_{18}SbTe_{20}$

LAST-*m* ($AgPb_mSbTe_{m+2}$) forms a big family of many compounds achieved by changing *m*. All of them showed good *ZT* (*ZT* > 1) for the same reason. At 700 K, LAST-10 and LAST-18 have *ZT* values of 1.2 and 1.7 respectively. Their low κ_l values (~ 0.45 W/(mK) at 700 K) are due to nanocrystals embedded in the matrix (*Figure 1.13(b)*).

1.3.4 State-of-art TE materials

Figure 1.14 shows the *ZT* vs. *T* plots of the above discussed state-of-the-art thermoelectric materials like Bi_2Te_3, PbTe, $CsBi_4Te_6$, LAST. In this Section, the state-of-the-art SiGe and $Yb_{14}MnSb_{11}$ are also discussed below.

The most widely used high-temperature thermoelectric material is SiGe, the *p*-type SiGe with *ZT* just above 0.5 at *T* > 900 K is used by NASA.[7, 57] SiGe alloys have a κ value of 10 W/(mK), about ~ 6 - 10 times lower than the values for the individual elements (Si and Ge). Such lower values with respect to the elemental values is due to scattering of the heat carrying phonons by grain boundaries.[31] They are used for high temperature energy conversions due to their stability at high temperature as a result of its 3-D macromolecular diamond like structure.

$Yb_{14}MnSb_{11}$[7, 57] is a Zintl compound that exhibits better thermoelectric properties than SiGe. It exhibit a maximum *ZT* of ~ 1.0 at 1223 K thanks to its glass like κ of ~ 0.7 - 0.9 W/(mK) between 300 – 1275 K (κ_l ~ 0.4 W/(mK) at ~300 K).[7] Such low κ is due to the complex structure and heavy atoms present in the system.[57] The complex structure with ionic bonds provides a less rigid structure and decreases the phonon mean free path. The heavy atoms in the structure do not help in transporting the phonon as they don't vibrate due to their heavy atomic masses. Together, these effects lead to low κ resulting in better *ZT* than SiGe.[57] Thanks to its excellent thermoelectric properties, NASA will be using it for the future development of TEG.[7]

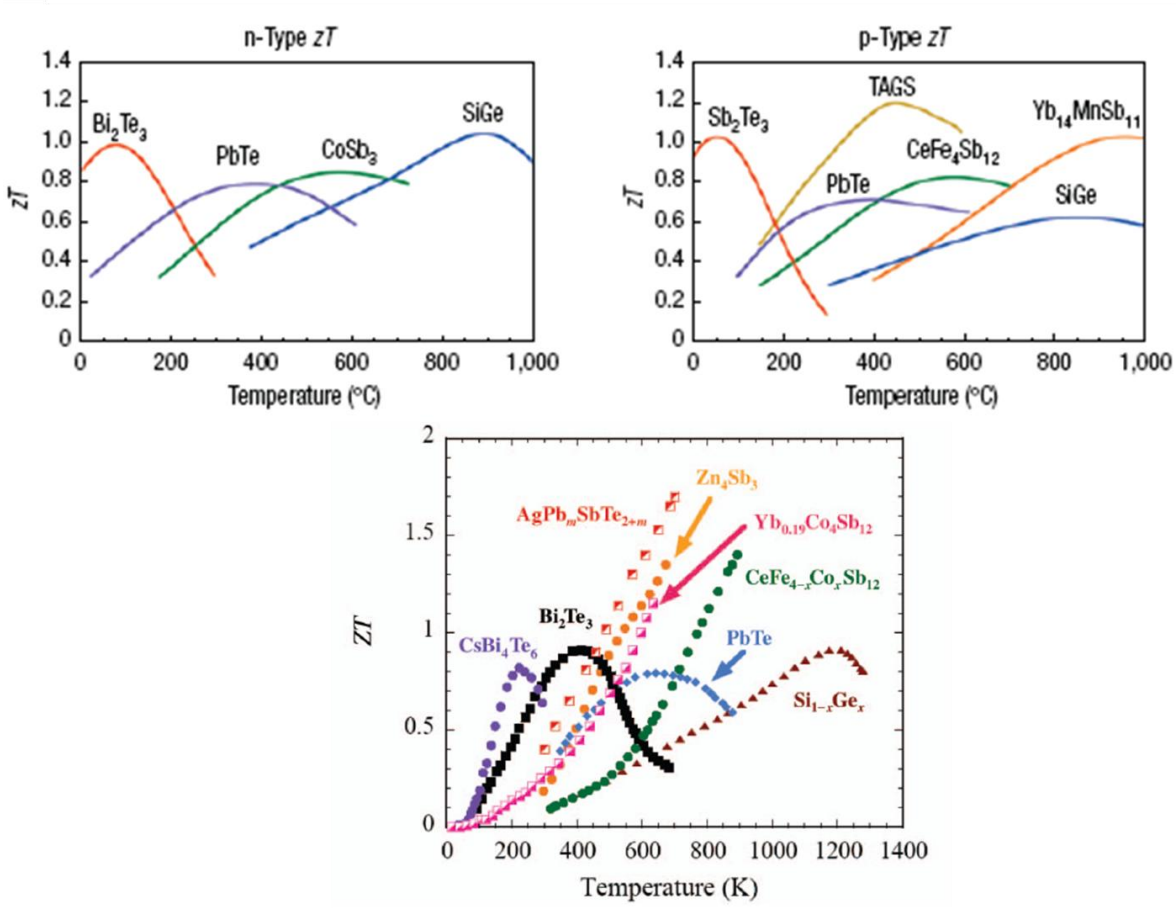

Figure 1.14[7, 23]: Plots of *ZT* vs. *T* for *n*- type (top left), *p*-type (top right) semiconductors and several bulk materials (centre)

1.3.5 Thallium compounds

From the above examples, it is obvious that a low κ is one of the critical and important parameter to have high *ZT* values. The compounds discussed above have some special features, like rattlers in cages, layered structures, atomic disorder, defects and nanodomains, which are responsible for low κ. However, most of the compounds with extremely low κ are thallium based compounds due to the soft nature of Tl–Tl bonds.[58] Some thallium based compounds with good thermoelectric properties are briefly discussed below.

1.3.5.1 Thallium-filled skutterudites

As discussed above in *Section 1.3.1.1*, skutterdudites have a cage like structure whereby the voids can be filled by 'guest' atoms which would rattle and hence scatter the heat carrying phonons. In thallium-filled skutterudites (Tl filling the voids in Co_4Sb_{12}), a similar hypothesis was reported.[59] As the amounts of Tl filling the voids in the skutterudite structure increases, the κ decreases for temperatures between 50 K and 300 K (*Figure 1.15*). The system gets exhausted for higher Tl containing compounds as the decrease in κ for the same temperature range 50 K – 300 K, plateaus. κ of the undoped skutterudite, Co_4Sb_{12} is maximum ~ 30 W/(mK) at 50 K and as low as 10 W/(mK) at RT while that of $Tl_{0.8}Co_4SnSb_{11}$ is maximum ~ 2.5 W/(mK) at 50 K and slightly above 2 W/(mK) at RT.[59]

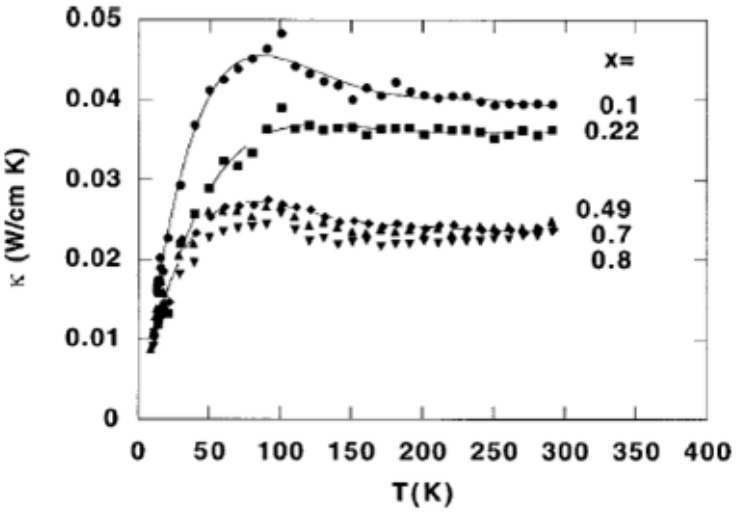

Figure 1.15[59]: Plot of κ vs. *T* for several Tl-doped skutterudites ($Tl_{0.1}Co_4Sb_{12}$, $Tl_{0.22}Co_4Sb_{12}$, $Tl_{0.49}Co_4Sn_{0.5}Sb_{11.5}$, $Tl_{0.7}Co_4Sn_{0.75}Sb_{11.25}$ and $Tl_{0.8}Co_4SnSb_{11}$)

The sudden and rapid decrease in κ is due to phonon scattering as a result of atoms rattling about their equilibrium position. Tl atoms rattle relatively more than the other atoms in the structure. Moreover, the more the Tl present in the skutterudite structure, the more significant the change in carrier concentration will be. This might

also be a reason for lower κ as other than increasing the κ_e, the increasing numbers of carriers will interact with the phonons and lead to electron-phonon scattering. Consequently, κ_l is further decreased. At RT, the best sample was $Tl_{0.1}Co_4Sb_{12}$ with a *ZT* value of 0.175; however, the best *ZT* value obtained in this family is 0.8 at 800 K for $Tl_{0.22}Co_4Te_{12}$. Both are *n*-type samples due to the electrons donated by the Tl atoms.

1.3.5.2.1 $TlMTe_2$, M = Sb and Bi (1-1-2 thallium based compounds) and silver thallium tellurides

The 112 compounds have a rhombohedral NaCl structure with space group *R*-3*m*. $TlSbTe_2$ and $TlBiTe_2$ differ in their thermoelectric properties significantly due to their different nature. $TlSbTe_2$ is a *p*-type semiconductor[60] while $TlBiTe_2$ is an *n*-type semiconductor.[61] The latter is also considered as a non-metallic superconductor.[60]

$TlSbTe_2$ has a *ZT* of 0.87 at 715 K as it has low κ (~ 1.4 W/(mK) at 300 K due to phonon scattering)[58] and high *S* (S_{max} = 224 μV/K at 666 K).[60, 62] On the other hand, $TlBiTe_2$ had a maximum *ZT* of only 0.15 at 760 K despite its low κ_{max} of ~ 2.1 W/(mK) at 490 K, this is due to its low *S* values (S_{max} ~ -75 μV/K at 760 K).[61, 62] Above 700 K, the *ZT* values of $TlBiTe_2$ increase rapidly due to a rapid increase in σ as a result of a phase transition.

Silver thallium tellurides are considered as a new class of advanced thermoelectric materials. Many compounds of this group of ternary combinations have very good *ZT* values thanks to their low κ. There are two main compounds in this group of ternaries, the Ag_9TlTe_6[63] and the AgTlTe[64].

Ag_9TlTe_6 exhibits a low κ of ~ 0.25 W/(mK) over a wide range of temperature above RT, the highest *ZT* of the latter is 1.23 at 700 K. In the attempt to further improve the thermoelectric properties of Ag_9TlTe_6, $Ag_{8.92}Tl_{0.94}Te_{5.15}$, $Ag_{9.04}Tl_{0.87}Te_{5.09}$ and $Ag_{8.94}Tl_{0.87}Te_{5.19}$ were prepared. The study of those compounds helped to understand how their thermoelectric properties changes with slight changes in stoichiometry. The low κ values of these compounds were maintained; the highest *ZT*

obtained at 645 K was ~ 1.03 for $Ag_{8.94}Tl_{0.87}Te_{5.19}$ and the highest *ZT* of 1.25 was exhibited by $Ag_{9.04}Tl_{0.87}Te_{5.09}$.

AgTlTe is a *p*-type semiconductor with very low $\kappa < 0.5$ W/(mK), however, it is not as good as Ag_9TlTe due to its low power factor ($S^2\sigma$) as a result of its low σ. The performance of AgTlTe was enhanced through doping with Cu at the Ag site ($Ag_{1-x}Cu_xTe$, x = 0, 0.02, 0.05, 0.1, 0.2, 0.3 and 0.4). The power factors ($S^2\sigma$) of the Cu doped AgTlTe materials were higher due to higher carrier concentration while still maintaining the κ low (< 0.5 W/(mK), *Figure 1.16(a)*). The maximum *ZT* was 0.61 at 580 K for x = 0.4, this is approximately two times the undoped compound as shown in *Figure 1.16(b)*.

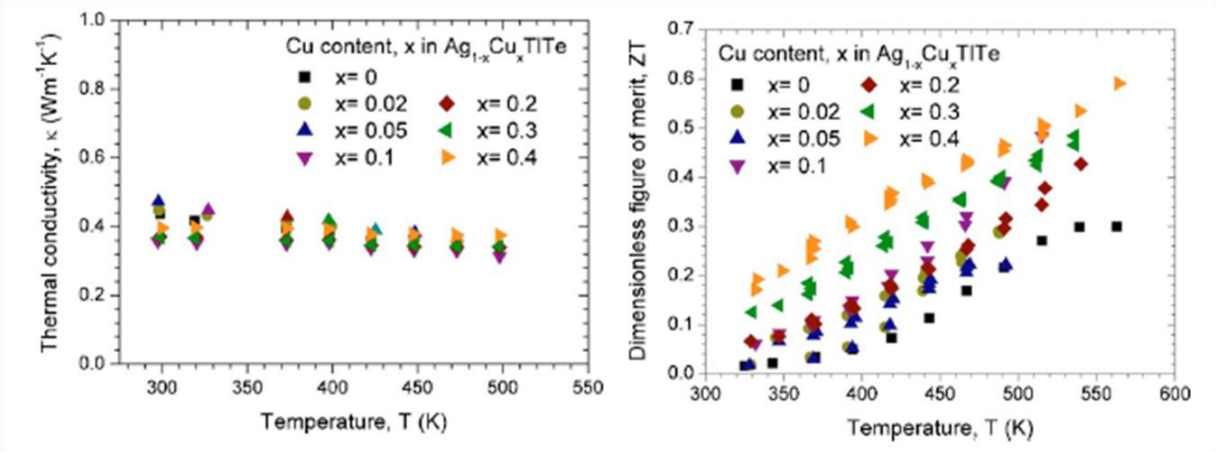

Figure 1.16[64]: Plots of (a) κ vs. *T* (b) *ZT* vs. *T* of $Ag_{1-x}Cu_xTlTe$

1.3.5.3 Tl_2MTe_5, M = Ge and Sn, 2-1-5 thallium based compounds

There are many ternary compounds from this family. In this section, Tl_2GeTe_5 and Tl_2SnTe_5, (TGT and TST respectively), will be discussed briefly. They both have a tetragonal unit cell with columns of Tl ions along the *c*-axis (*Figure 1.17*) and large interatomic distances for the eight fold coordinated Tl ions.[65] The large interatomic distances indicate that some of the thallium atoms are loosely bound in the structure and this justifies the large atomic displacement parameters. This is one of the reasons these

compounds were considered for thermoelectric properties as they are thereby expected to have low κ.[31, 65] κ_l of those systems were less than 5 W/(mK) which is less than one third of the value for pure Bi_2Te_3.[31, 65] *ZT* for TST was found to be ~ 0.6 at 300 K and is predicted to reach 0.85 at 400 K.[65] The structure of TST and TGT differ in the stacking of the (Ge/Sn)Te_4 tetrahedra and $TeTe_4$ square planar units linked into chains by edge sharing.[31, 65]

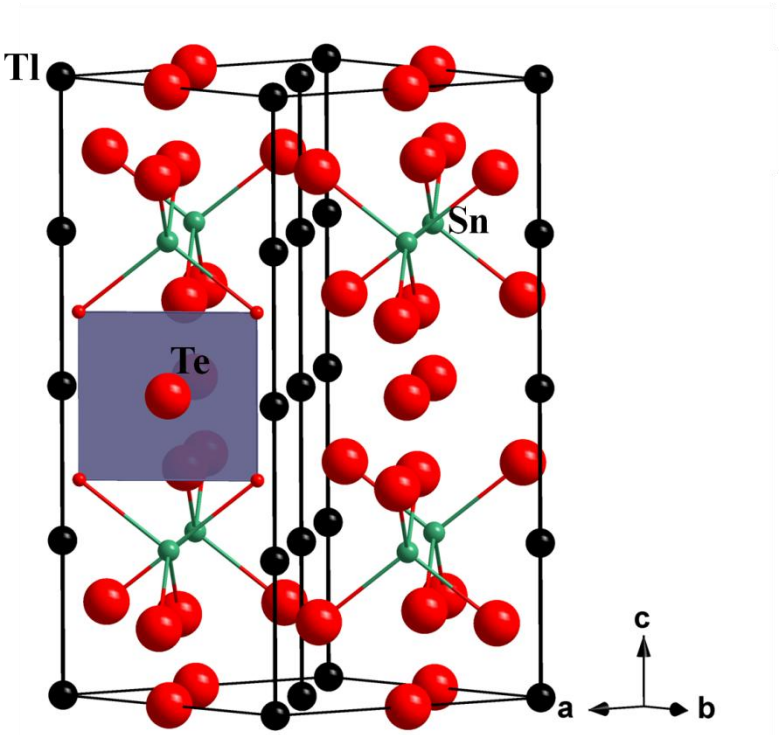

Figure 1.17: Crystal structure of TST

1.3.5.3.1 Tl_9MQ_6, M = Sb, Bi and Q = Se, Te (9-1-6 thallium based compounds) and $Tl_8M_2Q_6$, M = Sn, Pb and Q = Se, Te

The best thallium based thermoelectric material is Tl_9BiTe_6 with a *ZT* value of 1.2 at about 500 K on a zone refined sample, this is higher than ~ 0.8, the *ZT* of the optimized $Bi_{2-x}Sb_xTe_{3-y}Se_y$ and $(GeTe)_{85}(AgSbTe_2)_{15}$ (TAGS-85).[66] Tl_9BiTe_6 is one of the compounds from the large group of ternaries in this system (Tl_9MQ_6, M = Sb, Bi and Q = Se, Te and $Tl_8M_2Q_6$, M = Sn, Pb and Q = Se, Te).[67] Every compound from this system is derived from the isostructural Tl_5Te_3.

Tl_5Te_3 has a tetragonal, Cr_5B_3 structure type with space group *I*4/*mcm*.[68, 69] There are four different crystal sites; the *16l* site, which is 100 % occupied by Tl^{3+}, *4c* site occupied by Tl^{3+} and Tl^{+} in a 50:50 proportion, *4a* and *8h* sites occupied by Te^{2-} (Te1) and Te^{2-} (Te2) respectively.[66] *Figure 1.18* shows the structure of Tl_5Te_3 parallel to (011), the Te1 and Tl1 atoms form a straight chain along [001]. Tl1 forms a distorted octahedron with the surrounding four Te2 and two Te1 atoms {Tl1–Te1 = 3.15 Å (2×) and Tl1–Te2 = 3.36 Å (4×)}.

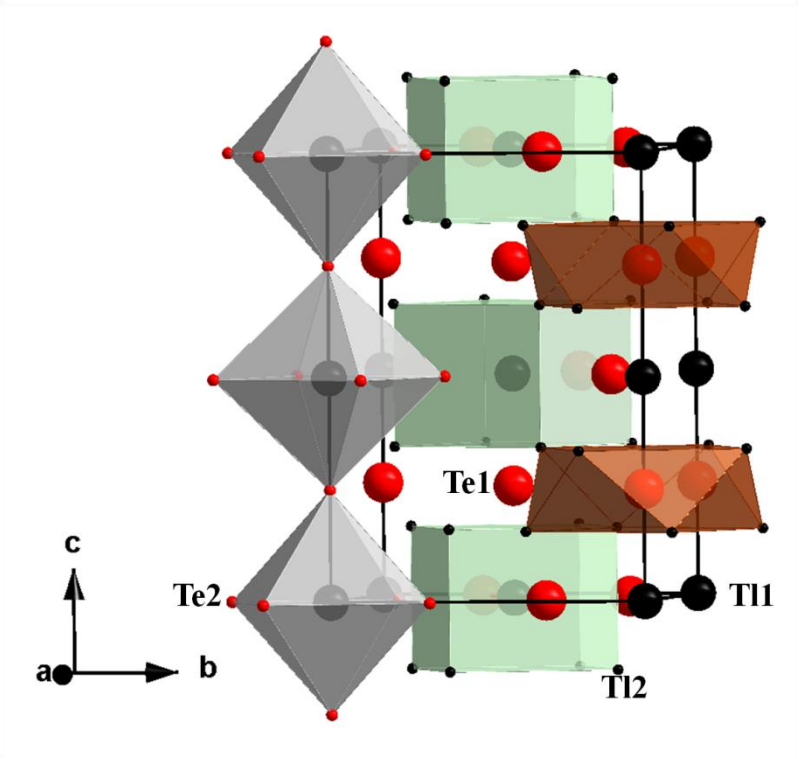

Figure 1.18: Tl_5Te_3 structure parallel to (011)

The Tl1 and Te1 atoms on the chain along [010] are surrounded by Tl2 atoms in a different environment, Tl1 is found at the centre of cubes formed by eight Tl2 while Te1 is surrounded by eight Tl2 in an archimedian antiprism.[68] *Figure 1.18* shows that Te1 is surrounded by eight Tl2 in an archimedian antiprism while *Figure 1.19* shows that the latter turns into an icosahedron with the two Tl1 on its opposite sides along the *c*-axis. Therefore, Te1 forms an icosahedron with eight Tl2 and two Tl1. On the other hand, Te2

forms a dodecahedron with six Tl2 and two Tl1. The coordination sphere of the atoms sitting at the *4c* and *16l* sites are discussed in *Section 3.1.2.2* and shown in *Figure 3.4*.

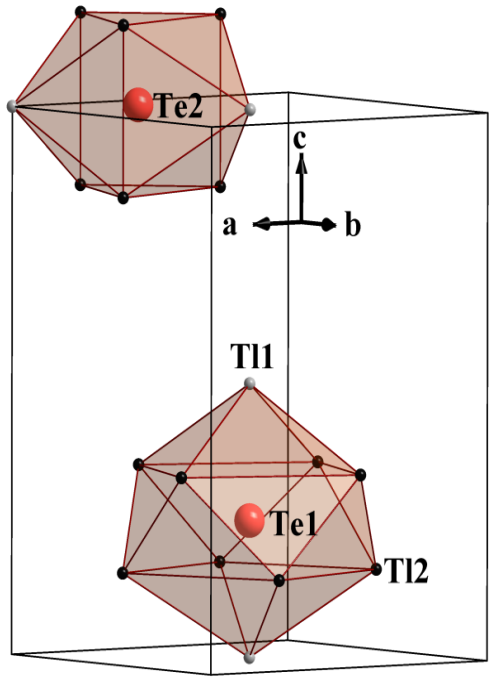

Figure 1.19: $(Te1)(Tl1)_2(Tl2)_8$ and $(Te1)(Tl1)_2(Tl2)_6$ polyhedra

The icosahedra share corners with each other just like the dodecahedra are connected to each other. Just like the two Te sites have different coordination spheres, the two Tl sites too have two different coordination spheres as discussed in *Section 3.2.2*.

Despite its low resistivity ($\sigma >> 1 \times 10^5/(\Omega m)$, Tl_5Te_3 is not a good thermoelectric material due to its low $S << 50$ μV/K and high $\kappa \sim 4$ W/(mK) (65% contribution form κ_e).[58] Such properties are attributed to metallic materials. Unlike the latter, Tl_9BiTe_6 of the same structure type has κ as low as 0.39 W/(mK) at 300 K. The low κ is attributed mainly to the disorder and mixed valence (50% of Bi^{3+} and 50% of Tl^+) on the *4c* site. Mass fluctuation does not have a contribution in scattering the phonon since the mass difference between Tl and Bi is very small (~ 2 %),[66] similar properties were observed for Tl_9GeTe_6.[8] The strong scattering of phonons due to random arrangement of mixed valence ions, Tl^+ and Bi^{3+}, at the *4c* site is supported by the fact that the κ of the Tl_8PbTe_6

(Tl_8PbTe_6 does not have disordered arrangement but two Pb at the *4c* site) is 0.72 W/(mK). [66] The second best thermoelectric material in this group of ternary compounds is Tl_9SbTe_6 with $ZT \sim 0.42$ at 591 K.[70]

It is believed that the κ can be further reduced if other than disorder and mixed valence, mass fluctuation could contribute in the scattering of the phonons. This is the basis of the motivation for the study of thallium lanthanoid tellurides, the present work.

1.4 Conclusion and project motivation

The aim of most thermoelectric research is to come up with a suitable cost effective thermoelectric material with a high *ZT* value to be able to contribute in managing the global energy demand. Lots of research has already been done on different materials to understand the challenges in the field. The main objective of many research groups is to develop new materials and optimise the properties of already existing materials, the most popular route to that is nanostructuring of the existing materials. Scientists are trying to introduce nanodomains in many of the already known materials like SiGe, PbTe and $BiTe_3$. Recently, nanostructures of skutterudites, $CoSb_3$, have been successfully obtained and the thermoelectric properties of the nanostructured $CoSb_3$ skutterudites were enhanced. Another prospective method to decrease the thermal conductivity while increasing the electron density-of-state at the Fermi level is hybrid or composite bulk materials like the composites Bi_2Te_3. In this technique, the nanostructure is incorporated into the bulk structures as additive and the thermal conductivity is expected to decrease via nanoscale phonon scattering centres.

There are few compounds which surpassed the thermoelectric properties of the state-of-the thermoelectric materials like $Yb_{14}MnSb_{11}$, a Zintl compound which will be used in thermoelectric generators in NASA projects instead of the well known SiGe thermoelectric in the future. Another compound is Zn_4Sb_3, which has the 'phonon-glass behaviour' accounting for its low thermal conductivity, and hence high *ZT* of 1.4 at about 400^{o}C.

Many efforts are put to lower the thermal conductivity of thermoelectric materials without decreasing the electrical properties. Materials already exhibiting very low thermal conductivity are thallium based compounds which are also explored extensively already. The best thallium based compounds known to date are Tl_9BiTe_6 and $Ag_{9.04}Tl_{0.87}Te_{5.09}$ with a $ZT \sim 1.2$ at about 580 K and 700 K respectively. However, thermoelectric properties of the 9-1-6 family of this series with lanthanoids are not yet known. Atomic masses of lanthanoids and thallium differ much more than thallium and bismuth, therefore, mass fluctuation is expected to contribute in further lowering the thermal conductivity in addition to the phonon scattering phenomenon present already due to random arrangement of Ln/Tl at the *4c* site. Moreover, f-block elements possibly have heavy f-electrons at the Fermi level, which would be an advantage for the Seebeck coefficient values as the Seebeck coefficient is directly proportional to the effective mass. Therefore with lower thermal conductivity and better Seebeck coefficient values, 9-1-6 thallium lanthanoid tellurides might exhibit better *ZT* values than Tl_9BiTe_6; hence, the thermoelectric properties of thallium lanthanoid tellurides and how doping the latter changes the thermoelectric properties is worth an investigation. With the collaboration of the General Motors of Canada, the structure and thermoelectric properties of thallium lanthanoid telluride was explored during this research work.

In this work, thallium lanthanoid tellurides, $Tl_{10-x}Ln_xTe_6$, $0.25 \leq x \leq 1.32$, Ln = La, Ce, Pr, Nd, Sm, Gd, Tb, Dy, Ho and Er will be synthesized and characterized. The physical properties of all these compounds will be measured to determine their *ZT* values, from which they could be classified as good or better thermoelectric materials, with respect to the already known 9-1-6 thallium compounds. The aim of this study is purely for scientific purpose as thallium based thermoelectric are least likely to be commercialised due to the toxicity of thallium. Therefore, this study will add up to the scientific data available about the thermoelectric properties of 916-thallium based tellurides. Moreover, this study will help to understand the behaviour of 916-thallium based tellurides with lantahnoids and determine whether or not they are suitable thermoelectric materials.

2 METHODOLOGY

In this chapter, the background and experimental procedures of the different techniques used in this thesis will be discussed. The first part of the project was to synthesize and characterize the thermoelectric materials followed by the second part which involved measurement of the thermoelectric properties of the pure compounds.

2.1 Synthesis of thallium lanthanoid tellurides

In solid state chemistry, there are many methods good for laboratory or/and industrial purpose to prepare inorganic solids, some common methods are briefly covered below. The choice of the technique depends on the starting materials/product involved and on the form of the product required (single crystals or polycrystalline powder or amorphous phase).[71, 72]

- **Ceramic method**

This method consists of heating together two solids which react to form the required product. The challenge in this technique is the homogeneity of the product as solid state reaction occurs at the interface of the two solids. Once the surface layer has reacted, the reaction continues as the reactants diffuse from the bulk to the interface (*Scheme 2.1*). The interaction between the two starting materials becomes harder as the amount of the solid product between the interfaces of the two starting materials increases, hence, the reaction gets slower. The solution to this issue is grinding finely the starting materials together and even before the completion of reaction, the mixture can be removed, ground and put back in the furnace.[71, 72]

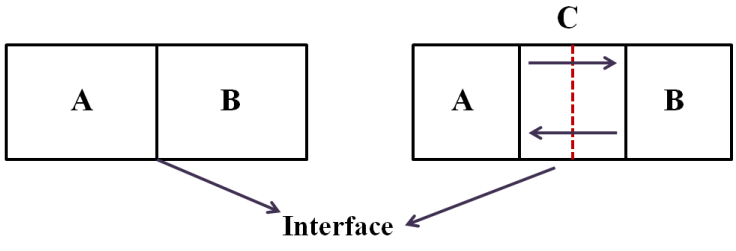

Scheme 2.1: Reaction between A and B to give C at the interface

- **The SOL-GEL method**

As the name suggests, a sol (colloidal suspension of particles in a liquid) of the reactants in a suitable liquid is prepared, the sol is either treated or left to stand to form a gel.[72] A gel is a semi-rigid solid in which the solvent is contained in a framework of a material which is either colloidal or polymeric. The gel is then heated to get the final product (*Scheme 2.2*).

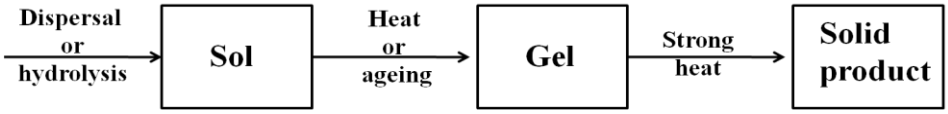

Scheme 2.2[72]: Steps in the sol-get synthesis route

- **Precursor method**

In this method, a solid precursor is first prepared in which the required elements are present in the right mole ratio. The precursor is then decomposed to the required product by heating.[72]

- **Chemical vapour transport**

Chemical vapour transport is used both for sample preparation and crystal growth. A solid or solids interact with a volatile compound and a solid product is deposited in a different part of the apparatus at a different temperature (*Scheme 2.3*).[71, 72]

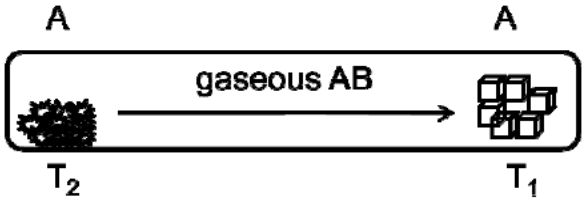

Scheme 2.3: Chemical vapour transport for crystal growth

2.1.1 Experimental

All the compounds were synthesized by the same method in this thesis, the stoichiometric amount of respective elements, were measured and put in a silica tube in an argon filled glove box. The tubes containing the elements were taken out of the glove box and evacuated on a vacuum line. The silica tubes, under a pressure of approximately 10^{-3} mbar, were then sealed with a hydrogen torch and put in a furnace set at the appropriate temperature profile (RT to 623 K in 5 h, held at 623 K for 24 h, heat up to 873 in 24 h, held at 873 K for 48 h and cooled down to 723 K in 100 h).

For all the compounds with $x > 1$, after the furnace was off, the reaction mixture was pressed into pellets and put in a silica tubes in the argon filled box. The tubes were evacuated, sealed and put in the furnace to anneal the pellets at 728 K for 1 week. This process was repeated until phase pure compound was obtained.

In the attempt to grow single crystal, a Bridgman experiment was attempted to synthesize Tl_9LaTe_6. In the Bridgman experiment, the reaction mixture (mixture of right stoichiometric amount of the respective elements) in an evacuated and sealed silica tube was put in a temperature gradient furnace. The furnace at the hot side was set at heating profile mentioned above; the maximum and final temperature at the hot side was 873 K. The cooling profile was done differently in this experiment. The cold end of the temperature gradient furnace was set at 723 K. The cold end and the hot end were approximately 30 cm apart. The silica tube was moved down the temperature gradient furnace from the hot side (873 K) to the cold end (723K), in one month.

The technique is close to the ceramic technique, the only difference is that in the first part, Tl (melting point of ~ 575 K) melts and the reaction is then between a molten state thallium and solid state materials. *Scheme 2.4* shows the steps involved in the synthesis of the thallium lanthanoid tellurides.

All the elements were bought from Alfa Aesar and most of them were used without any further treatment. The elements used are Tl, granules, 99.9999% (cleaned and dried on the vacuum line as the Tl bought was stored under water); Te, broken ingots, 99.99% (sublimed to get higher purity tellurium ingots); La, powder, -40 mesh,

99.9%; Ce powder, -325 mesh, 99.9%; Pr powder, -40 mesh, 99.9%; Nd, powder, -40 mesh, 99.9%; Sm powder, -40 mesh, 99.9%; Gd, powder, -40 mesh, 99.9%; Tb, powder, -40 mesh, 99.9%; Dy, powder, -325 mesh, 99.9%; Ho, powder, -325 mesh, 99.9%; Er, powder, -40 mesh, 99.9% .

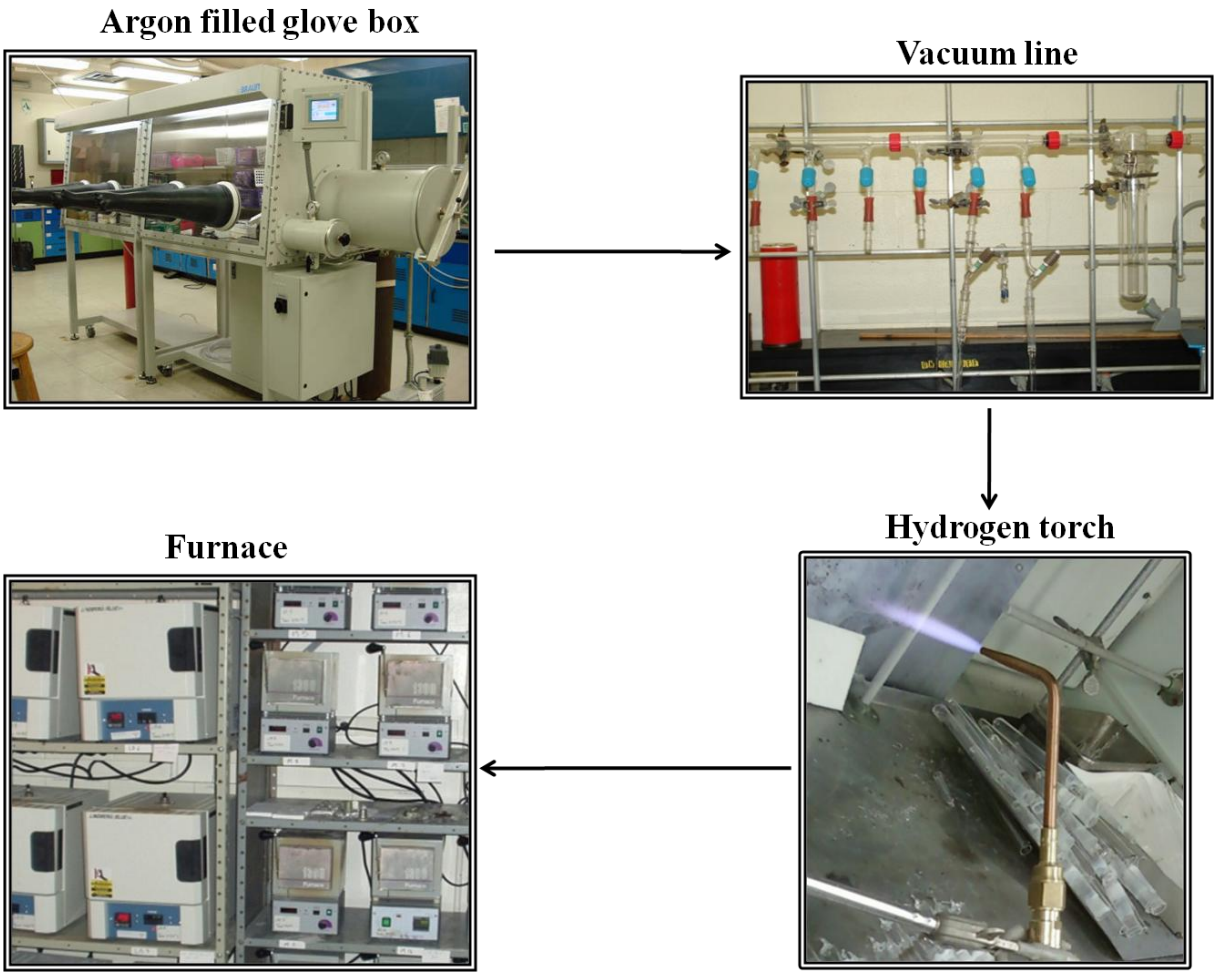

Scheme 2.4: Steps involved in the synthesis of thallium lanthanoid tellurides

2.2 Analysis of thallium lanthanoid tellurides

A combination of various analytic methods (PXRD, single crystal X-ray diffraction, EDX, DSC analyses) was used to analyze the samples as one would not be able to conclude the phase purity, homogeneity and the stoichiometry of the compounds

by only one technique. All the various techniques support each other and together they help to conclude how successful the syntheses were.

For example, powder X-ray diffraction is used to determine the phases in the product. Single crystal X-ray diffraction will support the XRD data by giving the crystal structure and formula of the compound, hence confirming the phase. The stoichiometry of the compound together with the homogeneity of the compound are obtained from EDX, if the compound was homogeneous, the stoichiometry obtained from EDX should be close to that obtained from the single crystal X-ray diffraction. The combination of the techniques used to characterize the samples is discussed in more detail in *Chapters 3*.

2.2.1 Powder X-ray Diffraction

X-rays were discovered by a German Physicist, Röntgen, in 1895 and it is only in 1912 that their wave nature was reported by Von Laue.[72] He used a crystal of copper sulphate as the diffraction grating to diffract the X-rays because crystalline solids consist of an ordered arrangement of particles with interatomic spacing of the order of ~ 100 pm. An incident light with wavelength of the same order as the magnitude as the spacings of the grating will get diffracted when passed through the crystal.

In 1913, W. H. and W. L Bragg determined the structure of NaCl using the X-ray diffraction, they noted that X-ray diffraction behaves like 'reflection' from the planes of atoms within the crystal and that they are 'reflected' from the planes only at specific orientations of the crystal with respect to the source and detector.[71, 72] The condition for the reflection of X-rays by a crystal is illustrated in *Figure 2.1*. Incident X-rays **A** and **A'** of wavelength, λ, are scattered by atoms **B** and **B'** at angle, θ, to give the reflected rays **C** and **C'** respectively; the reflected rays are in phase with one another, this condition is called the constructive interference. Constructive interference occurs when the path lengths of the interfering beams differ by an integral number of wavelengths.[71-73]

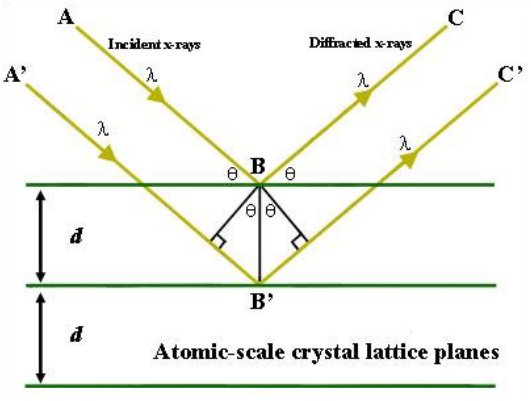

Figure 2.1[74]: Bragg's Law of reflection

From *Figure 2.1*,

$$\text{Difference in path length} = 2d_{(hkl)}Sin\theta_{(hkl)} \quad (2.1)$$

For constructive interference, difference in path length should be an integral number, *n*, of wavelengths (λ). Hence, *Equation 2.2* is derived.

$$n\lambda = 2d_{(hkl)}Sin\theta_{(hkl)} \quad (2.2)$$

Equation 2.2 is known as the Bragg Law whereby $\theta_{(hkl)}$ is the Bragg angle, the angle at which the incident X-ray interacts with the atoms on the (hkl) planes, the Miller indices and d_{hkl} is the interatomic spacing, the distance between a set of (*hkl)* planes.

When a crystal is subjected to X-rays, each atom of the crystals scatters the X-rays. The detector in a diffractometer detects the angle at which the X-rays are scattered along 2θ and the intensities of the scattered X-rays to give diffraction pattern which is a plot of *intensity (counts)* vs. 2θ.

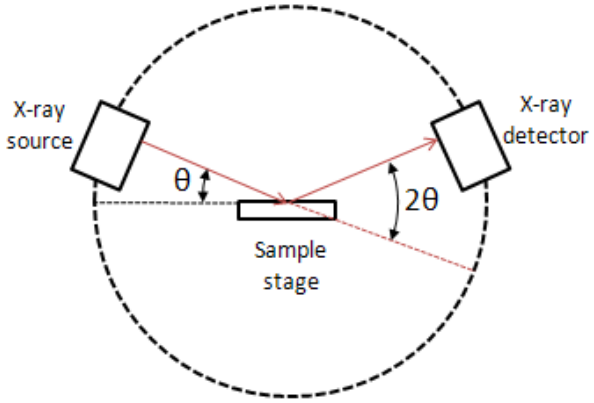

Figure 2.2[75]: Schematic representation of the principle of a powder X-ray diffractometer

Each peak corresponds to a resultant wave scattered by the atoms sitting on a particular (*hkl*) plane. Each atom scatters the X-ray differently depending on its atomic mass and position; the extent to which each atom (*j*) in the structure scatters the X-ray independently is called the scattering factor, f_j, of that particular atom (*j*). f_j depends on the number of electrons of the atoms, the Bragg angle and the wavelength.[73]

$$f_j = f_0 e^{-\frac{B\sin^2\theta}{\lambda^2}} \quad (2.3)$$

Where f_0 = observed scattering factor

$B = 8\pi^2 U$ (U is the temperature factor, the average vibration amplitude)

The scattering factor of all the atoms sitting on the (*hkl*) plane gives the scattering factor of the structure from that (*hkl*) plane called the structure factor, $F_{(hkl)}$. $F_{(hkl)}$, which is the extent to which all the atoms on that (*hkl*) plane in the unit cell will scatter the X-rays.[73]

$$F_{(hkl)} = \sum f_j e^{2\pi i(hx_j+ky_j+lz_j)} \quad (2.4)$$

Where (x_j,y_j,z_j) is the fractional coordinates of atom *j* in the unit cell.

The intensity, *I*, of the resultant wave from a particular (*hkl*) plane depends on the atomic masses and the atomic positions of all the atoms sitting on that (*hkl*) planes in the crystal structure. *I* is proportional to the square of the structure factor, $F_{(hkl)}$.[73]

$$I_{(hkl)} \propto |F_{(hkl)}|^2 \tag{2.5}$$

Powder X-ray diffraction is the first analysis one would do. From the diffraction pattern, the following information can be obtained:[73]

- lattice parameters (*a*, *b*, *c*, α, β, γ) of the unit cell as they depend on $d_{(hkl)}$ which depends on position of the peak, 2θ according to Bragg's Law.
- scattering factor and atomic positions of the atoms as they affect the intensities of the peaks.
- defects in the structure as they affects the peak shape.

2.2.1.1 Experimental

The sample was finely crushed until a homogenous fine powder was obtained; the sample was then put on an aluminum sample holder which was then loaded on a rotating platform in the Power XRD instrument (*Figure 2.3, left*). The instrument used for all the analysis is the INEL diffractometer (*Figure 2.3, right*) utilizing Cu-$K\alpha_1$ and a position sensitive-detector. As the X-rays bombarded the sample, they were diffracted as mentioned in S*ection 2.2.1*; the sample was kept rotating to allow as many planes as possible to satisfy the diffraction condition. All the samples were scanned for 15 - 30 minutes unless more accurate measurements were needed for refinements, in which case the experiments were ran overnight. The diffracted rays are detected by the detector with a detection range of $0^o - 120^o$ along 2θ as illustrated in *Figure 2.3*.

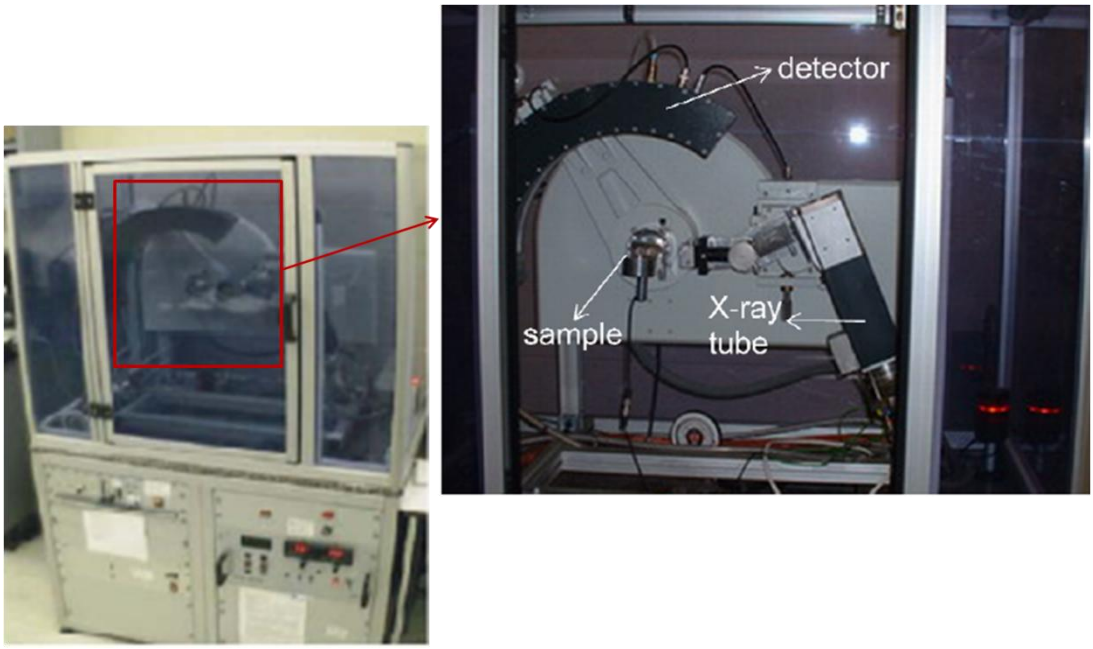

Figure 2.3: Powder X-ray diffractometer and INEL detector

The diffraction patterns obtained were compared against a database such as the Inorganic Crystal Structure Database (ICSD) to know the structure type of the compound present in the sample, however, phases present in less than 5 % are not detected by this technique.[72, 73]

2.2.2 Single crystal structure determination

Single crystal X-ray diffraction is the most convenient and accurate method to determine the crystal structure of a compound; however, the challenge for this technique is to get a good quality crystal. The basic principle of this technique is same as in powder X-ray diffraction. One of the differences is that the sample is mounted onto either a 3-circle or a 4-circle goniometer, these circles refer to the four angles (2θ, χ, φ, and Ω) that define the relationship between the crystal lattice, the incident ray and detector (*Figure 2.4*).[72] The crystal can move on the χ, φ, and Ω circles and the detector on the 2θ circle. The second difference is that the data is collected as reflections in a set of frames.[72]

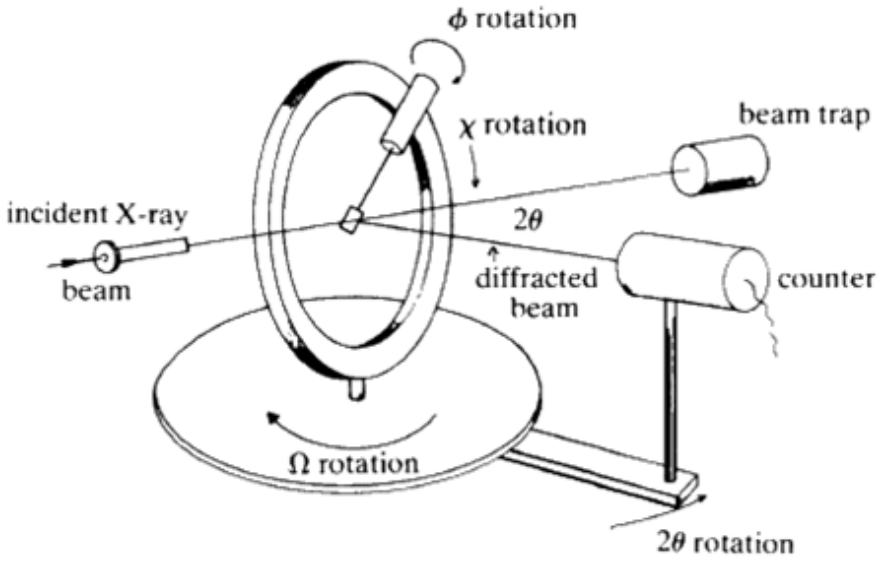

Figure 2.4[72]: Schematic diagram of a four-circle diffractometer

2.2.2.1 Experimental

A single crystal is mounted on a thin glass fiber which is attached to a brass pin and mounted onto a goniometer head in the single crystal X-ray diffractometer, a Bruker Smart Apex CCD diffractometer with graphite-monochromatized Mo-Kα_1 radiation (*Figure 2.5*). The crystal is then centered within the X-ray beam by adjusting the X, Y and Z direction followed by data collection in a set of frames by SMART software which is integrated in the APEX2 package.[76] ω scans were performed by steps of 0.3° in ω in two groups of 606 frames (each with an exposure time of 60 seconds) at ϕ = 0° and 90°. The reflections from these frames are auto-indexed to determine the primitive unit cell. The primitive unit cell is then refined using least-squares and converted to the appropriate crystal system and Bravais lattice. This new cell is also refined using least-squares to determine the final orientation matrix for the sample. After the refined cell and orientation matrix have been determined, the experiment continues by collecting a sphere or hemisphere of data using an incremental scan method, collecting frames in 0.1° to 0.3° increments (over a certain angle while others are held constant). A complete data

collection may require anywhere between 6 hours to 24 hours, depending on the sample quality.

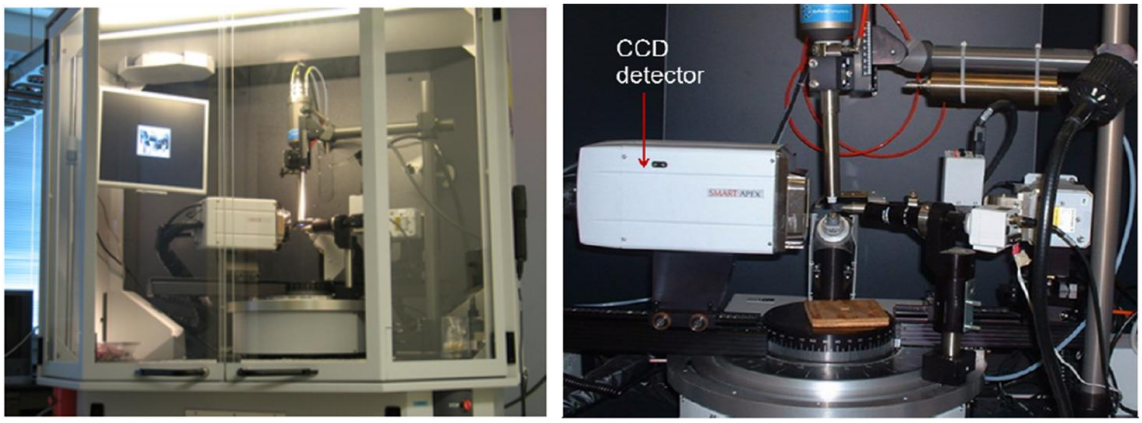

Figure 2.5: Bruker smart APEX CCD (left) and four-circle system with the CCD detector (right)

After the data have been collected, some corrections mentioned below must be applied to the entire data set. This is called data reduction as it also reduces the raw frame data to a smaller set of individual integrated intensities. These correction and processing procedures are typically part of the software package which controls and runs the data collection. The program is integrated with the APEX2 for the cell refinement and data reduction is SAINT.[77] The following corrections are involved in the data reduction process:

- Polarization correction (p) as the intensities of the reflected reflections are reduced due to polarisation.[73]
- Lorentz correction (L), which is related to the geometry of the collection mode.[73]
- Absorption correction, as part of the X-rays are absorbed by the atoms (especially heavy atoms) rather than scattered. As a result, intensities of the scattered rays are decreased. Absorption corrections were carried out by fitting a function to the empirical

transmission surface as derived from multiple equivalent measurements using SADABS incorporated in the package SAINT.[77]

The quality of the collected data is evaluated by the internal residual value (R_{int}) which depends on the observed structure factor, F_o.[73]

$$R_{int} = \frac{\sum |F_o^2 - F_{(mean)}^2|}{\sum F_o^2} \quad (2.6)$$

$$|F_o| = \sqrt{\frac{KI_{(hkl)}}{Lp}} \quad (2.7)$$

The observed structure factor, F_o, needs to be compared to the calculated structure factor, F_c, using a scaling factor K, to be able to conclude the success of the experiment. Therefore, to get F_c, after the corrections, the crystal structure should be solved by either the Patterson (used in systems with at least one heavy atom) or the Direct (used for compounds containing atoms with similar scattering factor) method using the SHELX package.[78, 79] In this project, only 3 samples were analysed by this technique and the structures were refined using the Direct method. The atomic positions are refined with the least square methods.

The quality of the refinement is evaluated by the difference between the observed and calculated structure factors called as the residual index or R factor (R_1) and weighted R factor (wR_2), w is the weighting parameter. The lower the R value the better is the refinement; however, the standard deviations in atomic positions, cell parameters etc., should be small too to conclude how good the refinement was.

$$R_1 = \frac{\sum ||F_o| - |F_c||}{\sum |F_o|} \quad (2.8)$$

$$wR_2 = \sqrt{\frac{\sum w(F_o^2 - F_c^2)^2}{\sum w(F_o^2)}} \quad (2.9)$$

The main issues in using single crystal X-ray diffraction are that in some cases it might be a challenge to get good quality single crystal of an appropriate size for this technique and presence of twin crystals. In such cases, one can do Rietveld refinement.

2.2.3 Rietveld refinement

Rieltveld refinement is a crystal structure refinement technique named after Dr. Hugo Rietveld, a Dutch crystallographer who discovered this technique in late 1960s. This technique was initially used to refine crystal structures from neutron diffraction as they have simple Gaussian peak shapes.[80] In 1977, Malmros and Thomas extended this method to powder X-ray diffraction using different peak-shape functions like the Lorentzian and pseudo-Voigt instead of Gaussian.[81]

To be able to apply this technique, a structural model from a database is needed based on the powder pattern of the sample. The powder pattern of the structural model is calculated and compared to the measured pattern of the sample. The profile of the model is refined by point-by-point comparison between the two profiles via a least-square refinement method. From the refinements, the peak positions, lattice parameters and the space group can be deduced. The model should have approximately the same unit cell dimensions, atomic coordinates as well as the same space group.

The proposed model is modified by changing the atomic positions, thermal displacement parameters and the fractional occupancy factor of each atom, then refined until the calculated pattern achieves a best fit match with the measured pattern. The difference between the observed and the calculated profiles is calculated as per *Equation 2.10* and shown on the refinement plot as 'obs-cal'.[80]

$$S_y = \sum_i w_i \left(y_{i(obs)} - y_{i(calc)}\right)^2 \qquad (2.10)$$

Where S_y = residual

$y_{i(obs)}$ = the observed intensity at the i^{th} step

$y_{i(calc)}$ = calculated intensity at the i^{th} step

w_i = weighting factor =/$y_{i(obs)}$

To judge if the 'best-fit' is achieved, the following *R*-values have been developed and are commonly used.[80]

$$R_F = \frac{\sum|\sqrt{I_{(hkl)(obs)} - I_{(hkl)(calc)}}|}{\sum\sqrt{I_{K(obs)}}} \quad (2.11)$$

Where R_F = *R*-structure factor

$I_{(hkl)}$ = intensity of the K^{th} Bragg reflection at the end of the refinement cycles

$$R_p = \frac{\sum|y_{i(obs)} - y_{i(calc)}|}{\sum|y_{i(obs)}|} \quad (2.12)$$

$$R_{wp} = \sqrt{\frac{\sum w_i(y_{i(obs)} - y_{i(calc)})^2}{\sum w_i(y_{i(obs)})^2}} \quad (2.13)$$

Where R_p = *R*-profile and R_{wp} = *R*-weighted profile

The smaller the *R* values, the better is the refinement; however, the success of the refinement is not judged only on the basis of the *R* value, it is a combination of a proper model, reasonable atomic positions, bond distances and bond angles.

2.2.3.1 Experimental

The X-ray diffractometer was aligned and calibrated and the PXRD data of the sample was collected over a long period (overnight). The PXRD data were then converted to a *.gs* file and refined using GSAS[82] (general structure analysis system) software via a graphical user interface EXPGUI.[83]

2.2.4 Energy dispersive X-ray analysis

This technique is both a qualitative and quantitative analysis used to identify the elements and the percentage of each element present in a compound. This is possible by measuring the intensity of the X-rays emitted by each element in the compound when the compound is bombarded by a high energy electron beam (one spot at a time) inside the

electron microscope. The bombarding electrons collide with the atoms in the sample and knock off one of the inner electrons; the vacancy left by the leaving electron is filled by one of the outer electrons (a higher energy electron). In so doing, the higher energy electron gives up some of its energy (energy liberated in form of X-rays) to occupy a lower level shell, the amount of energy released in this process depends on

- the transition itself (*Figure 2.6*). Which shells the electron is transitioning between (L → M, L → N, L → K, M → K or M → K etc.) as each transition would need a characteristic energy.
- the element. Every element releases X-rays with a characteristic wavelength.

Hence, measuring the amounts of energy present in the X-rays being released by a specimen during electron beam bombardment helps to identity the atom.

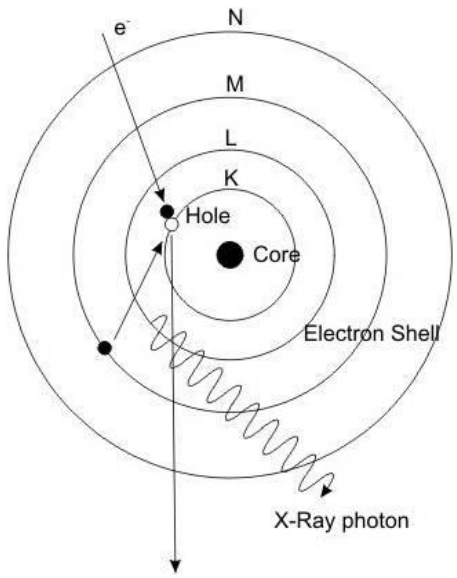

Figure 2.6[84]: Schematic diagram of principle of EDX

In this technique, the amount of energy liberated for each transition against how frequently the transition takes place is measured to get an EDX spectrum – a plot of *intensity* vs. *energy* (*Figure 2.7*). The area under each peak for a particular transition in an element would be proportional to the amount of the element present in the sample. Moreover, EDX analysis is considered as a qualitative analysis because it also provides

information on the homogeneity of the sample. One experiment involves shooting the high energy electron beam at least five different positions and if the atomic percents of the different elements present in the compounds at the five positions are close, the sample is considered as homogeneous. If the sample is not homogeneous, more shots are taken to be able to differentiate between the presence of secondary phases and the presence of off-stoichiometric compounds.

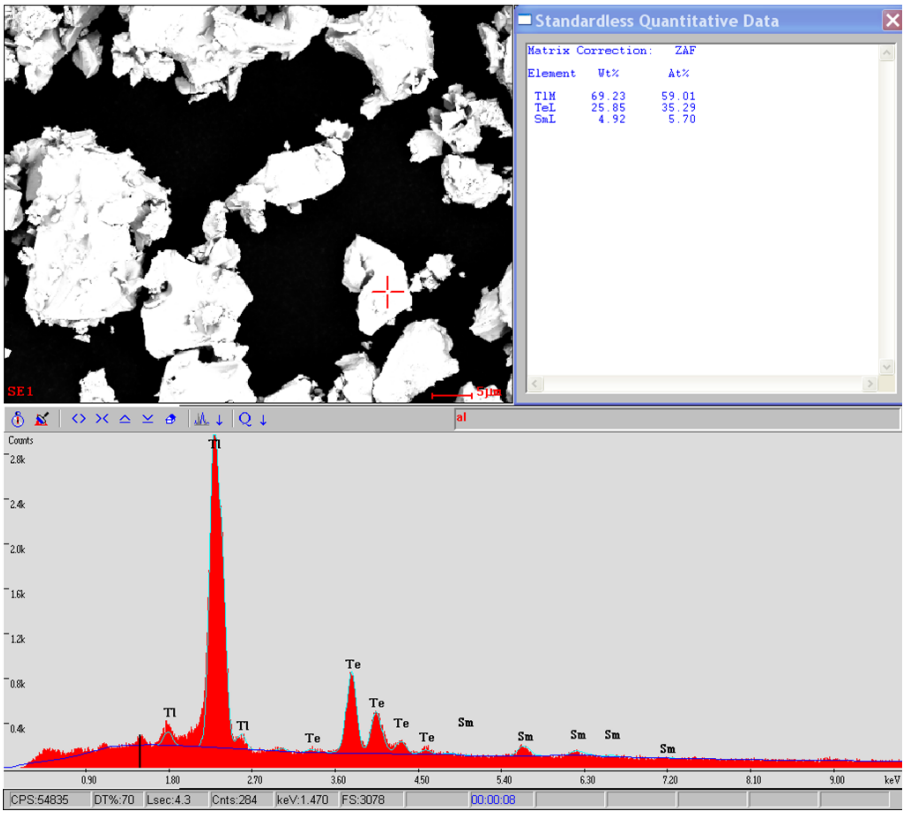

Figure 2.7: EDX spectrum

2.2.4.1 Experimental

The sample was ground to very fine powder and applied to a carbon sheet held on an aluminum holder. The sample holder with the sample on a carbon sheet is then put on a chamber stage (which can accommodate eight aluminum holders) which is part of the

spectrometer, a SEM (LEO 1530) integrated with an EDX (Pegasus 1200) (*Figure 2.8, left*). The chamber is evacuated once the door is closed. The experiment involves taking and magnifying images of the sample, adjusting the resolution and choosing the spots (based on appearances) to shoot with the electron beam. Once the high speed electron beam hit the sample, the X-ray liberated by the atoms at that spots are directed to the detector (*Figure 2.8, right*) which detect the X-ray energies corresponding to each transition and the number of times that transition occurs.

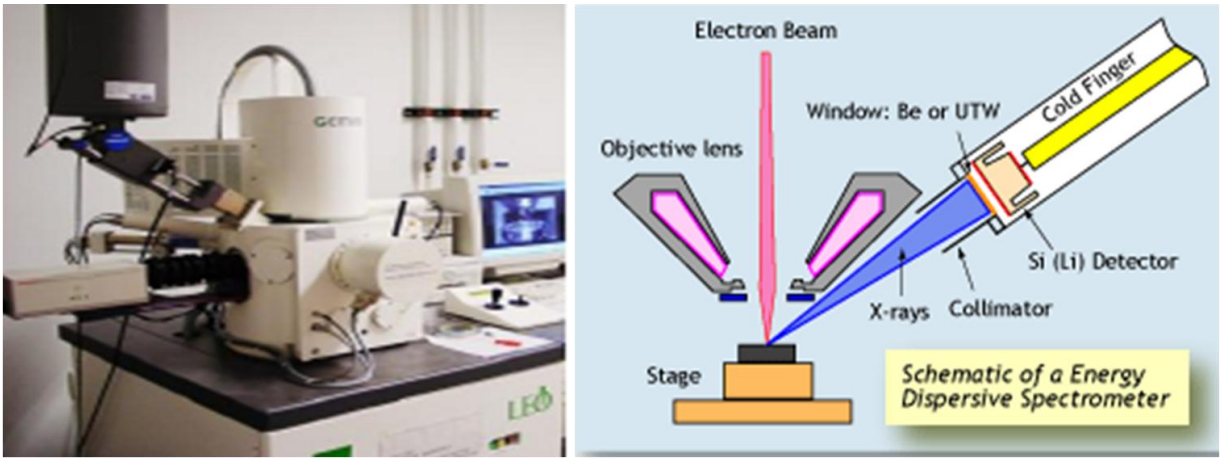

Figure 2.8: SEM (LEO 1530) with integrated EDX Pegasus 1200 (left) and schematic diagram of EDX experiment[85] (right)

2.2.5 Differential scanning calorimetric (DSC) analysis

This method is used to analyze the changes that take place when the sample is heated and cooled down, the possible changes are melting (change in state) or/and phase transition (decomposition). The sample and the reference are subjected to the same heating rate and cooling rate, the changes in the heat flow experienced by both of them are noted simultaneously. The reference does not undergo any changes in state over the temperature range used to examine the sample. The difference in heat flow between the sample and a reference standard is recorded by the computer connected to the instrument

(*Figure 2.9*). After the measurement is done, the software gives a plot of *difference in energy flow* vs. *T*.

The DSC plots show endothermic peaks during which heat is absorbed in processes like melting and exothermic peaks during which heat is liberated in processes like crystallization.[86] If the DSC plots have more than one endothermic or exothermic peak, the extra peaks might correspond to incongruent melting of the sample or presence of other phases. One can even identify phase transition or decomposition of the sample from the DSC-TG plots (TG plot shows the change in mass with temperature).

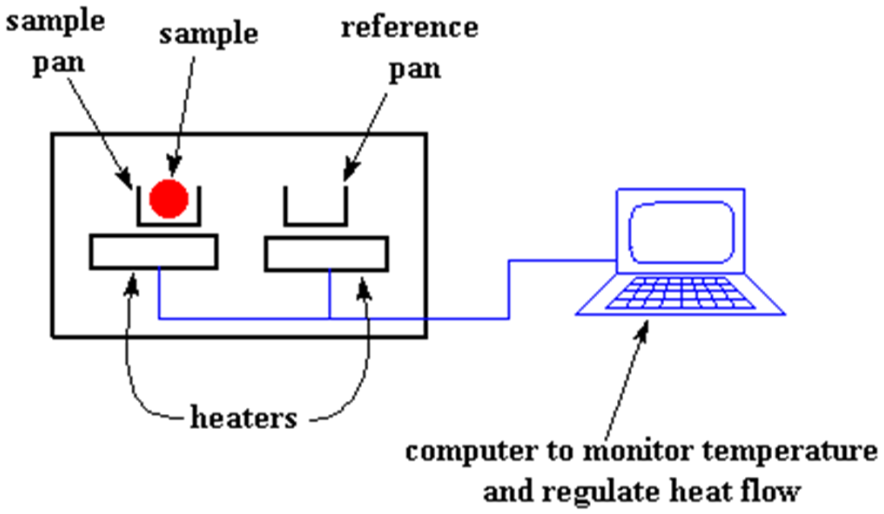

Figure 2.9[87]: Schematic diagram of the DSC set up

Figure 2.10 shows an example of the DSC plot indicating how the heat flow changes for glass.[86] There are three points to consider in this plot, the change in heat capacity, the crystallization (amorphous glass starts to crystallize) and the fusion (heat being absorbed as melting starts).

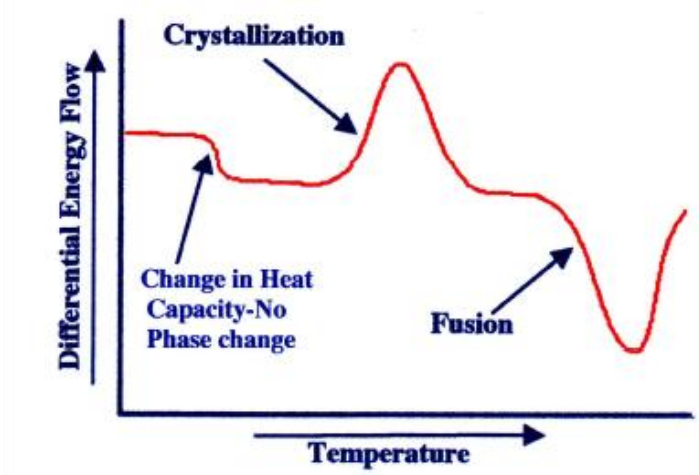

Figure 2.10[86]: DSC plot for glass

2.2.5.1 Experimental

Temperature-dependent combined DSC measurements were performed with the computer-controlled NETZSCH STA 409PC Luxx. The experiments were run from RT to ~ 1075 K with 25 mg - 56 mg of the phase pure sample under a constant flow of argon (80 ml/min) which also provides the balance flow (50 ml/min) at a heating rate of 20 K/min.

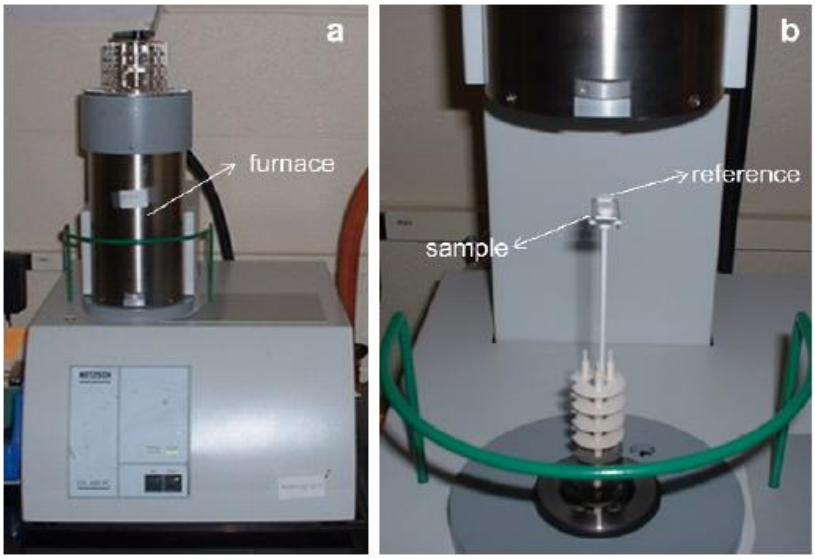

Figure 2.11: (a) NETZSCH STA 409 PC Luxx apparatus (b) sample holder

2.3 Physical property measurements

As mentioned earlier, after the compounds were synthesized and characterized, they were taken for physical property measurements. Since the project is about thermoelectric properties, the aim of the property measurements is to come up with a *ZT* value and the parameters required to be measured for that purpose are the Seebeck coefficient values, electrical and thermal conductivity values. All the measurements were done using the apparatus available in Kleinke's Lab at the University of Waterloo.

2.3.1 Seebeck coefficient and electrical conductivity measurement

As discussed in *Section 1.2.1.1*, when a conducting material is heated at one side, heat travels from the hot side to the cold side generating a potential difference. Therefore, heat energy is converted to electrical energy due to a temperature difference, this effect is called the Seebeck effect and the ratio of the potential difference developed to the temperature difference is called the Seebeck coefficient, *S* (*Equation 1.6*). Hence, *S*, can be obtained by measuring the temperature and potential differences between two points as shown in *Figure 2.13*.

Referring to *Section 1.2.1.2*, electrical conductivity, σ, can be obtained from the electrical resistance, *R*, and the dimensions of the pellet (*Equation 1.9*). Hence, the dimensions of the pellets should be measured and *R* should be calculated from Ohm's Law ($V = IR$). Since, *V* and *I* can be measured experimentally, σ can be obtained as shown in *Figure 2.14*.

2.3.1.1 Experimental

Seebeck coefficient values, *S*, and electrical resistivity, ρ, were measured simultaneously using the ULVAC ZEM-3 measuring system (*Figure 2.12(a)*). The samples were ground homogenously and pressed into 13*2*2 mm rectangular pellets which were annealed in evacuated and sealed silica tubes at 650 K. The sintered pellet

was placed in between the jaws in the furnace chamber, and between the jaws, two probes were brought in contact to the pellet. The jaws and the probes were closed tight enough to give a good contact (*Figure 2.12(b)*).

Figure 2.12: (a) ULVAC ZEM-3 instrument (b) Sample pellets in the heating chamber

The chamber was then closed, evacuated and filled with helium gas before starting the measurement. All the measurements were run under helium between RT and 550 K with ΔT of 15 K, 20 K and 25 K at the base temperature for every segment (7 segments: 300 K, 325 K – 525 K at 50 K intervals and 550K). *Figures 2.13* and *2.14* show the conceptual diagrams for the S and ρ measurement respectively.

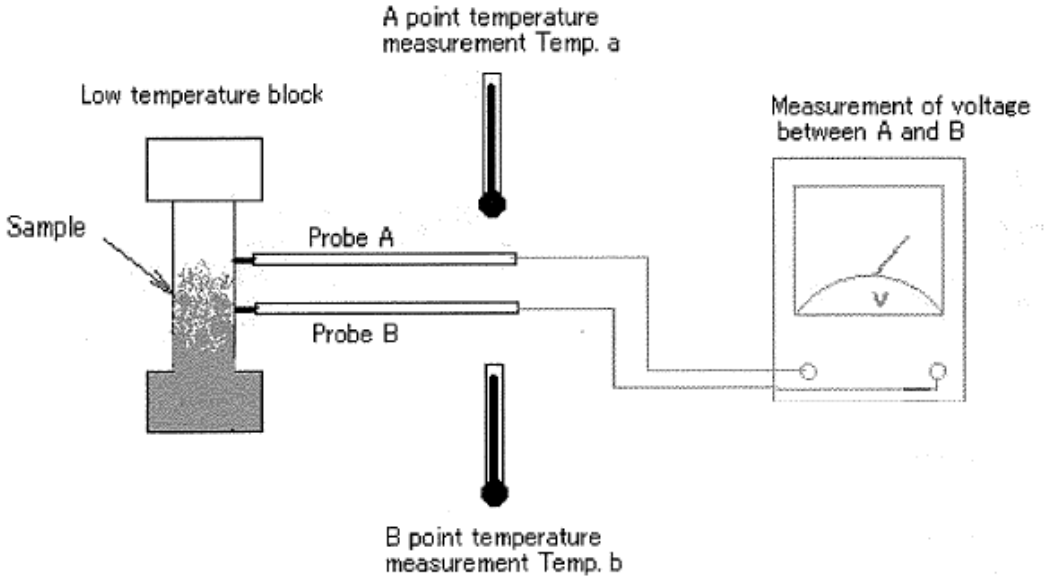

Figure 2.13[88]: Schematic diagram for *S* measurement

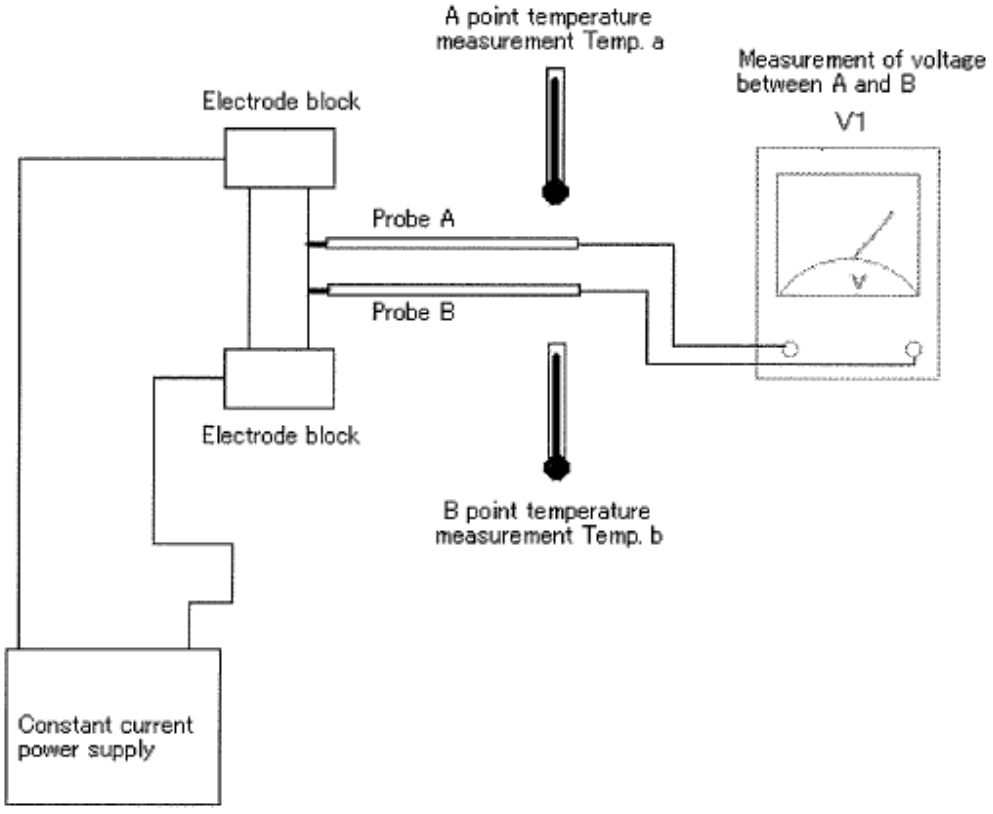

Figure 2.14[88]: Schematic diagram of ρ measurement

2.3.2 Thermal conductivity measurement

There are several methods to measure the thermal conductivity of bulk samples in the solid state.[31] Some methods are

- The steady-state method, whereby the temperature difference across the sample due to heating power is measured.
- The comparative method, which is same as the steady-state method; however a standard with comparable thermal properties to the sample to be measured is put in series between the heater and the sample.
- The Pulse-Power method, which has the same basic principle of the steady-state method; however, the temperature difference is small as the heating current is pulsed with a square wave.
- Laser-Flash diffusivity whereby the sample is irradiated with a laser at one side and monitored by an IR detector at the opposite side (*Figure 2.15*). As the thermal conductivity is a measure of how good or fast a material conduct heat, the IR detector detects the temperature rise at the opposite side as a function of time. The time taken for the opposite side to reach half the maximum temperature rise ($t½$) is measured by the thermal conductivity machine. $t½$ is related to the thermal diffusivity (how fast the heat diffuse into the material), D, and the thickness, L, of the pellet according to the *Equation 2.14*.

$$D = 0.1388\frac{L^2}{t½} \tag{2.14}$$

The experimental thermal conductivity can be calculated according to *Equation 2.15*.

$$\kappa = DdC_p \tag{2.15}$$

$$C_p = \frac{3R}{M_m} \tag{2.16}$$

Where d = density of the material

M_m = averaged molar mass = molecular weight/no. of atoms

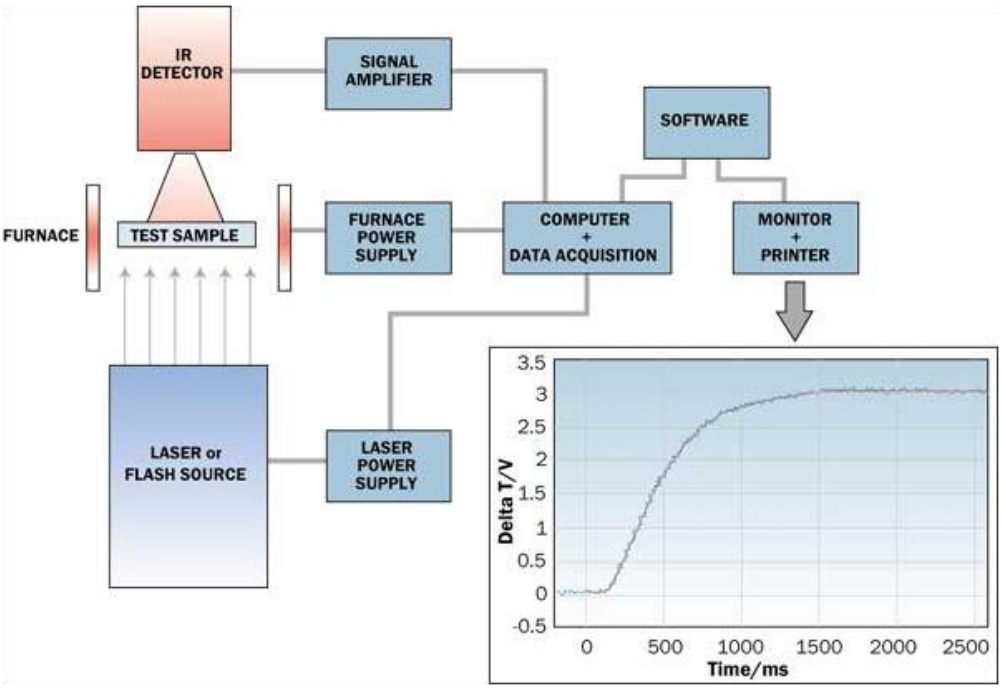

Figure 2.15[89]: Schematic diagram of the Flash-Laser diffusivity system and the temperature rise curve

2.3.2.1 Experimental

In this study, all the measurements were done through the Laser-Flash diffusivity method using the Flash line 3000 thermal diffusivity system (ANTER corp.) shown in *Figure 2.16*.

The samples are pressed in a cylindrical pellet (diameter and thickness of 8 mm and 2 mm respectively) and sintered in a sealed and evacuated silica tube at 650 K. The densities of the pellets were then measured by applying the formula, density = mass/volume. The pellets were then sprayed with graphite and left to dried. In the meantime, the IR detector was cooled with liquid nitrogen for about 1 hr. Once the pellets were dried, they were put in a carousel which was then placed in the furnace chamber. The chamber was closed, evacuated and purged with argon; the experiment was run under constant flow of argon from 400 K to 550 K at 25 K intervals.

Figure 2.16: Flash line 3000 thermal diffusivity system

2.3.3 Magnetic properties measurement

The overall magnetic field strength of atoms or ions containing paired electrons (which would spin and orbit in opposite direction, hence, would have no net electron spin) is zero and such materials are called diamagnetic.[90] However, when placed in an external magnetic field, diamagnetic materials do produce a slight magnetic field that opposes the external magnetic field and are pushed out of a magnetic field. If a diamagnetic material is placed in a strong external magnetic field, the magnetic field strength inside the material will be less than the magnetic field strength in the air surrounding the material. The slight decrease in the field strength is the result of realignment of the electrons in the orbit motion.[90]

Atoms or ions having unpaired electrons in their outermost shell with random orientations of the electron spin in absence of an external magnetic field are known as paramagnetic and are attracted slightly by a magnetic field.[90, 91]

Other orientation of the unpaired electrons gives rise to different types of magnetism briefly explained below and illustrated in *Figure 2.17 (a)*.[29, 90, 91] In ferromagnetic material, all the spins are aligned in the same manner, they experience

strong attraction to a magnet as their net electron spin is higher. In anti-ferromagnetic material the unpaired electrons are aligned in equal number of spins in each direction, anti-ferromagnetic materials are weakly attracted to a magnet. Ferrimagnetisms occurs when the unpaired electrons are held in a pattern with some up and some down, however there are more spins held in one direction.

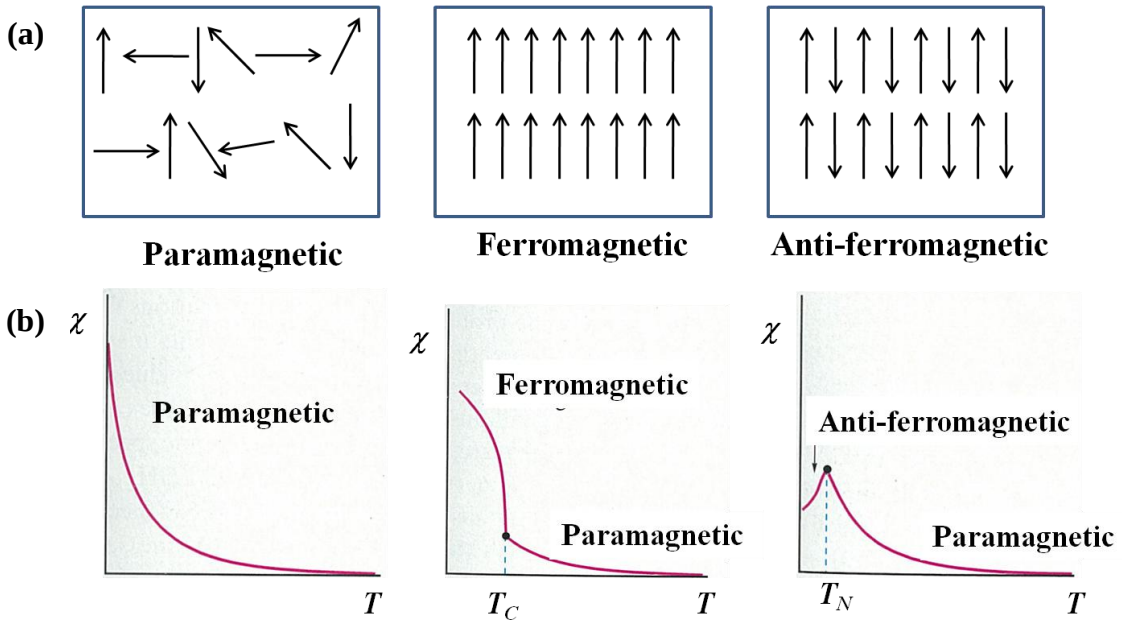

Figure 2.17[29]: (a) Representation of different types of magnetism (b) plots of/χ vs. *T*

In some cases, a material can be changed from one type to another as a function of temperature as shown in *Figure 2.17 (b).*[29] T_c is the Curie temperature at which ferromagnetic ordering occurs and T_N is the Neel temperature at which antiferromagnetism occurs.[29]

Magnetic properties are important in our daily life as the principle of magnetism is applied in many of our routine activities like watching TV, playing music, using computers/laptop, iron materials are used for those purposes. The principle of magnetism is even applied in the medical field, it is the basis of the MR imaging in diagnostic radiology, the imaging process is principally performed with the hydrogen nucleus.[90]

Magnetic properties are popular among the f-block metal compounds as all the Ln^{3+} ions contain unpaired electrons and are paramagnetic except Y^{3+}, La^{3+} and Lu^{3+}.[92] Rare Earth Magnets like NdFeB and SmCo are used commercially already.[93] NdFeB magnets are quite common and relatively cheap, used for high performance applications like in MRI machine, magnetic holding systems like latches, shutters and loudspeaker-type actuator.[93] On the contrary, SmCo magnets are more expensive and used where performance and reliability is a priority over cost like in aeronautic and military applications.[93]

The critical magnetic characteristics of a material are magnetisation, coercively and stability.[93, 94] The magnetisation is the magnetic moment per volume, which measures the extent a material can be magnetized.[94] The Magnetic moment (μ_{eff}) can be obtained experimentally from the magnetic susceptibility (χ) which expresses the ability of an applied field to magnetize a specified quantity of material. Molar magnetic susceptibility, atomic magnetic susceptibility and volume magnetic susceptibility give the magnetizability of a material per unit molecular weight, unit atomic weight and per unit volume respectively.

$$\mu_{eff} = 2.828\sqrt{\chi_m T} \tag{2.17}$$

Where μ_{eff} = effective magnetic moment

χ_m = molar susceptibility can be obtained experimentally

The experimental μ_{eff} can be compared to the theoretical values calculated according to *Equation 2.18* for d-block systems and *Equation 2.19* for f-block systems.

$$\mu_{eff} = \sqrt{n(n+2)} \tag{2.18}$$

Where n = number of unpaired electrons

$$\mu_{eff} = g_J\sqrt{J(J+1)} \tag{2.19}$$

Where $g_J = 1 + \{S(S+1) - L(L+1) + J(J+1)/2J(J+1)\}$

S = max spin multiplicity = $\sum m_s$

L = maximum Orbital Angular Momentum = $\sum m_l$

J = Total Angular Momentum = (L+S), (L+S)-1, (L+S)-2, ……. (L-S), for less than half filled shell, J = minimum value, for more than half filled shell, J = maximum value.

In this study, the magnetic properties of specific compounds (Tl_9LnTe_6, Ln = Ce, Pr, Sm and Tb) were measured to check their oxidation state. Since magnetic properties depend on the interaction of unpaired electrons, once the experimental magnetic moment is obtained through magnetic susceptibility, it can be compared to the theoretical magnetic moment, μ_{eff}. μ_{eff} may be used to deduce the number of unpaired electrons and hence the electron configuration can be known leading to the oxidation state.

2.3.3.1 Experimental

All the measurements were done at McMaster University using a Quantum Design MPMS (Magnetic Property Measurement System) SQUID (Superconducting Quantum Interference Device) magnetometer (*Figure 2.18*).

The moment, M, of the samples was measured as a function of the magnetic field, H, at a constant temperature (T) of 2 K and as a function of T at a fixed H of 100 Oe for Ce and Tb and 1000 Oe for Sm and Pr using the Quantum Design MPMS SQUID magnetometer (*Figure 2.18*).

The susceptibility, χ, at each temperature was calculated as the ratio of M:H where the applied magnetic filed, H, is constant. χ_m was therefore calculated as a function of T and applying Curie-Weiss fit or Modified Curie-Weiss fit, the μ_{eff} of the sample was obtained.

Figure 2.18: Quantum Design MPMS SQUID magnetometer (McMaster University)

The magnetometer consists of a superconducting magnet and a pick-up coil (*Figure 2.19(a)*). The superconducting magnet is a solenoid made of a superconducting wire cooled with helium. The principle of the measurement is that the sample is moved through a pick-up coil (*Figure 2.19(b)*). The magnetic moment of the sample induces an electric current in the pick-up coil system causing a change in magnetic flux in these coils. The change in the current in the coil produces a variation in the SQUID output voltage that is proportional to the magnetic moment of sample.

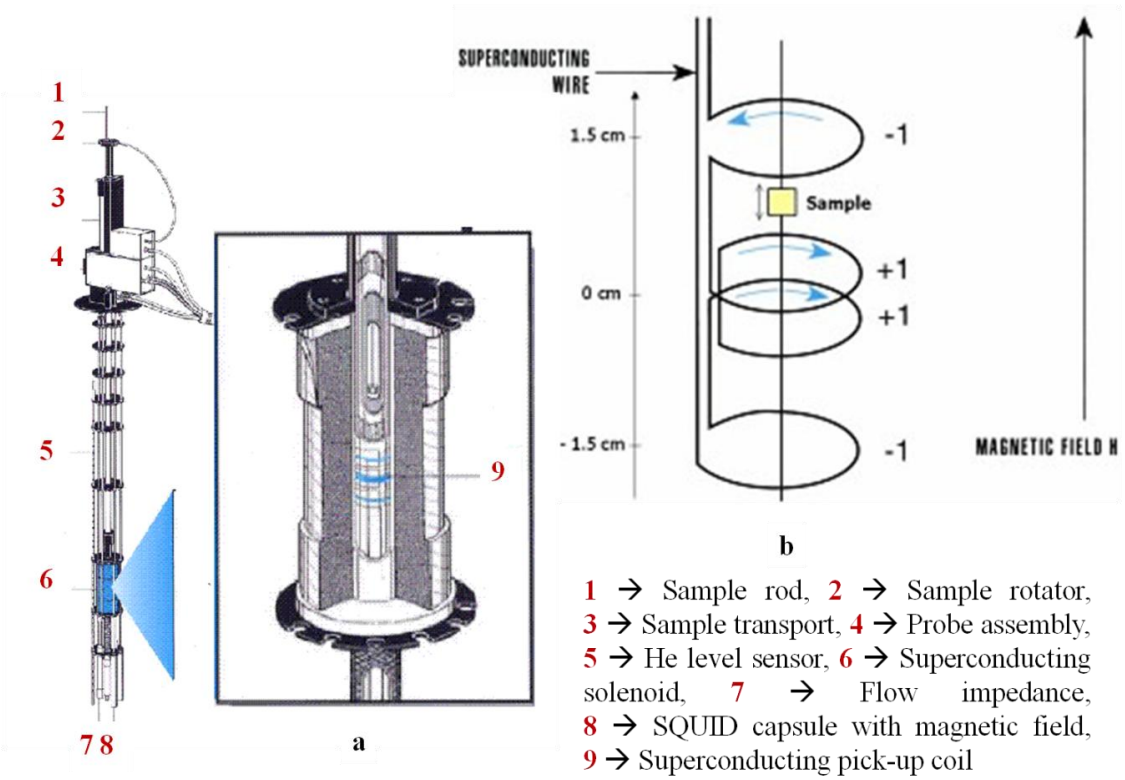

Figure 2.19: Schematic diagram of (a) The SQUID magnetometer[95] (b) pick-up coil[96]

2.4 Band structure calculation

The carriers in a material behave like waves; hence, their wave properties can be described by the Schrödinger Equation.[29, 97]

$$H\psi = E\psi \tag{2.20}$$

Where H = Hamiltonian operator = $\frac{-h^2}{8\pi^2}\left(\frac{\partial^2}{\partial x^2} + \frac{\partial^2}{\partial y^2} + \frac{\partial^2}{\partial z^2}\right) + V$

E = kinetic energy = $\frac{1}{2}mv^2$

ψ = wave function

V is the potential energy, which is the electrostatic force of attraction between the nucleus and the electron. Since the carriers are moving particles, their potential energy is assumed to be 0.[97]

The Schrödinger equation describes the atomic orbital, ∅, containing an electron of effective mass, *m**, with an energy, *E*, and a wave vector, *k*. Therefore, solution of the Schrödinger equation gives the energy[29] and wave function[98] of the particle:

$$E = \frac{k^2h^2}{8\pi^2m^*} \tag{2.21}$$

$$\psi = \sum_n e^{iknа}\ \emptyset_n \tag{2.22}$$

Where *h* = Planck's constant

n = 0, 1, 2, 3, ……

The magnitude of the wave vector is related to the wavelength, λ, ($k = \frac{2\pi}{\lambda}$) and its direction shows the propagation of the electrons in the Brillouin zone with lattice spacing *a*, $\frac{-\pi}{a} \leq k \leq \frac{\pi}{a}$. *a* is so small in solid state inorganic compounds that the atomic orbitals overlap to give a band instead of a molecular orbital, which is the case for molecular systems.

For example, considering the simplest case, a 1D linear chain of hydrogen atom with lattice spacing *a*. The H-atoms are labeled by *n* (*n* = 0, 1 - 4) and the *1s* orbital of hydrogen atoms are $\emptyset_n$ (*Figure 2.20*).

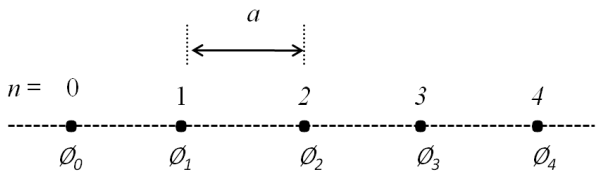

Figure 2.20: 1D-linear chain of hydrogen atoms

The *1s* orbital containing its electron could overlap either in phase or out of phase depending on their positions **(Γ, X** etc**)** in the Brillouin Zone (*Figure 2.21*).

At Γ, $k = 0$, $\psi = \sum \emptyset_n = \emptyset_0 + \emptyset_1 + \emptyset_2 + \emptyset_3 + \emptyset_4 + \ldots\ldots\ldots$

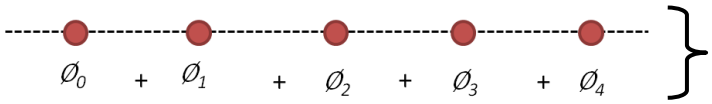

At X, $k = \frac{\pi}{a}$, $\psi = \sum(-1)^n \emptyset_n = \emptyset_0 - \emptyset_1 + \emptyset_2 - \emptyset_3 + \emptyset_4 - \ldots\ldots\ldots$

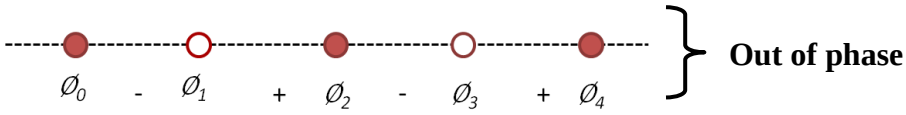

Figure 2.21: Interactions of the 1s hydrogen orbitals in the linear chain

Therefore, for the 1D linear hydrogen chain, at the centre of the Brillouin zone, **Γ**, the orbitals are in phase giving a more stable (lower energy) bonding interaction with respect to the less stable (higher energy) anti-bonding interaction, which occurs at **X**. The band structure (a plot of *E* vs. *k*) can be constructed for the 1D linear hydrogen chain (*Figure 2.22(a)*). Unlike the hydrogen chain, the crystal structures of compounds are 3D based on the Bravais lattices, and different Bravais lattices will have different Brillouin zones and hence, different *k*. Hence, the band structure of different systems will be different.

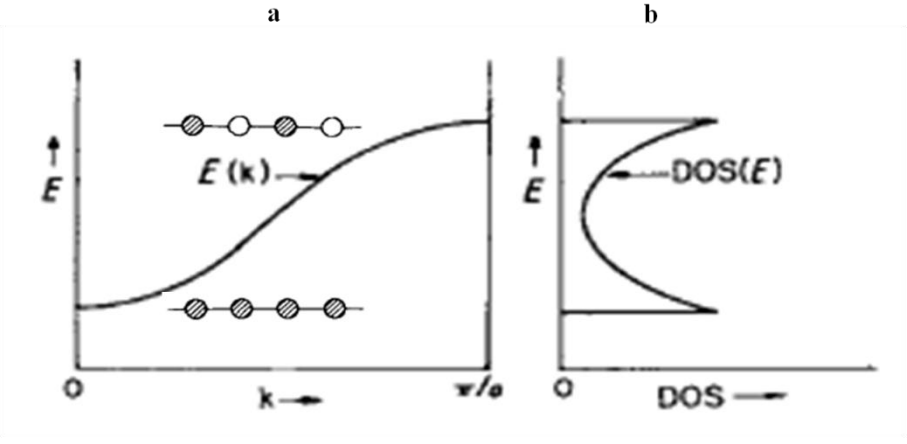

Figure 2.22: (a) Band structure (b) *DOS* curve of a chain of hydrogen atoms

From the band structure, the following important information can be extracted:

- The density-of-states plot (*DOS* curve), which is a plot of *E* vs. *number of states*, *N(E)dE*, can be calculated.[71] (*DOS(E)dE = number of levels between E and E+dE* → *DOS* counts levels and plots distribution of electrons in energy).[98] The inverse of the slope of the bands in the band structure is proportional to the *DOS* (flatter band, higher *DOS*), that's how *Figure 2.22 (b)* is related to *Figure 2.22 (a)*.[98] Since the *DOS* is related to *S* and σ as discussed in *Sections 1.2.1.1* and *1.2.1.2*, knowing the *DOS* of a material helps to tune its properties through doping.
- From the position of the Fermi level in the band structure and *DOS* curve, one can predict electronic properties of materials.

The bandwidth of the band depends on the interaction of the orbitals involved (smaller interatomic spacing leading to better overlap and to a bigger band width (*Figure 2.23*)).[98] This point is important and discussed in *Chapter 3* to interpret electronic properties of some materials. Therefore, calculation of the band structure and *DOS* curve is very important, that's why some calculations (LMTO[99] and Wien2*k* package[100]) were done in this study.

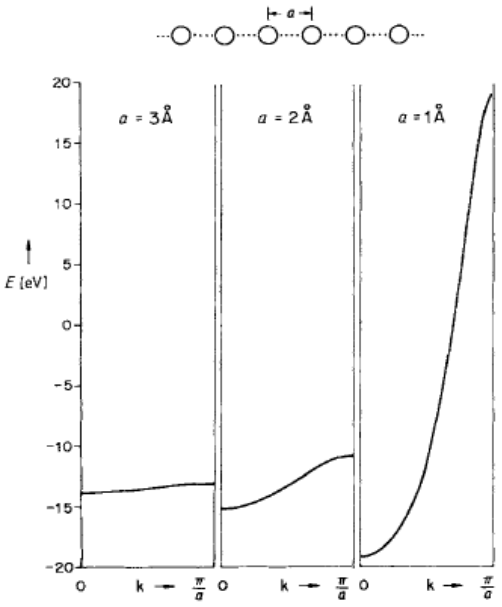

Figure 2.23[98]: Band structure of a chain of hydrogen atoms spaced 3 Å, 2 Å and 1 Å apart

2.4.1 LMTO calculations

Some calculations ($Tl_{10-x}La_xTe_6$) were done by using the LMTO (Linear Muffin Tin Orbitals) program controlled under the LINUX computer operating system.[99] The LMTO program uses the density functional theory (DFT) which is based on the Hohenberg and Kohn theory about the relation between the total energy of a system containing particles interacting with each other and the density distribution.[101] The program calculates the energies and density-of-states by solving the Kohn-Sham equation instead of the Schrödinger equation. [102] According to Kohn-Sham, a set of single particle equations gives the right electron density and total ground state energy of the particle interacting particle system.[102] Hence the calculation needs some approximations for the exchange correlation energy in the DFT to be able to map an interacting system onto a non-interacting system quite closely. The approximations are the atomic-spheres approximation (ASA)[103] and the local density approximation (LDA).[104]

2.4.2 WIEN2*k* calculations

In this study, the DOS of the highly correlated f-electron system were calculated using the WIEN2*k* package as the LMTO method did not work. In this approach, the onsite intra-atomic Coulomb repulsion, *U*, between electrons occupying the localized 4f states in lanthanoids or narrow 3d band in transition-metal compounds and exchange parameter, *J*, are included.[105]

$$U = E(d^{n+1}) + E(d^{n-1}) - 2E(d^n) \quad (2.23)$$

$$J = (F^2 + F^4)/14 \quad (2.24)$$

3 ANALYSIS AND ELECTRONIC STRUCTURE OF $Tl_{10-x}Ln_xTe_6$

Ten new phases, $Tl_{10-x}Ln_xTe_6$, $0.25 \leq x \leq 1.32$, Ln = La, Ce, Pr, Nd, Sm, Gd, Tb, Dy, Ho and Er, were synthesized using the same method as described in *Section 2.1.1*. The compounds were analyzed and characterized as mentioned in *Section 2.2* and the physical properties were measured according to *Section 2.3*.

In this chapter the analysis will be described in two parts, firstly the analysis of the lanthanum phase will be discussed. Then a general discussion on the analysis of the rest of the compounds studied in this thesis will be covered as follows:

- as *x* increase within a particular phase for a given Ln
- across the Ln series of a stoichiometric compound Tl_9LnTe_6.

Similarly, the electronic structures of the lanthanum phase as *x* increases will be discussed first followed by the electronic structures across the series for Tl_9LnTe_6.

3.1 Analysis of $Tl_{10-x}La_xTe_6$, $0.25 \leq x \leq 1.15$

3.1.1 EDX and DSC Analyses

The EDX data of samples $Tl_{9.8}La_{0.2}Te_6$ and Tl_9LaTe_6 showed that no heteroelements were present in either case. The atomic percents of Tl, La and Te over five shots indicated that the compounds were homogenous. The Tl : La : Te ratios of $Tl_{9.75}La_{0.25}Te_6$ and Tl_9LaTe_6, as averaged over several crystals, were concluded to be close to what is expected as shown in *Table 3.1*.

The stability of $Tl_{9.75}La_{0.25}Te_6$ and Tl_9LaTe_6 were confirmed by the DSC analysis and their proposed melting points are 718 K and 802 K respectively. *Figure 3.1* shows the DSC plots of the two compounds. It is postulated that as the amount of lanthanum increases in the structure, the melting point of the compounds increases, most probably due to decreasing polarizing power[91] from Tl^{3+} to La^{3+}, as La^{3+} (1.172 Å)[106] is bigger than Tl^{3+} (1.025 Å).[106]

Table 3.1: EDX data of $Tl_{9.75}La_{0.25}Te_6$ and Tl_9LaTe_6

Compound	Experimental atomic percent (Nominal atomic percent)		
	Tl	**La**	**Te**
$Tl_{9.75}La_{0.25}Te_6$	62.99 (60.94)	1.97 (1.56)	35.04 (37.5)
Tl_9LaTe_6	56.44 (56.25)	6.13 (6.25)	37.43 (37.5)

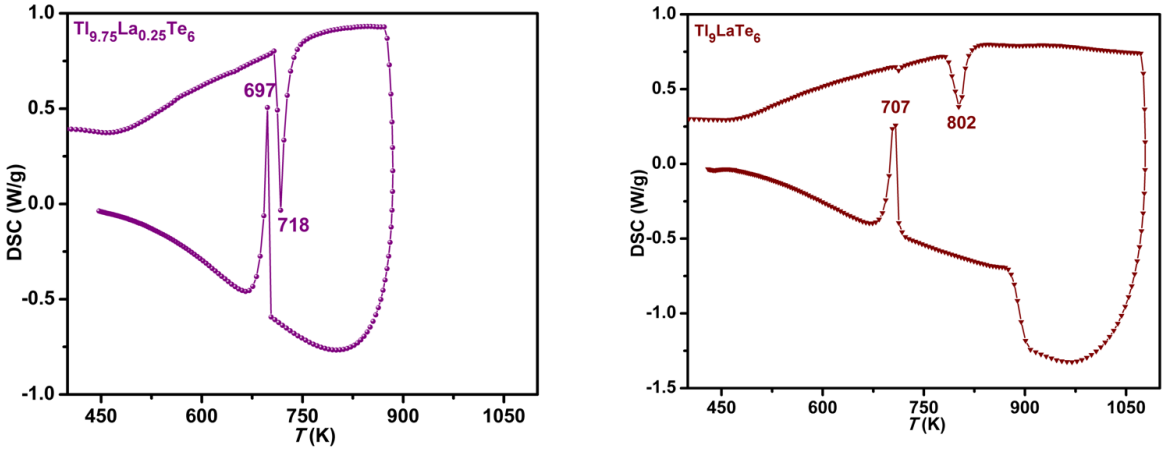

Figure 3.1: DSC plots of $Tl_{9.75}La_{0.25}Te_6$ (left) and Tl_9LaTe_6 (right)

3.1.2 XRD Analysis and Structure determinations of $Tl_{10-x}La_xTe_6$

As discussed in *Section 1.3.5.4*, Tl_9BiTe_6 exhibited a quite promising *ZT* value of 1.2 at 580 K on a zone refined pellet. As mentioned earlier in *Section 1.3.5.4*, Tl_9BiTe_6 belongs to the Tl_5Te_3 family, which has a body centered tetragonal structure with space group, *I4/mcm* with two Tl and two Te sites, and no Te–Te bonds. $Tl_{10-x}La_xTe_6$ compounds are postulated to have the same structure type.

3.1.2.1 XRD Analysis of $Tl_{10-x}La_xTe_6$

All the compounds synthesized were analyzed by powder X-ray diffraction as discussed in *Section 2.2.1.1*. The patterns obtained were compared to that of Tl_5Te_3[69, 107] or Tl_9BiTe_6.[69, 108]

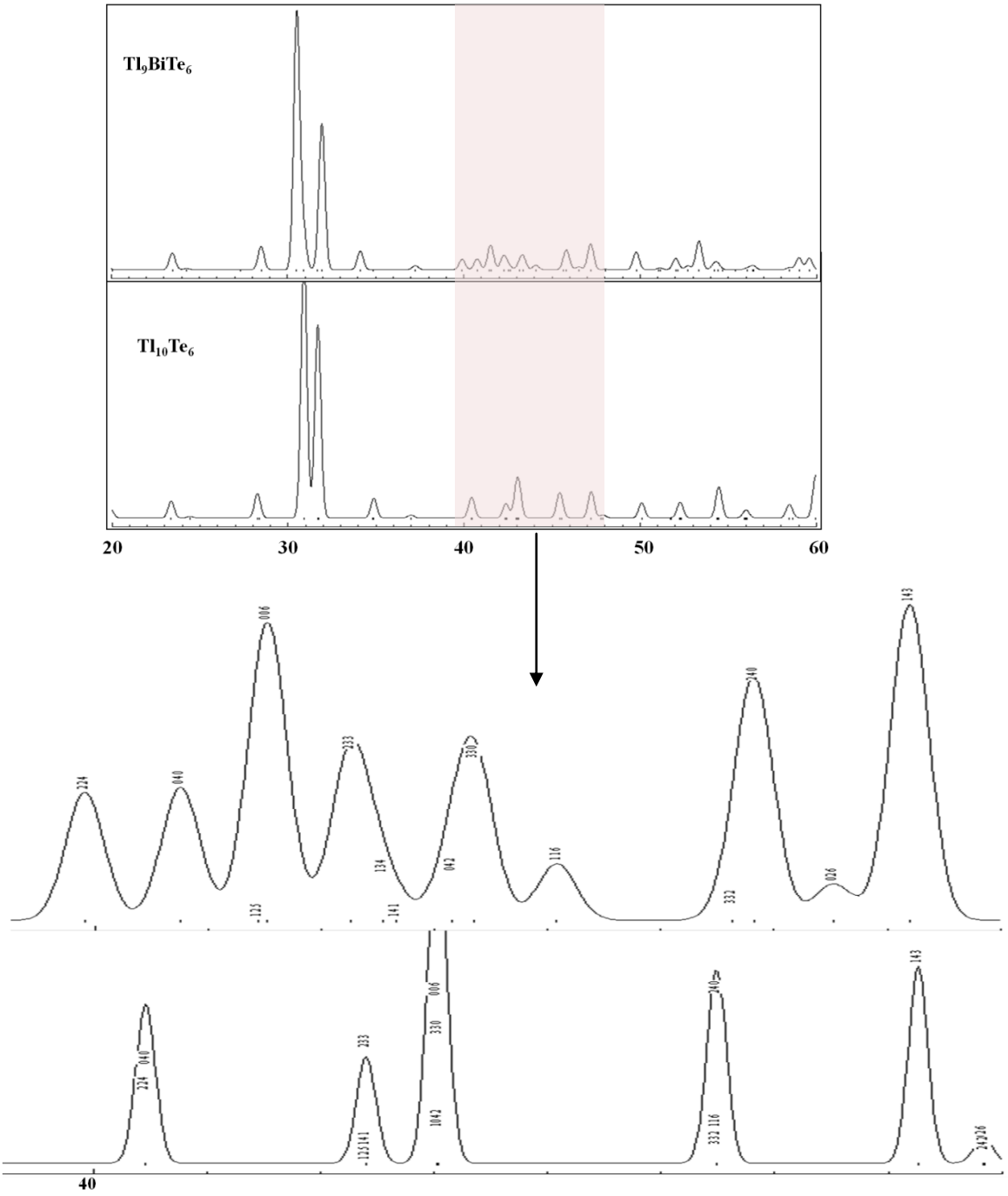

Figure 3.2: XRD patterns of $Tl_{10}Te_6$[69, 107] and Tl_9BiTe_6[69, 108]

The two patterns (*Figure 3.2*) are of the same structure type, the highlighted part shows that there is a slight shift in the 2θ values between the two patterns due to their different lattice parameters (Tl_5Te_3[69]: a = 8.930(2) Å, c = 12.589(4) Å and Tl_9BiTe_6[66, 109]: a = 8.855(2) Å, c = 13.048(4) Å). It is also noteworthy that there was an insignificant difference in intensity due to the very small difference in the scattering factor of Bi and Tl as they have atomic numbers that are 83 and 81 respectively.

Since, compounds of the series $Tl_{10-x}La_xTe_6$, are expected to be isostructural to Tl_5Te_3, they are expected to have same patterns as either Tl_5Te_3 or Tl_9BiTe_6. It is observed that as x increases, the patterns match that of Tl_9BiTe_6 more closely as shown in *Figure 3.3*. Slight shifts in the 2θ values were also observed as more lanthanum was incorporated in the structure, for the same reason: the change in lattice parameters. The lattice parameters of three compounds from this series ($Tl_{9.72(6)}La_{0.28}Te_6$ and $Tl_{9.37(2)}La_{0.63}Te_6$, *Table 3.3*; $Tl_{8.96(3)}La_{1.04}Te_6$, *Table A.2*) were obtained from the single crystal X-ray diffraction data. Moreover, lighter lanthanum (mass number 138.91 g/mol) replacing the heavier thallium (mass number 204.38 g/mol) results in a greater difference in scattering factor. As a result, a greater difference in the peak intensities are observed as more La is incorporated.

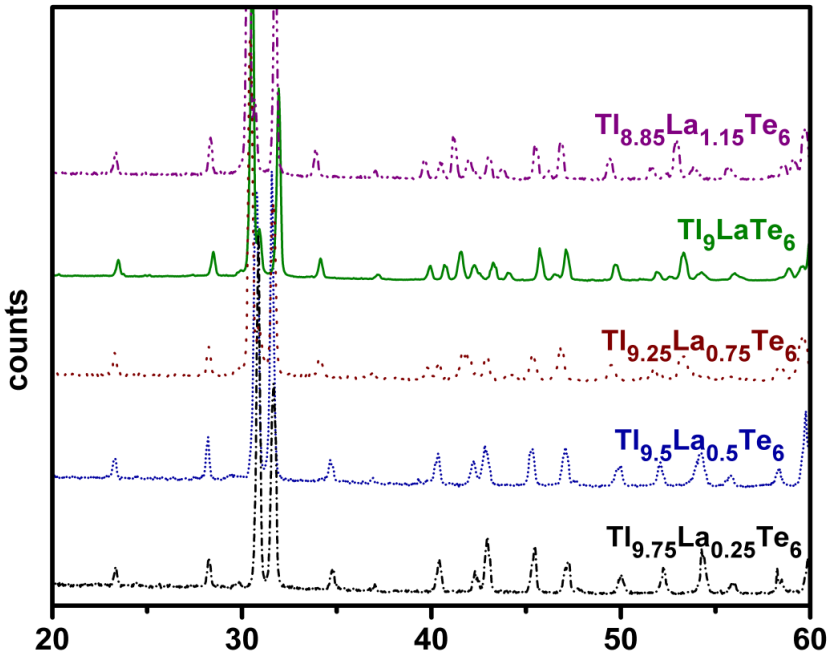

Figure 3.3: XRD patterns of $Tl_{10-x}La_xTe_6$, $0.25 \leq x \leq 1.15$

3.1.2.2 Structure determinations of $Tl_{10-x}La_xTe_6$

To gather further evidence of the phase range and study the changes arising, three different samples were selected for crystal structure analysis. Crystals were selected from the phase pure samples with $x = 0.2$ and $x = 1.0$ as well as from an inhomogeneous sample from a crystal growth experiment using the Bridgman method with $x = 1.0$. Lorentz, polarization and absorption corrections were done to all the data collected.

The structure refinements were carried out with the SHELXTL program package.[78] The systematic absences restricted the choice of space groups to *I*4*cm* and *I*4/*mcm*, noting that the latter was adopted both by Tl_5Te_3[110] and Tl_9BiTe_6.[111] Test refinements in *I*4*cm* and *I*4/*m*, as suggested for $Tl_{8.93}Sb_{1.07}Te_6$, showed no evidence of long range ordering; therefore, *I*4/*mcm* was identified as the correct space group.[108] Using the atomic positions published for Tl_9BiTe_6[69] and assuming mixed Tl/La occupancies on the *4c* (M1) site, the refinements converged smoothly without showing any anomalies. No La incorporation was detected on the *16l* (Tl2) site in any case. The M1 site of $Tl_{10-x}La_xTe_6$ is mixed occupied by Tl and La, comparable to Tl_9BiTe_6[66] with a 1:1 mixture of Tl and Bi on that position, which is coordinated by six Te atoms forming a tetragonally compressed octahedron. In Tl_5Te_3, the Tl1–Te distances are 3.15 Å (Tl1–Te1, 2×) and 3.36 Å (Tl1–Te2, 4×), with the shorter distances running parallel to the *c* axis and the longer ones parallel to the *a,b* plane.[110] These octahedra form a linear chain along the *c* axis via corner condensation (*Section 1.3.5.4*, *Figure 1.18*). The octahedra become increasingly regular with increasing La concentration, culminating in M1–Te distances of 3.22 Å (2×) and 3.36 Å (4×) (*Table 3.2*). The increasing regularity of the $(M1)Te_6$ octahedron is caused by the spherical shape of the La^{3+} cation, and leads to anisotropic changes of the *a* and *c* axes upon La incorporation, namely a small decrease of the *a* axis and a larger increase of the *c* axis (*Table 3.2*).

Table 3.2: Selected interatomic distances [Å] of $Tl_{10-x}La_xTe_6$, x = 0.28, 0.63.

Interaction		$Tl_{10}Te_6$[110]	$Tl_{9.72(6)}La_{0.28}Te_6$	$Tl_{9.37(2)}La_{0.63}Te_6$
M1–Te1	2×	3.147(1)	3.1530(2)	3.2235(4)
M1–Te2	4×	3.361(1)	3.3690(8)	3.3604(4)
Tl2–Te2		3.159(1)	3.159(2)	3.1871(8)
Tl2–Te2	2×	3.389(1)	3.3859(2)	3.4407(6)
Tl2–Te1	2×	3.600(1)	3.6168(9)	3.6157(4)
Tl2–Tl2		3.459(2)	3.499(2)	3.4976(9)
Tl2–Tl2	2×	3.496(2)	3.519(2)	3.5159(7)
Tl2–Tl2		3.728(1)	3.725(2)	3.7220(9)

These distances are in the expected range of La–Te distances, as a comparison with $La_{3-x}Te_4$ reveals, wherein the La atoms are eightfold coordinated by Te atoms at distances of 3.24 Å and 3.42 Å.[112]

The coordination of the Tl2 atom is highly irregular with five Te atoms at distances between 3.19 Å and 3.62 Å in Tl_9LaTe_6 and between 3.16 Å and 3.62 Å in $Tl_{9.72}La_{0.28}Te_6$ (*Figure 3.4*). The Tl2 atoms surround the Te1 atoms in the form of a square antiprism and the M1 atoms in form of a cube (the cubes are shown in *Figure 1.18*). Thereby the Tl2 atoms build linear chains along the *c*-axis of alternating, face-sharing square antiprisms and cubes that are centered by the $(M1)Te_6$ chains. A variety of likely significant Tl2–Tl2 distances between 3.46 Å and 3.73 Å occur in the structure of Tl_5Te_3, as often observed in thallium tellurides.[113-116]

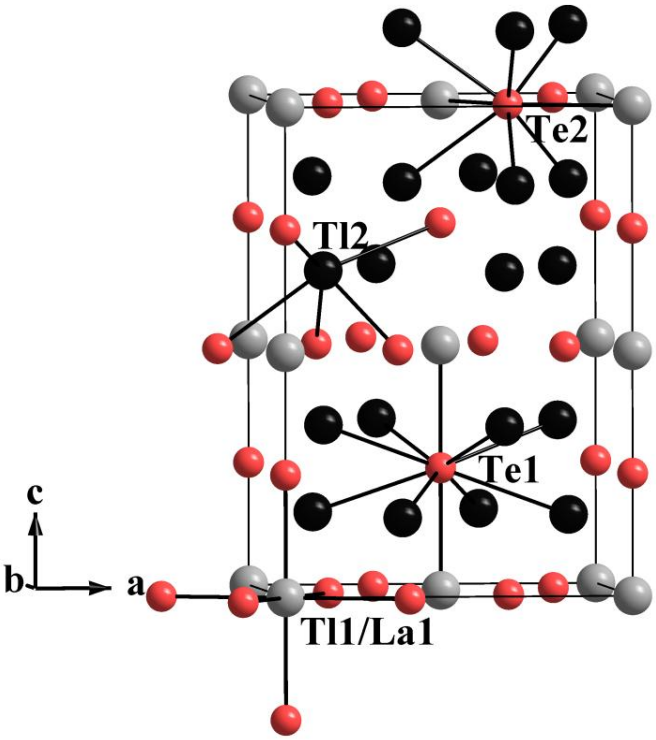

Figure 3.4[117]: Crystal structure of $Tl_{9.72}La_{0.28}Te_6$

The lattice parameters were in accord with the expected body centered tetragonal Bravais lattice. The data obtained on crystal prepared from the Bridgman method - refined formula $Tl_{9.37(2)}La_{0.63}Te_6$ - were much better than those from the homogenous $x = 0.2$ sample. No suitable crystal was found from the homogenous $x = 1.0$ sample. The lattice parameters obtained from a very small crystal of the compound $x = 1$ ($a = 8.9220(4)$ Å, $c = 13.156(1)$ Å, $V = 1047.2(1)$ Å^3) indicate a much higher La content than $x = 0.63$ (with $a = 8.951(1)$ Å, $c = 12.894(1)$ Å, $V = 1033.1(2)$ Å^3). The crystallographic data are summarized in *Table 3.3*, and the atomic parameters including the occupancy factors are listed in *Table 3.4*.

Table 3.3: Crystallographic Data for $Tl_{10-x}La_xTe_6$, x = 0.28, 0.63

Refined formula	$Tl_{9.72(6)}La_{0.28}Te_6$	$Tl_{9.37(2)}La_{0.63}Te_6$
formula weight [g/mol]	2790.97	2768.06
T of measurement [K]	298(2)	298(2)
λ [Å]	0.71073	0.71073
space group	*I*4/*mcm*	*I*4/*mcm*
a [Å]	8.9538(3)	8.951(1)
c [Å]	12.6118(9)	12.894(1)
V [Å^3]	1011.09(9)	1033.1(2)
Z	2	2
μ [mm^{-1}]	86.17	82.33
ρ_{calcd} [g/cm^3]	9.167	8.899
$R(F_o)^a$ \ $R_w(F_o^2)^b$	0.059 \ 0.137	0.022 \ 0.053

^{a} $R(F_o) = \Sigma||F_o|-|F_c||/ \Sigma|F_o|$

^{b} $R_w(F_o^2) = [\ \Sigma[w(F_o^2 - F_c^2)^2]/ \Sigma[w(F_o^2)^2]\ ]^{/2}$

Table 3.4: Atomic coordinates and equivalent isotropic displacement parameters of $Tl_{9.37(2)}La_{0.63}Te_6$

Atom	**Site**	***x***	***y***	***z***	U_{eq}/Å^2
M1[a]	*4c*	0	0	0	0.0277(3)
Tl2	*16l*	0.14701(3)	x + ½	0.15960(3)	0.0372(2)
Te1	*4a*	0	0	¼	0.0283(3)
Te2	*8h*	0.33926(6)	x + ½	0	0.0206(2)

a) M1 is mixed occupied by 69(1)% Tl and 31(1)% La.

3.2 Analysis of $Tl_{10-x}Ln_xTe_6$, Ln = Ce, Pr, Nd, Sm, Gd, Tb, Dy, Ho and Er, $0.25 \leq x \leq 1.32$

3.2.1 EDX and DSC analysis

The elemental analysis data on different crystals for each compound analyzed by this technique confirmed the phase homogeneity except for Tl_9HoTe_6 and $Tl_{8.84}Gd_{1.16(8)}Te_6$; the Tl_9HoTe_6 compound had an unknown secondary phase highly rich in holmium (12.70% Tl, 68.27% Ho and 19.03% Te) while the $Tl_{8.84}Gd_{1.16(8)}Te_6$ compound had a slightly gadolinium rich phase (48.72% Tl, 14.68 % Gd and 36.61% Te). The atomic percents for each element at different spots for a particular sample were averaged and compared to the nominal atomic percent of the corresponding compound. *Table 3.5* shows the nominal and experimental elemental atomic percents of some compounds for the $Tl_{10-x}Ln_xTe_6$ phase, Ln = Ce, Pr, Nd, Sm, Gd, Tb, Dy, Ho and Er. Among the homogenous samples, $Tl_{9.32}Gd_{0.68}Te_6$ had 20% more gadolinium than expected; $Tl_{9.5}Dy_{0.5}Te_6$ and Tl_9DyTe_6 compounds had about 23% - 24% less dysprosium than expected. Based on the EDX data, no more than 4.7% of dysprosium and holmium could be incorporated in the structure. Two parameters of the substituent (charge and size) were considered to substitute Tl^{3+} at the *4c* site in the body centered tetragonal structure of the $Tl_{10}Te_6$ ($Tl_9^+Tl^{3+}Te_6$) to make $Tl^+_9Ln^{3+}Te_6$. The charge should be +3 to maintain charge neutrality and the size of the substituent should be between that of Tl^{3+} (1.025 Å)[106] and Bi^{3+} (1.172 Å)[106] to be able to fit at the *4c* site. Unlike the possible mixed valent elements like cerium (+3 and +4), samarium, europium and ytterbium (+2 and +3); dysprosium and holmium exhibit only a +3 oxidation state like lanthanum, neodymium, gadolinium and erbium,[92, 118, 119] hence, they were expected to be incorporated in the Tl_5Te_3 structure up to at least 6%, yielding Tl_9LnTe_6. Moreover, there is nothing in particular about the sizes of Dy^{3+} (1.052 Å)[106] and Ho^{3+} (1.041 Å)[106] compared to that of Er^{3+} (1.030 Å)[106] which could have avoided their incorporation in the structure and yet not that of Er^{3+}. Therefore, the reason why incorporation of dysprosium and holmium in the structure were limited to about 4% - 5% is not known, just like the reason why more neodymium (8.25%) compared to gadolinium (7.25%), terbium and erbium (6.1% - 6.2%) could incorporated into the structure is not apparent.

Table 3.5: EDX data of $Tl_{10-x}Ln_xTe_6$, Ln = Ce, Pr, Nd, Sm, Gd, Tb, Dy and Er, $0.5 \leq x \leq 1.3$

	Observed			Nominal		
	Tl	**Ln**	**Te**	**Tl**	**Ln**	**Te**
$\mathbf{Tl_{8.97}Ce_{1.03(5)}Te_6}$	58.3	5.9	35.8	56.1	6.4	37.5
$\mathbf{Pr_{8.92}Pr_{1.08(8)}Te_6}$	57.3	7.2	35.5	55.8	6.8	37.5
$\mathbf{Tl_{8.98}Nd_{1.02(6)}Te_6}$	59.5	5.8	34.7	56.1	6.4	37.5
$\mathbf{Tl_{8.68}Nd_{1.32(6)}Te_6}$	54.6	8.7	36.8	54.3	8.3	37.5
$\mathbf{Tl_{8.99}Sm_{1.01(7)}Te_6}$	59.6	6.3	33.9	56.7	6.3	37.5
$\mathbf{Tl_{9.32}Gd_{0.68(8)}Te_6}$	59.8	5.4	34.8	58.0	4.3	37.5
$\mathbf{Tl_{9.0}Gd_{1.0(1)}Te_6}$	59.8	5.6	34.7	56.5	6.0	37.5
$\mathbf{Tl_{8.83}Gd_{1.17(8)}Te_6}$	55.4	7.1	37.5	55.3	7.3	37.5
$\mathbf{Tl_{9.01}Tb_{0.99(5)}Te_6}$	59.1	6.3	34.7	56.3	6.2	37.5
$\mathbf{Tl_{9.5}Dy_{0.5}Te_6}$	62.3	2.6	35.1	59.4	3.1	37.5
$\mathbf{Tl_9DyTe_6}$	60.4	4.7	35.0	56.3	6.2	37.5
$\mathbf{Tl_9HoTe_6}$	59.8	3.9	36.4	56.3	6.2	37.5
$\mathbf{Tl_{9.47}Er_{0.53(6)}Te_6}$	61.5	3.2	35.3	59.1	3.4	37.5
$\mathbf{Tl_{9.19}Er_{0.81(6)}Te_6}$	58.2	5.5	36.4	57.4	5.1	37.5
$\mathbf{Tl_{9.05}Er_{0.95(5)}Te_6}$	59.0	6.0	35.0	56.4	6.1	37.5

DSC measurements were done for $Tl_{8.97}Ce_{1.03(5)}Te_6$, $Tl_{8.92}Pr_{1.08(8)}Te_6$, $Tl_{8.99}Sm_{1.07(7)}Te_6$, $Tl_{9.05}Er_{0.95(5)}Te_6$ and Tl_9HoTe_6 compounds. The DSC plots of the two late compounds of the Tl_9LnTe_6 series (Tl_9HoTe_6 and Tl_9ErTe_6, *Figure 3.5*) showed two endothermic peaks (during melting) and one exothermic (during crystallization). The peak at about ~ 720 K could be most probably due to the presence of traces of Tl_5Te_3, which could not be observed from the EDX. Unlike for the case of Tl_9ErTe_6, it is quite understandable for Tl_9HoTe_6 as the EDX data of the latter showed an inhomogeneity. $Tl_{8.98}Nd_{1.02(6)}Te_6$ has already been reported to melt congruently at 820 K,[120] similarly, the congruent melting point of Tl_9LaTe_6 is reported to be ~ 802 K.[117] Assuming that the peak around 720 K is due to Tl_5Te_3, melting points of Tl_9HoTe_6 and $Tl_{9.05}Er_{0.95(5)}Te_6$ are ~ 747 K and ~ 763 K respectively. In contrast, DSC measurements of $Tl_{8.97}Ce_{1.03(5)}Te_6$, $Tl_{8.92}Pr_{1.08(8)}Te_6$ and $Tl_{8.99}Sm_{1.07(7)}Te_6$ compounds show that there is only one endothermic (melting) peak during heating and one exothermic (crystallization) peak

during cooling, indicating no decomposition below 1050 K. The melting points of three compounds were quite close to each other, namely between 710 K and 717 K.

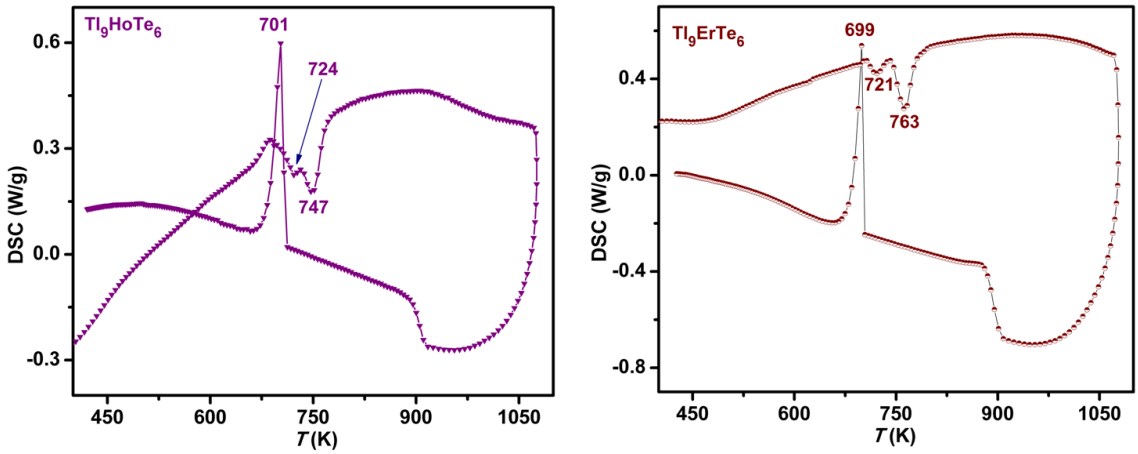

Figure 3.5: DSC plots of Tl_9HoTe_6 (right) and Tl_9ErTe_6 (left)

3.2.2 XRD analysis of Tl_9LnTe_6

The lattice parameters of some compounds were obtained by refining the XRD patterns using the GSAS software as discussed in *Section 2.2.3*. *Figure 3.6* shows the XRD patterns of the Tl_9LnTe_6 compounds with Ln being La, Nd, Gd, Tb, Dy, Ho and Er. The XRD pattern of Tl_9LaTe_6 compound matches closely to that of Tl_9BiTe_6 while that of Tl_9DyTe_6 matches to that of $Tl_{10}Te_6$, due to the decrease in c/a ratio from Tl_9LaTe_6 to Tl_9DyTe_6. It is also noteworthy that there is also a slight shift in the 2θ values of the patterns just like that observed for the phase range study (*Section 3.2*), however the noticeable shifts were for that of Tl_9HoTe_6 and Tl_9ErTe_6. The left shift in the XRD pattern of the Tl_9ErTe_6 compound is not justified based on Bragg's law as both the lattice parameters, *a* and *c* decrease in (*Table 3.7*) resulting in a decrease of the lattice spacing, *d*.

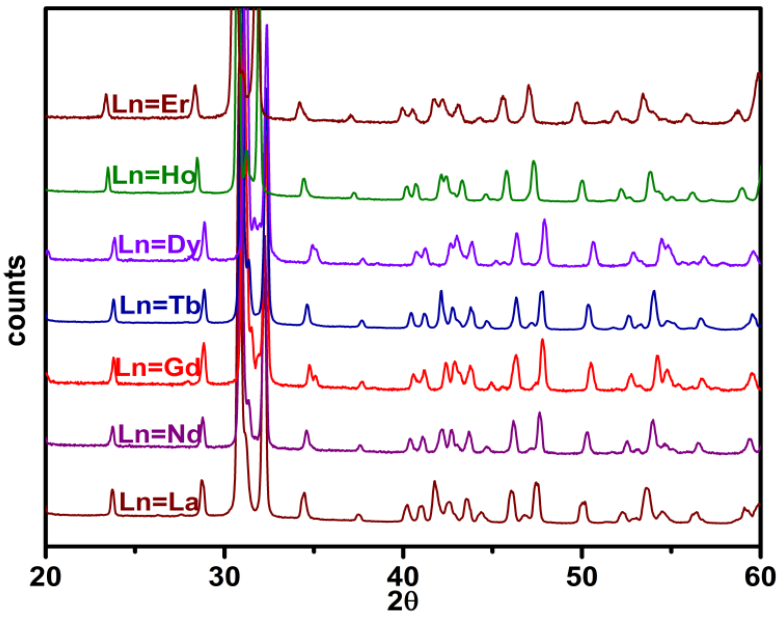

Figure 3.6: XRD patterns of Tl_9LnTe_6, Ln = La, Nd, Gd - Er

Unlike the XRD patterns shown in *Figure 3.6*, the XRD pattern of Tl_9CeTe_6 showed that the latter has a smaller *c/a* ratio (as it corresponds to that of $Tl_{10}Te_6$) while that of Tl_9SmTe_6 indicate a greater *c/a* ratio (as it corresponds to that of Tl_9BiTe_6) (*Figure 3.7*). Therefore, the *c/a* ratio of Tl_9CeTe_6 can be deduced to be quite small compared to that of Tl_9LaTe_6 and comparable to that of Tl_5Te_3. Furthermore, the *c/a* ratio increases from Tl_9CeTe_6 to Tl_9SmTe_6.

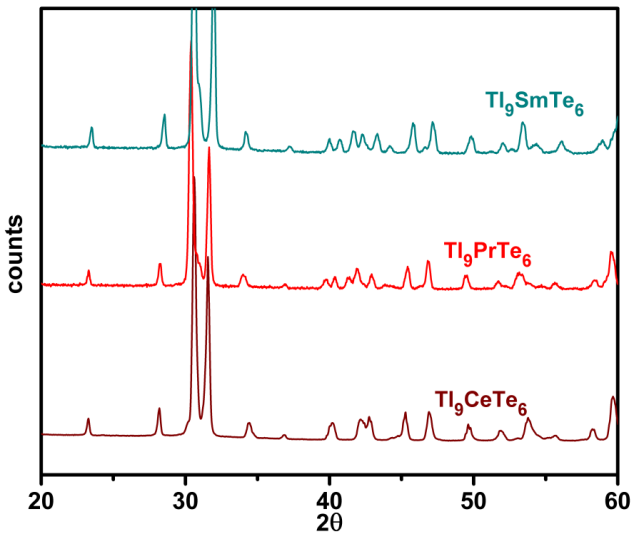

Figure 3.7: XRD patterns of Tl_9LnTe_6, Ln = Ce, Pr and Sm

3.2.3 Rietveld refinement of Tl_9LnTe_6

Nominal compounds Tl_9CeTe_6, Tl_9PrTe_6, Tl_9NdTe_6, Tl_9SmTe_6, Tl_9GdTe_6 Tl_9TbTe_6 and Tl_9ErTe_6 were refined to $Tl_{8.97}Ce_{1.03(5)}Te_6$, $Tl_{8.92}Pr_{1.08(8)}Te_6$, $Tl_{8.98}Nd_{1.02(6)}Te_6$, $Tl_{8.99}Sm_{1.07(7)}Te_6$, $Tl_{9.0}Gd_{1.0(1)}Te_6$, $Tl_{9.01}Tb_{0.99(5)}Te_6$ and $Tl_{9.05}Er_{0.95(5)}Te_6$, respectively using the Tl_9BiTe_6 model and confirming that the space group of *I4/mcm* was maintained. This implies that the reactions for those compounds were very successful and allows us to assume that the other reactions were as much successful and that the targeted compounds were obtained except for Tl_9DyTe_6 and Tl_9HoTe_6 compounds.

The absence of the lanthanoid atoms at the *16l* site was confirmed during the refinements as the occupancy of the latter remained 1 when it was set free. This implies that the mixed occupancy by Tl and Ln was only at the *4c* site as reported for Tl_5Te_3[69] (mixed occupancy between Tl^+ and Tl^{3+} at the *4c* site), Tl_9BiTe_6[66, 109] and the lanthanum series.[117] However, due to the close relations between the equivalent isotropic displacement parameter (U_{eq}) and the occupancy factor (F),[121] the U_{eq} parameter were fixed to the values obtained upon its refinement using the refined F values (obtained when refining each parameters individually). *Table 3.6* shows the atomic coordinates and U_{eq} for $Tl_{8.98}Nd_{1.02(6)}Te_6$ and $Tl_{9.05}Er_{0.95(5)}Te_6$ and *Tables 3.7 – 3.8* show the lattice parameters, unit cell volumes and selected interatomic distances of the Tl_9LnTe_6 compounds, Ln = Ce, Pr, Nd, Sm, Gd, Tb and Er.

Table 3.6: Atomic coordinates and equivalent isotropic displacement parameters of $Tl_{8.98}Nd_{1.02(6)}Te_6$ and $Tl_{9.05}Er_{0.95(5)}Te_6$

atom	Wyckoff site	$Tl_{9.98}Nd_{1.02(6)}Te_6$				$Tl_{9.05}Er_{0.95(5)}Te_6$			
		x	*y*	*z*	U_{eq}/Å^2	*x*	*y*	*z*	U_{eq}/Å^2
Nd/Tl1	***4c***	0	0	0	0.012	0	0	0	0.033
Tl2	***16l***	0.1471(2)	*x* + ½	0.1620(4)	0.034(2)	0.1475(2)	*x* + ½	0.1627(3)	0.041(1)
Te1	***4a***	0	0	¼	0.031(3)	0	0	¼	0.044(3)
Te2	***8h***	0.3380(5)	*x* + ½	0	0.029(3)	0.3380(5)	*x* + ½	0	0.048(3)

Table 3.7: Lattice parameters and selected interatomic distances of $Tl_{10-x}Ln_xTe_6$, Ln = Nd, Gd, Tb and Er, $x \approx 1$

		$Tl_{8.98}Nd_{1.02(6)}Te_6$	$Tl_{9.0}Gd_{1.0(1)}Te_6$	$Tl_{9.01}Tb_{0.99(5)}Te_6$	$Tl_{9.05}Er_{0.95(5)}Te_6$
***a* (Å)**		8.895(3)	8.894(6)	8.860(3)	8.853(3)
***c* (Å)**		12.998(5)	12.909(9)	12.993(5)	12.945(4)
***V* (Å^3)**		1028(1)	1021(2)	1020(1)	1014.6(9)
M1–Te1 (Å)	2×	3.249(1)	3.227(2)	3.248(1)	3.2363(9)
M1–Te2 (Å)	4×	3.334(3)	3.329(4)	3.315(2)	3.318(2)
Tl2–Te2 (Å)		3.193(5)	3.174(8)	3.169(4)	3.182(4)
Tl2–Te2 (Å)	2×	3.466(5)	3.469(9)	3.458(4)	3.458(4)
Tl2–Te1 (Å)	2×	3.588(2)	3.582(4)	3.581(2)	3.567(2)
Tl2–Tl2 (Å)		3.454(8)	3.709(9)	3.471(7)	3.694(5)
Tl2–Tl2 (Å)	2×	3.477(7)	3.47(1)	3.477(6)	3.455(5)
Tl2–Tl2 (Å)		3.702(5)	3.43(1)	3.675(5)	3.420(6)
R		0.0550	0.0699	0.0399	0.0588
wR		0.0609	0.0954	0.0503	0.0575
R_F^2		0.0973	0.0868	0.0876	0.1063

The lattice parameters of $Tl_{8.98}Nd_{1.02(6)}Te_6$ were found to be 8.895(3) Å for *a* and 12.998(5) Å for *c*. However, they did not match with those obtained by indexing the powder XRD patterns of Tl_9NdTe_6 (*a* = 8.855 Å and *c* = 13.010 Å) in the Tl_5Te_3 structure.[122]

The change in lattice parameters across the series Tl_9LnTe_6 shown in *Tables 3.7* and *Figure 3.8*, were anisotropic like in the case of Tl_9BiTe_6 (*a* = 8.855(2) Å, *c* = 13.048(4) Å)[66, 109] with respect to Tl_5Te_3 (*a* = 8.930(2) Å, *c* = 12.589(4) Å)[69] and (*a* = 8.929 Å and *c* = 12.607 Å).[107] $Tl_{9.0}Gd_{1.0(1)}Te_6$ and $Tl_{9.05}Er_{0.95(5)}Te_6$ had lattice parameters *a* = 8.894(6) Å and 8.853(3) Å, *c* = 12.909(9) Å and 12.945(4) Å respectively. The reason for this is again the increasing regularities in the $(M1)Te_6$ octahedra due to the

spherical shape of the f-block elements.[117] As a result of this, the expected decreasing trend in the M1–Te1 and M1–Te2 bond lengths across the Tl_9LnTe_6 series due to the decrease in atomic size of the lanthanoids across the series was not smooth. M1–Te1 bond length decreased from 3.249(1) Å in $Tl_{8.98}Nd_{1.02(6)}Te_6$ to 3.227(2) Å in $Tl_{9.0}Gd_{1.0(1)}Te_6$ and increased to 3.248(1) Å in $Tl_{9.01}Tb_{0.99(5)}Te_6$ while the M1–Te2 bond length decreased from 3.334(3) Å in $Tl_{8.98}Nd_{1.02(6)}Te_6$ to 3.315(2) Å in $Tl_{9.01}Tb_{0.99(5)}Te_6$ but increased slightly to 3.318(2) Å in $Tl_{9.05}Er_{0.95(5)}Te_6$.

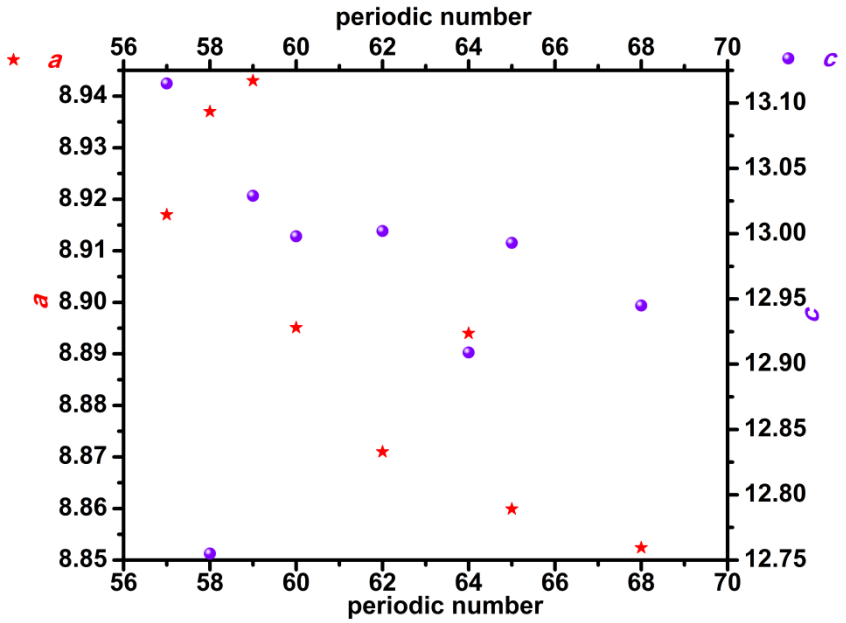

Figure 3.8: Plots of lattice parameters, *a* (Å) and *c* (Å) vs. periodic number for $Tl_{10-x}Ln_xTe_6$, $x \approx 1$

Nevertheless, when moving across the series from $Tl_{8.98}Nd_{1.02(6)}Te_6$ to $Tl_{9.05}Er_{0.95(5)}Te_6$, the expected decrease in overall volume was observed, from 1028(1) $Å^3$ to 1014.6(9) $Å^3$ respectively. This decrease was also observed for $x \approx 0.5$ and 0.75 in $Tl_{10-x}Ln_xTe_6$ (*Figure 3.9*). Similar observations were made for the $TlLnTe_2$ systems.[123]

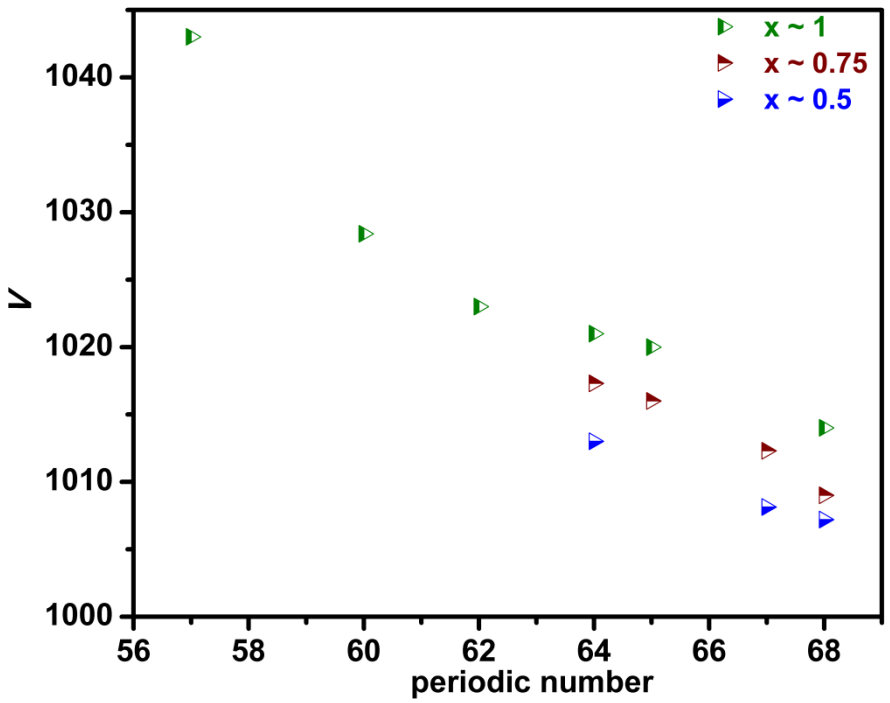

Figure 3.9: Plot of *V* (Å^3) vs. periodic number for $Tl_{10-x}Ln_xTe_6$, *x* = 0.5. 0.75 and 1

However, $Tl_{8.97}Ce_{1.03(5)}Te_6$ had an unexpectedly smaller volume (1019(1) Å^3) due to possible presence of mixed valent (Ce^{3+}/Ce^{4+}) ions in the system. Due to the smaller size of Ce^{4+} (1.01 Å)[106] with respect to that of Ce^{3+} (1.283 Å),[106] the presence of the latter will result in smaller unit cell volume. Mixed valent cerium compounds are quite common, some examples are $CeSn_3$, Ce_2Sn_5, $CeSn_7$.[124] Ternary compounds like $CeNi_5Sn$,[125] $CeFe_4Sb_{12}$[126] and $Ce_3Pt_3Sb_4$[127] were reported to be mixed valent as well. $Tl_{8.92}Pr_{1.08(8)}Te_6$ has a greater unit cell volume (1042(2) Å^3) with respect to that of the Tl_9LaTe_6 series (1047.2(1) Å^3)[117] and $Tl_{9.05}Er_{0.95(5)}Te_6$ (1014.6(9) Å^3) (*Figure 3.10*). Unlike the cerium compound, the praseodymium compound can not have mixed valent ions, as if this were the case, the unit cell volume would have been smaller, like that of the cerium compound, due to smaller size of Pr^{4+} (0.99 Å)[106] with respect to that of Pr^{3+} (1.13 Å).[106] Hence, the most plausible explanation for this observation is the presence of more praseodymium in the structure. In the worst case scenario with the maximum margin of error of 3σ, the formula of the compound would be $Tl_{8.68}Pr_{1.32}Te_6$ which should have bigger unit cell volume than Tl_9PrTe_6. EDX data which indicated more than 6.25% of Pr is incorporated in the system supports this scenario.

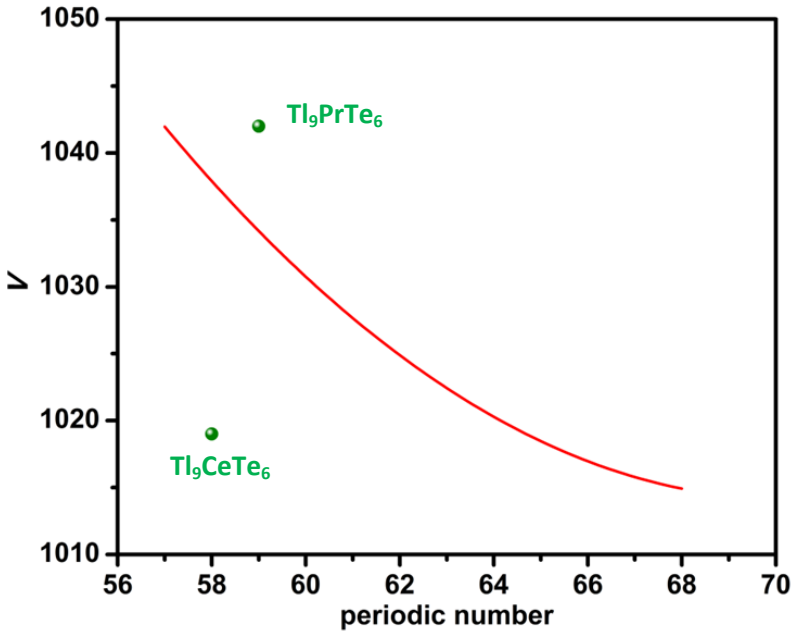

Figure 3.10: Unit cell volume of Tl_9CeTe_6 and Tl_9PrTe_6 with respect to the general trend (red curve) of *V* ($Å^3$) vs. periodic number for $Tl_{10-x}Ln_xTe_6$

Table 3.8 shows that the *c*/*a* ratio did indeed increase from Tl_9CeTe_6 to Tl_9SmTe_6 as indicated by the XRD patterns. Both of the lattice parameters, *a* and *c*, increase from 8.937 Å and 12.755 Å respectively for $Tl_{8.97}Ce_{1.03(5)}Te_6$ to 8.943 Å and 13.029 Å for $Tl_{8.92}Pr_{1.08(8)}Te_6$ and then decrease to 8.871 Å and 13.002 Å for $Tl_{8.99}Sm_{1.07(7)}Te_6$. Therefore, the change in lattice parameters is not anisotropic like in the case of Tl_9BiTe_6[66, 109] with respect to $Tl_{10}Te_6$.[69, 107] As a result, the general observation for the interatomic distances in the structures is that they increase from the $Tl_{8.97}Ce_{1.03(5)}Te_6$ structure to that of $Tl_{8.92}Pr_{1.08(8)}Te_6$ except for the M1–Te2 (4×) and Tl2–Tl2 (1×) distances; comparing the data for the latter and with that of $Tl_{8.99}Sm_{1.07(7)}Te_6$, there is a smooth decrease in the interatomic distances. Increasing regularities in the $(M1)Te_6$ octahedron results in the anisotropic change in the lattice parameters, the $SmTe_6$ octahedra are more regular compared to $CeTe_6$ and $PrTe_6$, and yet the change in lattice parameters is not anisotropic.

Table 3.8: Lattice parameters and selected interatomic distances of $Tl_{8.97}Ce_{1.03(5)}Te_6$, $Tl_{8.92}Pr_{1.08(8)}Te_6$ and $Tl_{8.99}Sm_{1.01(7)}Te_6$

		$Tl_{8.97}Ce_{1.03(5)}Te_6$	$Tl_{8.92}Pr_{1.08(8)}Te_6$	$Tl_{8.99}Sm_{1.01(7)}Te_6$
***a* (Å)**		8.937(3)	8.943(5)	8.871(4)
***c* (Å)**		12.755(4)	13.029(7)	13.002(6)
***V* (Å^3)**		1019(1)	1042(2)	1023(1)
M1–Te1 (Å)	2×	3.189(1)	3.257(2)	3.250(1)
M1–Te2 (Å)	4×	3.359(3)	3.350(3)	3.321(3)
Tl2–Te2 (Å)		3.182(5)	3.192(5)	3.172(5)
Tl2–Te2 (Å)	2×	3.439(5)	3.467(6)	3.461(5)
Tl2–Te1 (Å)	2×	3.594(2)	3.616(3)	3.582(3)
Tl2–Tl2 (Å)		3.748(5)	3.708(6)	3.696(6)
Tl2–Tl2 (Å)		3.424(7)	3.51(1)	3.488(7)
Tl2–Tl2 (Å)	2×	3.484(7)	3.513(8)	3.461(9)
R		0.0490	0.0716	0.0528
wR		0.0553	0.0673	0.0601
R_F^2		0.1174	0.1075	0.1178

3.2.4 Lattice parameters of $Tl_{10-x}Ln_xTe_6$ as *x* increases

A similar anisotropic change in lattice parameters was observed within a particular phase for a given Ln as *x* increases, as shown in *Tables 3.9* and *3.10* for the gadolinium and erbium phases respectively. *Figure 3.11* shows the change in lattice parameters for $Tl_{9.52}Ho_{0.48(4)}Te_6$ and $Tl_{9.24}Ho_{0.76(8)}Te_6$ of the holmium series and $Tl_{8.98}Nd_{1.02(6)}Te_6$ and $Tl_{8.68}Nd_{1.32(6)}Te_6$ of the neodymium series. For the holmium phase, as *x* increases, the lattice parameter *a* decreases while the *c* increases; and the opposite is true for the neodymium phase, as *x* increases, *a* increases while *c* decreases.

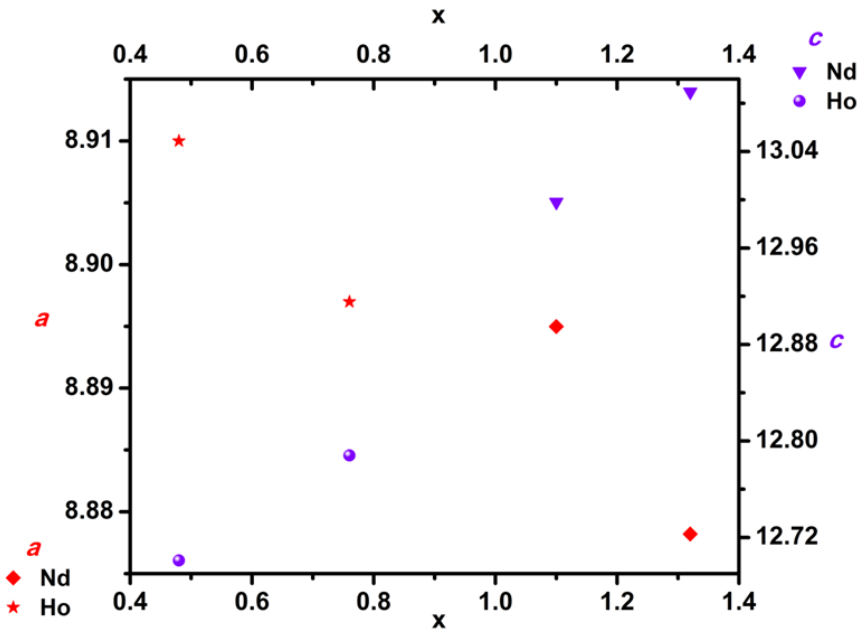

Figure 3.11: Plots of lattice parameters of $Tl_{10-x}Ln_xTe_6$, x ~ 1.02 and 1.32 for Ln = Nd; x ~ 0.48 and 0.76 for Ho

However, irrespective to the lanthanoid element, the unit cell volume increases as x increases in the $Tl_{10-x}Ln_xTe_6$ phase study. As x increases within a particular phase, more of the f-block atom replaces the d-block thallium ion. As a result, the unit cell volume is expected to increase as more lanthanoid ion is incorporated in the structure. The unit cell volumes of the two early and two late compounds of the holmium phase ($Tl_{9.52}Ho_{0.48(4)}Te_6$ and $Tl_{9.24}Ho_{0.76(8)}Te_6$) and neodymium phase ($Tl_{8.98}Nd_{1.02(6)}Te_6$ and $Tl_{8.68}Nd_{1.32(6)}Te_6$) respectively tend to give the same trend supporting the hypothesis (*Figure 3.12*). Similar observation was obtained for the lanthanum series[117] based on the single crystal X-ray diffraction data, as the lanthanum content increases, the unit cell volume increases (from 1011.09(9) $Å^3$ for $Tl_{9.72(6)}La_{0.28}Te_6$ to 1047.2(1) $Å^3$ for $Tl_{8.96(3)}La_{1.04}Te_6$) as the p-block thallium atom at the *4c* site is replaced by bigger f-block atom.

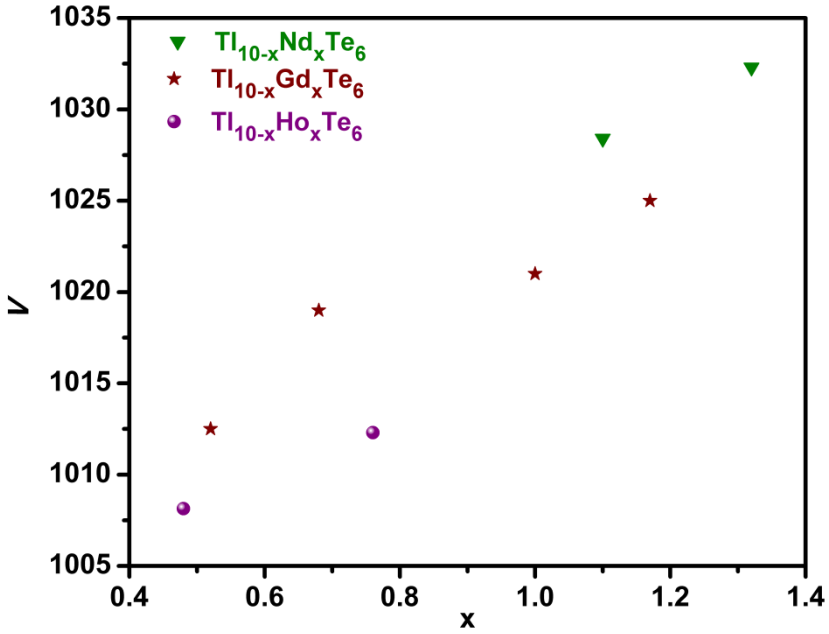

Figure 3.12: Plots of unit cell volume, *V* (Å^3) vs. *x* for $Tl_{10-x}Ln_xTe_6$, Ln = Nd, Gd and Ho (right)

Table 3.9: Lattice parameters and selected interatomic distances of $Tl_{10-x}Gd_xTe_6$, $0.52 \leq x \leq 1.16$

		$Tl_{9.48}Gd_{0.52(5)}Te_6$	$Tl_{9.32}Gd_{0.68(8)}Te_6$	$Tl_{9.04}Gd_{1.0(1)}Te_6$	$Tl_{8.83}Gd_{1.17(5)}Te_6$
***a* (Å)**		8.913(3)	8.874(5)	8.894(6)	8.859(1)
***c* (Å)**		12.746(4)	12.948(7)	12.909(9)	13.056(3)
***V* (Å^3)**		1012.5(9)	1019(2)	1021(2)	1025(1)
M1–Te1 (Å)	2×	3.1866(6)	3.237(2)	3.227(2)	3.264(1)
M1–Te2 (Å)	4×	3.343(2)	3.326(3)	3.329(4)	3.322(2)
Tl2–Te2 (Å)		3.160(5)	3.171(6)	3.174(8)	3.198(5)
Tl2–Te2 (Å)	2×	3.431(4)	3.443(6)	3.469(9)	3.468(4)
Tl2–Te1 (Å)	2×	3.593(2)	3.586(3)	3.582(4)	3.572(2)
Tl2–Tl2 (Å)		3.714(5)	3.691(6)	3.709(9)	3.695(5)
Tl2–Tl2 (Å)	2×	3.481(6)	3.47(1)	3.47(1)	3.468(6)
Tl2–Tl2 (Å)		3.452(7)	3.492(9)	3.43(1)	3.435(7)
R		0.0455	0.0616	0.0699	0.0486
wR		0.0550	0.0670	0.0954	0.0515
R_F^2		0.12560	0.0756	0.08683	0.10855

Table 3.10: Lattice parameters and selected interatomic distances of $Tl_{10-x}Er_xTe_6$, $0.53 \leq x \leq 0.95$

		$Tl_{9.47}Er_{0.53(6)}Te_6$	$Tl_{9.19}Er_{0.81(6)}Te_6$	$Tl_{9.05}Er_{0.95(5)}Te_6$
***a* (Å)**		8.905(3)	8.859(3)	8.853(3)
***c* (Å)**		12.703(4)	12.860(5)	12.945(4)
***V* (Å^3)**		1007.2(9)	1009(1)	1014.6(9)
M1–Te1 (Å)	2×	3.176(1)	3.215 (1)	3.2363(9)
M1–Te2 (Å)	4×	3.344(2)	3.323(2)	3.318(2)
Tl2–Te2 (Å)		3.163(4)	3.167(4)	3.182(4)
Tl2–Te2 (Å)	2×	3.416(5)	3.444(4)	3.458(4)
Tl2–Te1 (Å)	2×	3.590(2)	3.568(2)	3.567(2)
Tl2–Tl2 (Å)		3.708(5)	3.708(5)	3.694(5)
Tl2–Tl2 (Å)	2×	3.474(6)	3.468(6)	3.455(5)
Tl2–Tl2 (Å)		3.449(7)	3.418(7)	3.420(6)
R		0.0662	0.0593	0.0588
wR		0.0604	0.0547	0.0575
R_F^2		0.1249	0.0791	0.1063

3.3 Electronic structure calculations of $Tl_{10-x}La_xTe_6$, x = 0.5, 1 and 1.25 using the LMTO method

The electronic structures of three different models were calculated utilizing the LMTO (linear muffin tin orbitals) method with the atomic spheres approximation (ASA)[99, 128] and the local density approximation (LDA) to treat exchange and correlation effects as mentioned in *Section 2.4*.[103] The chosen formulas were $Tl_{9.5}La_{0.5}Te_6$, Tl_9LaTe_6, and $Tl_{8.75}La_{1.25}Te_6$, for which a reduction of symmetry to *P*4/*m* (thus a doubled primitive cell), *I*4/*m* (original cell size) and $P\bar{1}$ (in a fourfold primitive cell), respectively, was required. The following wavefunctions were used: for Tl *6s*, *6p*, *6d* and *5f* (the latter downfolded);[129] for La *6s*, *6p* (downfolded), *5d* and *4f*, and for Te *5s*, *5p*, and *5d* and *4f*

(the latter two downfolded). The eigenvalue problems were solved on the basis of 126, 242 and 52 *k* points within the irreproducible wedge of the first Brillouin zone, respectively, selected with an improved tetrahedron method.[130]

3.3.1 Electronic structures of $Tl_{10-x}La_xTe_6$ as *x* increases

As no Te–Te bonds are present in the structure of $Tl_{10-x}La_xTe_6$, the twelve negative charges of the six Te atoms per formula unit may be balanced by the positive ones in case of $x = 1$, namely $(Tl^+)_9La^{3+}(Te^{2-})_6$. The band structure calculations confirm that the Fermi level falls into the band gap in the case of Tl_9LaTe_6, while the valence band is partly empty in the case of $Tl_{9.5}La_{0.5}Te_6$, and the conduction band partly filled in the case of $Tl_{8.75}La_{1.25}Te_6$ (*Figure 3.13*). Thus, increasing *x* in $Tl_{10-x}La_xTe_6$ is expected to change the properties from metallic ($x = 0$) to *p*-doped semiconducting ($x < 1$) to *n*-doped semiconducting ($x > 1$).

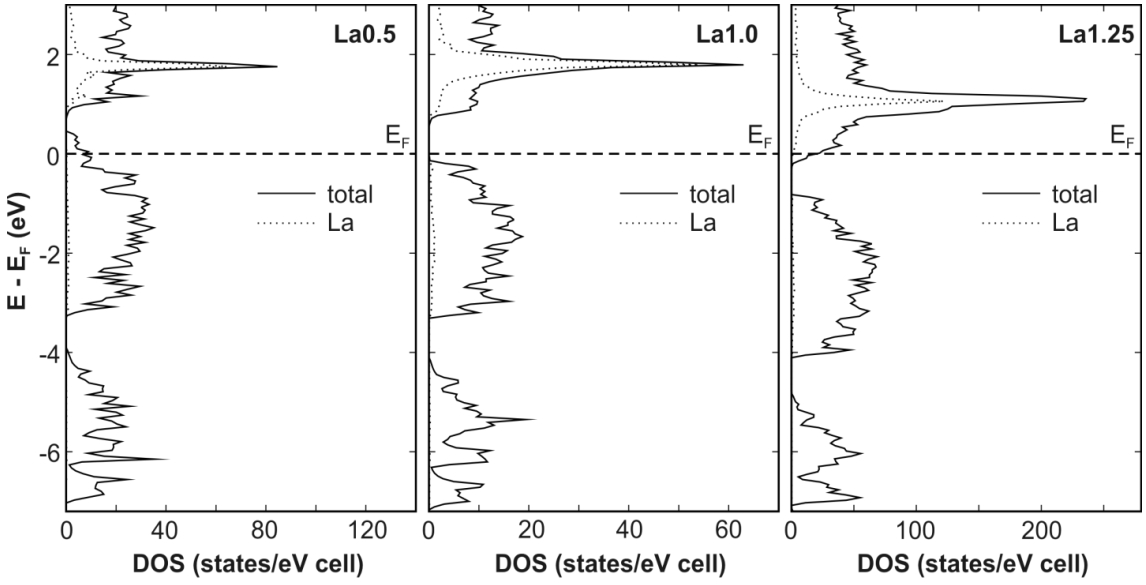

Figure 3.13: Densities of states of $Tl_{10-x}La_xTe_6$. Left: $x = 0.5$; center: $x = 1$; right: $x = 1.25$

The La content also has an impact onto the shape of the valence and conduction bands, as well as on the band gap size. The latter remains between 0.2 eV and 0.4 eV, which corresponds to the ideal gap size for the thermoelectric energy conversion.[131] The impact of La is largest on the conduction band, for its bottom area is dominated by the La *d* orbitals.

3.4 Electronic structures of Tl_9LnTe_6 with WIEN2*k* package

In the LDA (local density approximation) method, the onsite coulomb interaction (Hubbard parameter, *U*) is assumed to be small compared to the bandwidth, *W*.[132] This method was used for the electronic calculation of Tl_9LaTe_6 due to the absence of f-electron interactions (La: [Xe] $5d^1$ $6s^2$).[97] However, across the lanthanoid series, as the f-electrons are incorporated (eg. Tl_9GdTe_6, Gd: [Xe] $4f^7$ $5d^1$ $6s^2$ and Tl_9ErTe_6, Er: [Xe] $4f^{12}$ $6s^2$),[97] the system gets strongly correlated, thus, the LDA method does not work anymore.[132] For strongly correlated d- or f-electrons systems, the exchange correlation cannot be neglected. Hence, the electronic structures for such materials are calculated by the LSDA + *U* method which takes into account the onsite Coulomb interaction (*U*) and exchange parameter (*J*).[132-134] The electronic structure of Tl_9LnTe_6, Ln = La, Gd and Er were computed by the WIEN2*k* package. *U* and *J* values used for the calculations in this study are same as those derived in 1995[135] and used for Gd_3NiSi_2,[136] $Er_2@C_{82}$,[137] and ErSiO[138] systems, ~ 6.67 eV and ~ 0.72 eV respectively. The symmetry of the compounds Tl_9LnTe_6, Ln = La, Gd and Er was reduced to *I*4/*m* for these calculations just like for the DOS calculation of Tl_9LaTe_6 using LMTO method.[117] An irreducible Brillouin zone with 300 *k* points, RMT (muffin-tin radii) of 2.5, density plane cut-off of 7.0 and convergence criterium of 0.001 eV were used for all the calculations.

3.4.1 Electronic structures of Tl_9LnTe_6, Ln = La, Gd and Er, across the series

A DOS plot of Tl_9LaTe_6 was calculated by the WIEN2*k* package to compare it with that reported previously using the LMTO method[117] and understand the difference between DOS plots of compounds with f-electrons (Tl_9GdTe_6 and Tl_9ErTe_6) using the LSDA + *U* method. The DOS plots of Tl_9LaTe_6 calculated by LMTO and WIEN2*k*

package revealed not much difference, the band gap of the compound from both calculations is found to be ~ 0.5 eV (*Figure 3.14*).

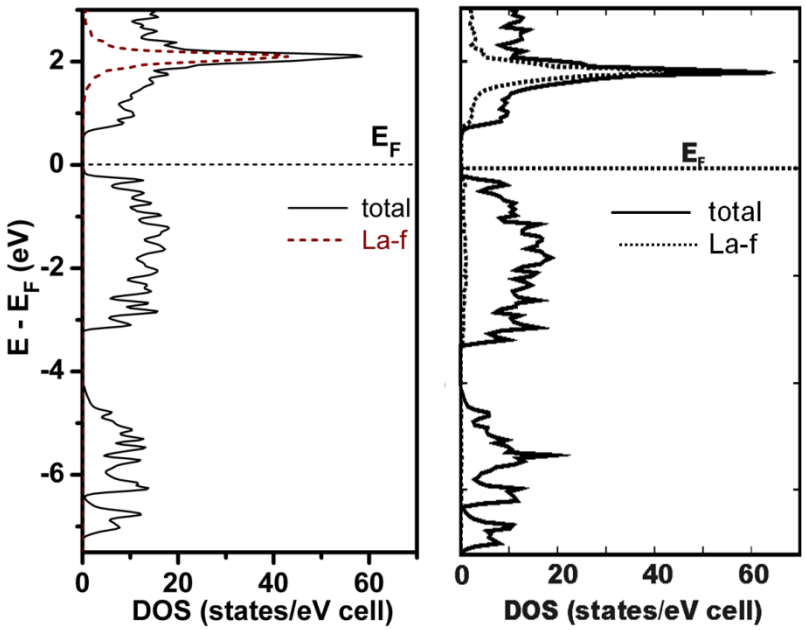

Figure 3.14: DOS of Tl_9LaTe_6 calculated with WIEN2*k* package (right) and LMTO (left)

With respect to that of Tl_9LaTe_6, Tl_9GdTe_6 has a much smaller band gap (< 0.3 eV). The fully occupied spin up f states are found well below the E_F (~ 5 eV) while the completely unoccupied f holes are found above the E_F (~ 0.25 eV) (*Figure 3.15*). Similar observation was made for Gd_3NiSi_2, however, the spin up f states were 8 eV below the E_F while the unoccupied f states were found at 6 eV above the E_F.[136]

Across any period of the periodic table, atomic size decreases from left to right, and so do the covalent radii and bond lengths.[97] This hypothesis supports the data for the lattice parameters and unit cell volume obtained from the refinements. As a result, across the series, the orbitals may overlap better leading to wider bandwidth comparing the DOS plots of Tl_9LaTe_6 with that of Tl_9ErTe_6 compounds. As a consequence band gap decreases as observed from the DOS calculations of Tl_9LaTe_6 and Tl_9GdTe_6. Moreover, for the lanthanoids, as more protons are added to the nucleus, the 4f-orbitals are stabilized and get lower than the 5d-orbitals.[92, 139] Hence, across the series, f-orbitals

contribution to valence band increases and when the f-band is situated in the valence band, the compound turns out to be a degenerate semiconductor which exhibits metal like character. Tl_9ErTe_6 is such a compound as per its calculated DOS plot where the 4f-states are part of the valence band (*Figure 3.15*). A similar observation was made for the ErSiO system.[138]

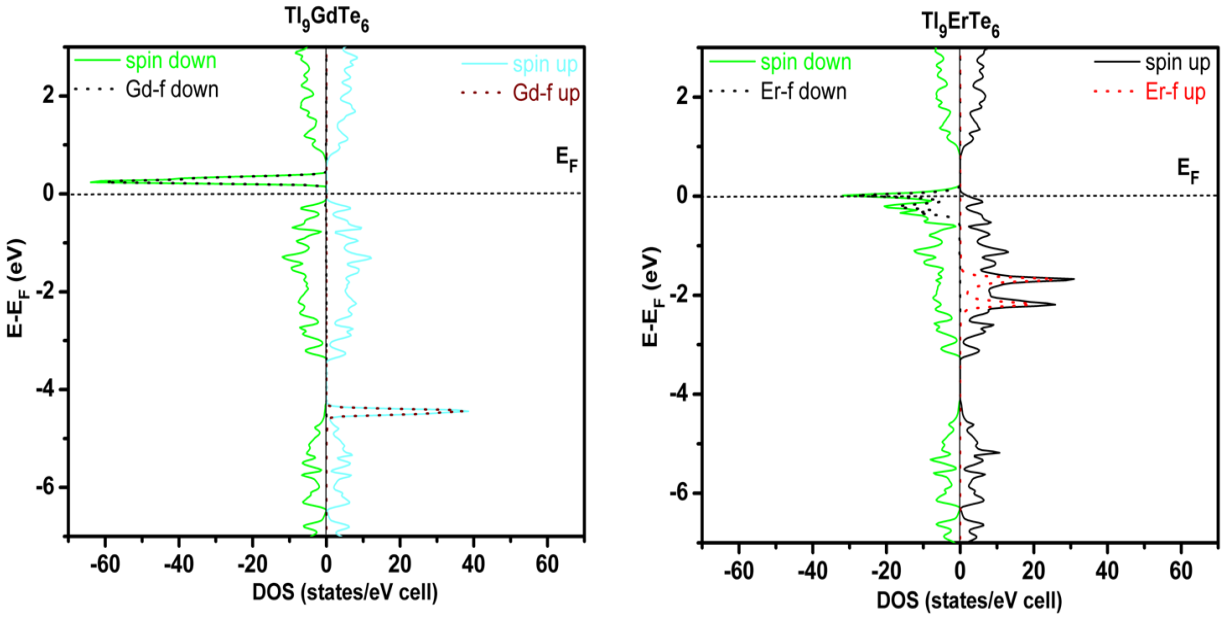

Figure 3.15: Dos of Tl_9GdTe_6 (left) and Tl_9ErTe_6 (right)

3.5 Conclusion

The $Tl_{10-x}Ln_xTe_6$ (Ln = La, Ce, Pr, Nd, Sm, Gd, Tb, Dy, Ho and Er) phase range was studied; Dy and Ho had a smaller range ($x < 1$) compared to La ($0.25 \leq x \leq 1.15$), Ce ($0.25 \leq x \leq 1.12$), Pr ($0.25 \leq x \leq 1.08$), Nd ($0.25 \leq x \leq 1.32$), Sm ($0.25 \leq x \leq 1.01$), Gd ($0.25 \leq x \leq 1.16$), Tb ($0.25 \leq x \leq 0.95$) and Er ($0.25 \leq x \leq 0.95$). From the single crystal data, as x increases for the lanthanum phase range, the unit cell volume, V, increases, V of $Tl_{9.72(6)}La_{0.28}Te_6$ is 1011.09(9) $Å^3$ and that of $Tl_{9.37(2)}La_{0.63}Te_6$ is 1033.1(2) $Å^3$. A similar observation was made from the Rietveld refinements using the Tl_9BiTe_6 model. For example, for the gadolinium phase, V of $Tl_{9.32}Gd_{0.68(8)}Te_6$ is 1019(2) $Å^3$ and that of $Tl_{8.84}Gd_{1.17(5)}Te_6$ is 1025(1) $Å^3$. Moreover, the Rietveld refinement data revealed that V decreases across the lanthanoid series for a particular stoichiometry ($Tl_{9.98}Nd_{1.02(6)}Te_6$, V

= 1028(1) Å and $Tl_{9.05}Er_{0.95(5)}Te_6$, V = 1014.6(9) Å). However, $Tl_{8.97}Ce_{1.03(6)}Te_6$ exhibited exceptionally smaller unit cell volume most probably due to presence of a mixed valent ion in the compound. On the contrary, $Tl_{8.92}Pr_{1.08(8)}Te_6$ had a much bigger unit cell volume than expected most probably due to presence of more than 6.25% praseodymium in the structure.

Electronic structure calculations indicate that perfectly ordered Tl_9LaTe_6 would be an intrinsic semiconductor, with a computed band gap of 0.4 eV. Moreover, as x increases in $Tl_{10-x}La_xTe_6$, the compound changes from metallic ($Tl_{9.5}La_{0.5}Te_6$) to intrinsic semiconductor (Tl_9LaTe_6) to *n*-type semiconductor ($Tl_{8.75}La_{1.25}Te_6$). The DOS calculated using the LDA and LSDA + U method for the compounds with f-electrons indicated a decrease in band gap across the series Tl_9LnTe_6, E_g of Tl_9GdTe_6 is much smaller than 0.4 eV. The Tl_9LnTe_6 compounds at the end of the series are expected to exhibit metallic like character. This is due to the stabilization of the f-states on taking f-electrons, hence, their f-states are at much lower energy and can possibly contribute to the valence band like in the case of Tl_9ErTe_6. Tl_9CeTe_6 could possibly exhibit the same scenario due to presence of stabilized Ce^{4+} f-states.

Therefore, it can be concluded that this study provides experimental data about crystal structures and lattice parameters of the thallium lanthanoid thellurides which agree with the theoretical trend expected. However, Tl_9CeTe_6 and Tl_9PrTe_6 were two exceptions. The electronic calculations support the hypothesis about the conducting property of Tl_9LnTe_6 across the Ln series and $Tl_{10-x}Ln_xTe_6$ for a particular phase.

4 THERMOELECTRIC PROPERTIES OF $Tl_{10-x}Ln_xTe_6$, Ln = La, Ce, Pr, Nd, Sm, Gd, Tb, Dy, Ho, Er, $0.25 \leq x \leq 1.32$

Thermoelectric properties of all the compounds synthesized were measured after they were analysed and concluded to be pure. The measurements were conducted as discussed in *Sections 2.3.1* and *2.3.2*. The properties are discussed in three parts as follows:

- Thermoelectric properties of $Tl_{10-x}La_xTe_6$, $0.25 \leq x \leq 1.15$
- Thermoelectric properties of $Tl_{10-x}Ln_xTe_6$, Ln = Nd, Ce, Pr, Sm, Gd, Tb, Dy, Ho and Er, $0.25 \leq x \leq 1.32$
- Anomalous properties of Tl_9LnTe_6, Ln = Ce, Pr and Sm

4.1 Thermoelectric properties of $Tl_{10-x}La_xTe_6$, $0.25 \leq x \leq 1.15$

The lanthanum phase is the first phase studied in this thallium lanthanoid telluride series. Due to an absence of f-electrons in this system, it is easier to understand the properties of this phase. Therefore, the lanthanum phase is considered to be the reference point for all the other series. The thermoelectric properties of this series were first studied on cold pressed sintered pellets; the thermoelectric properties of the compound with the best *ZT* value were studied on a hot pressed pellet.

4.1.1 Thermoelectric properties on cold-pressed sintered pellets

The electrical conductivity, σ, decreases with increasing La content (*Figure 4.1*) as expected based on the band structure calculations that predict a decrease of the charge carrier concentration (*Figure 3.13*). The $Tl_{10-x}La_xTe_6$ sample with $x = 0.5$ exhibits a room temperature σ value of 1480/(Ωcm), compared to 125/(Ωcm) for $x = 1.15$. The high charge carrier concentration of the $x = 0.5$ sample leads to a smoothly decreasing σ with increasing *T*, while all the other samples exhibit a decreasing σ at first, which then increases at higher temperatures. For example, σ of Tl_9LaTe_6 decreases from 290/(Ωcm) at 300 K to 130/(Ωcm) at 510 K, and then increases to 150/(Ωcm) at 600 K. This

indicates an increase in charge carrier concentration, *n*, that outweighs the decrease in mobility, μ, caused by significant amounts of intrinsic charge carriers crossing the forbidden energy gap above that temperature.[117] The room temperature values are comparable with those of zone-refined Tl_9BiTe_6 (180/(Ωcm))[140] and hot-pressed Tl_9BiTe_6 (250/(Ωcm)).[141]

The Seebeck coefficient, *S*, of degenerate semiconductors is proportional to *T* and approximately inversely proportional to the *n* ($S \propto n^{-2/3}$) according to *Equation 1.7*. According to the results of the electrical conductivity measurements, *S* should increase with increasing La concentration as well as with increasing *T*, until the charge carrier concentration increase begins to dominate. Both are observed experimentally (*Figure 4.1*, right) as *S*(300 K) increases from +28 μV/K for 0.5 La to +110 μV/K for 1.15 La. *S* generally exhibits a positive temperature dependence, but begins to decrease at higher La concentration around 500 K. The positive sign of the Seebeck coefficient is indicative of predominantly hole conduction, as expected because of the electron deficiency when $x < 1$, and that the conduction is still *p*-type for $x = 1.15$. This could be due to defects in the structure or strong anisotropies in the conduction band.[117] In any case, the Seebeck values published for Tl_9BiTe_6 are also positive, and with *S*(300 K) = +250 μV/K for the zone-refined[140] and +150 μV/K for the hot-pressed specimen[141] significantly higher than the La samples.

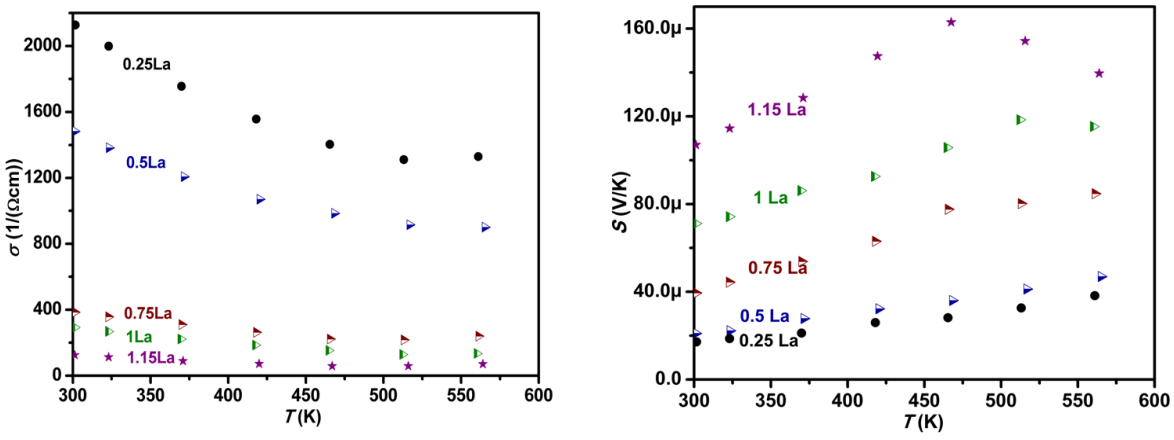

Figure 4.1: Plots of σ vs. *T* (right) and *S* vs. *T* (left) for $Tl_{10-x}La_xTe_6$

The total thermal conductivity, κ, as discussed in *Section 1.2.1.3*, consists of the electronic and the lattice contribution. In case where the κ_l contribution is quite small, κ will be a reflection of κ_e. In cases where κ_l does contribute significantly to κ, the trend of κ would be a combination of the two or reflect the one which is more dominant. κ_l might either decrease with T due to an increase in lattice vibration resulting in a decrease in mean free path, l_t as per *Equation 1.16* or increase with T due to increase in specific heat capacity, C_p, in cases where the plateau of the C_p vs. T plot (*Figure 1.6*) is not reached for the temperature range used.[30] On the other hand, κ_e will be a reflection of σ as per *Equation 1.15*. Therefore, since σ initially decreases with increasing T and start increasing above ~ 500 K, κ_e should also decrease with increasing T and increase above ~ 500 K. The plot of κ vs. T (*Figure 4.2*, left) reflects this scenario, hence it is concluded that the phonon contribution to conduct heat in this system is very small and the main mechanism responsible for heat conduction is the movement of the carriers. Moreover, the samples with the larger electrical conductivity exhibit larger κ as expected according to the Wiedemann-Franz law, *Equation 1.15*. κ did not change significantly with increasing T with respect to the change with increasing La concentration. Therefore, κ is basically temperature independent for the $Tl_{10-x}La_xTe_6$ samples, while it decreases like σ with increasing La concentration. Values around 0.5 W/(mK) were obtained for x = 1 and x = 1.15, which are slightly higher than those determined for zone-refined and hot-pressed Tl_9BiTe_6 (both around 0.39 W/(mK)). This suggests that the higher mass of Bi, compared to La, leads to lower κ_l, despite the larger mass fluctuation in the case of Tl_9LaTe_6.

The ZT values, derived from the measurements of S, σ, and κ, follow the typical trend of thermoelectric materials, which is an approximately linear increase until $(ZT)_{max}$ is reached. This occurs around 530 K with ZT = 0.18 for $Tl_{8.85}La_{1.15}Te_6$ (*Figure 4.2*, right). On the other hand, the other La-containing materials show an increase throughout the whole measurement range, while their ZT values remain lower, with the exception of Tl_9LaTe_6. Overall, the formally electron-precise material Tl_9LaTe_6 performs best, reaching ZT = 0.21 around 580 K. For comparison, hot-pressed Tl_9BiTe_6 was reported to exhibit $(ZT)_{max}$ at 590 K, with ZT = 0.86. Its significantly higher thermoelectric figure-

of-merit may be a consequence of the consolidation method, which yielded 98% of the theoretical density, while the La samples introduced here achieved only 85%.

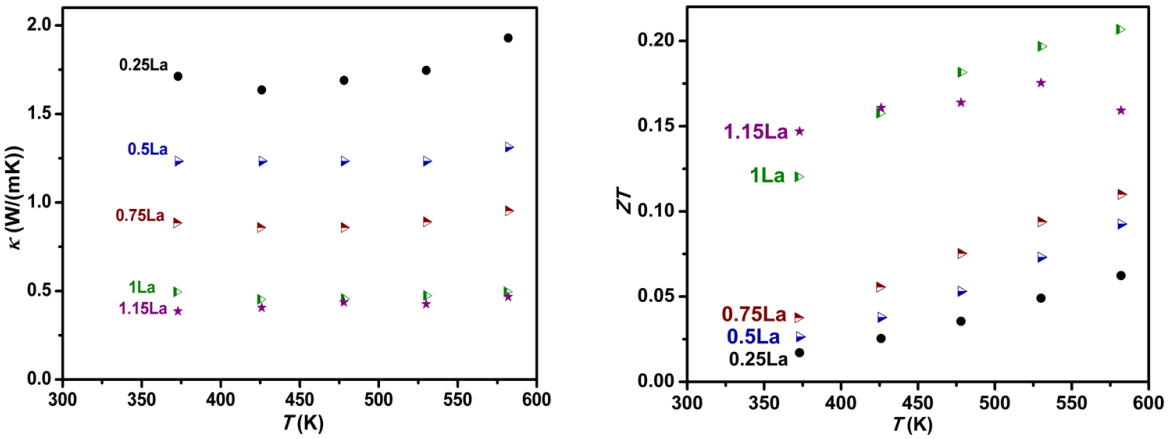

Figure 4.2: Plots of κ vs. T (right) and ZT vs. T (left) for $Tl_{10-x}La_xTe_6$

4.1.2 Thermoelectric properties on hot-pressed Tl_9LaTe_6 pellet

The thermoelectric property of the promising Tl_9LaTe_6 compound was measured on a hot-pressed pellet (at 575 K under pressure of 100 MPa for 30 mins). The hot pressing was carried out at Clemson University. The XRD pattern of the hot-pressed pellet confirmed that the compound did not undergo any kind of decomposition upon hot pressing. The pellet was hot-pressed to achieve the maximum compactness of the polycrystalline material and study the effect of compactness of these materials on thermoelectric properties.

Conduction of electricity depends on the mobility of the carriers which will be improved in a denser material. Ronfard Hared[142] demonstrated that increase in sintering temperature drastically decrease the electrical resistance of the sample, hence, increasing their electrical conductivity.[142] The reason for this is that sintering at higher temperature densifies the sample which improves the mobility of the carriers without disruptions like air pockets. Our present study showed that hot pressing did improve the electrical conductivity, unlike the case of Tl_9BiTe_6, where the electrical resistivity was about 59/(Ωcm) at about 550 K for the zone-refined sample[108] while that of the hot-pressed pellet was about 100/(Ωcm).[66] At 500 K, the σ of the hot pressed sample was 247/(Ωcm)

while that of the sintered pellet was 137/(Ωcm), therefore, an increase by a factor of only approximately 1.5 was observed.

This might be because the density of the sintered pellet was already not bad, about 83%, while that of the hot-pressed pellet was about 95 % of the theoretical density; an improvement of only about 10 % was obtained. This implies that the thallium lanthanoid telluride compounds do get quite compact even when sintering cold-pressed pellets. Since the Seebeck coefficient depends on the carrier concentration and temperature, which are not affected by hot pressing, the Seebeck coefficient data were not improved. *Figure 4.3* shows the plots of electrical conductivity (left) and Seebeck coefficient (right) values of the hot-pressed sample with respect to the sintered pellet.

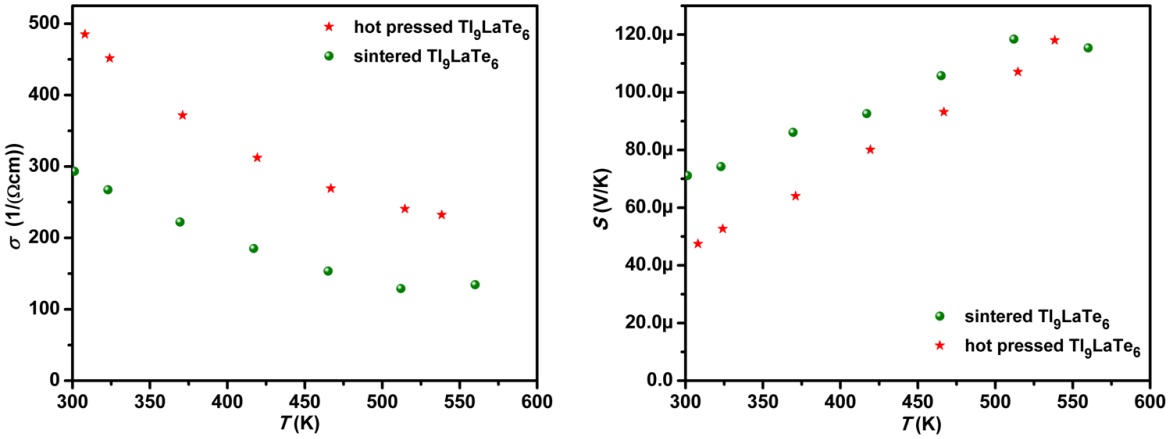

Figure 4.3: Plots of σ vs. T (left) and S vs. T (right) for the sintered and hot-pressed pellet of Tl_9LaTe_6

Thermal conductivity is another parameter of the dimensionless figure of merit that is affected by compactness and porosity.[34, 35, 143, 144] At 500 K, κ of the hot-pressed pellet was 0.51 W/(mK) compared to the sintered pellet which was 0.45 W/(mK); therefore, the data on the hot-pressed sample were little bit higher (by a factor of about 1.1), and this was the case over the whole temperature range measured. Thus, the thermal conductivity values of the hot-pressed pellet with 95 % the theoretical density is not too far from that of the sintered pellet with 83 % the theoretical density (*Figure 4.4*, left). Therefore, the measured thermal diffusivity on the hot-pressed pellet could be

considered as almost same as the thermal diffusivity of a pellet with 100 % theoretical density. Hence, Tl_9LaTe_6 indeed has a low thermal conductivity (0.4 Wm/K - 0.6 W/(mK)) comparable to other thallium based compounds like Ag_9TlTe_5 (0.22 W/(mK) at RT),[107, 145] Tl_4SnTe_3 (0.50 at RT),[107] and Tl_9BiTe_6 (0.39 W/(mK) at RT).[7, 66, 108]

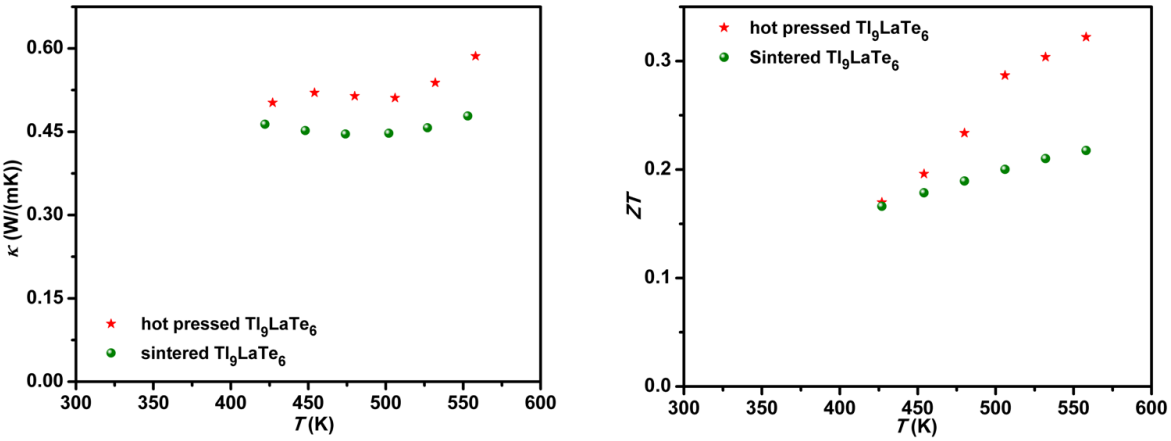

Figure 4.4: Plots of κ vs. T (left) and ZT vs. T (right) for the sintered and hot-pressed pellet of Tl_9LaTe_6

Overall, the *ZT* values on the hot-pressed pellet were improved by a factor of approximately 1.5 (*Figure 4.4*, right), which is minimal, just like in the case of Tl_9BiTe_6, (at about 590 K, *ZT* of a hot pressed pellet is 0.86 while that of a zone refined material is 1.2).[7, 66, 108] However, the results do support the fact that hot-pressed pellets have better thermoelectric properties with respect to cold-pressed pellets.

4.2 Thermoelectric properties of $Tl_{10-x}Ln_xTe_6$, Ln = Nd, Gd, Tb, Dy, Ho, Er; $0.25 \leq x \leq 1.32$

Other thallium lanthanoid telluride compounds of the $Tl_{10}Te_6$ family were synthesized with different lanthanoid elements across the series. Some compounds like Tl_9NdTe_6 and Tl_9GdTe_6 have already been synthesized earlier by Babanly but their thermoelectric properties were not studied.[120, 122, 146] In this chapter the thermoelectric properties of $Tl_{10-x}Ln_xTe_6$, Ln = Nd, Gd, Tb, Dy, Ho, Er; $0.25 \leq x \leq 1.32$, are discussed in two parts:

a) as x increases for a given Ln phase (all data generally correlates with the observed trend for $Tl_{10-x}La_xTe_6$ phase).

b) across the f-block series for a particular stoichiometry, $x \approx 1$.

4.2.1 Thermoelectric properties of $Tl_{10-x}Ln_xTe_6$, Ln = Nd, Gd, Tb, Dy, Ho, Er; $0.25 \leq x \leq 1.32$ as x increases

According to *Equation 1.7*, as T increases, S increases, but at the same time, as n increases, S decreases; therefore, overall S would depend on which parameter dominates in a particular situation. S values of all the compounds were measured from 300 K to 600 K, and the positive S values throughout the measurement showed that all the compounds are p-type semiconductors. Compounds with $x > 1$ are supposed to be n-type semiconductors as Tl_9LnTe_6 is an intrinsic semiconductor, however, $Tl_{8.88}Ce_{1.12(6)}Te_6$, $Tl_{8.68}Nd_{1.32(6)}Te_6$ and $Tl_{8.84}Gd_{1.16(8)}Te_6$ were all p-type semiconductors just like $Tl_{8.85}La_{1.15}Te_6$.[117] This is likely due to defects in the structure, which have been responsible for p-type character for GeTe[147] and nGeTe.$m$$Sb_2Te_3$[148] compounds as well.

Unlike $Tl_{8.85}La_{1.15}Te_6$,[117] $Tl_{8.88}Ce_{1.12(6)}Te_6$, $Tl_{8.68}Nd_{1.32(6)}Te_6$ and $Tl_{8.84}Gd_{1.16(8)}Te_6$ did not show a maximum S within the measurement temperature range (300 K – 600 K), therefore, throughout the measurement, T was more dominant, as T increases S increases. All the other compounds gave the same trend, S of $Tl_{9.25}Nd_{0.75}Te_6$, $Tl_{8.98}Nd_{1.02(6)}Te_6$ and $Tl_{8.68}Nd_{1.32(6)}Te_6$ increases from 34 μV/K, 46 μV/K and 70 μV/K (at ~ 300 K) to 79 μV/K, 92 μV/K and 109 μV/K respectively (at ~ 550 K). Similarly, S of $Tl_{9.75}Tb_{0.25}Te_6$, $Tl_{9.50}Tb_{0.50}Te_6$, $Tl_{9.26}Tb_{0.74(7)}Te_6$ and $Tl_{9.01}Tb_{0.99(5)}Te_6$ increases from 18 μV/K, 14 μV/K, 24 μV/K and 30 μV/K to 36 μV/K, 44 μV/K, 53 μV/K and 63 μV/K respectively. These values also suggest that as x increases, S increases just like for the lanthanum series[117], this is because as x increases, the number of electron in the system increases, hence decreasing the number of holes, which are the carriers in such compounds. As a result, n decreases leading to an increase in S as $S \propto n^{-2/3}$ (*Figure 4.5*, left). However, from the S vs. x plot of $Tl_{10-x}Ce_xTe_6$ phase, one could interpret the fit in two ways either as an increase in S as x increases with the value for $x \sim 1$ off the fit or an increase in S as x increases with the value for $x \sim 1.12$ off the trend. The off trend for the value of x ~ 1

could be due to the shape of the DOS curve as $S \propto (\partial DOS(E)/\partial E)|_{E = E_F}$.[27, 28] Other than the shape of the DOS curve, the off trend value for $x \sim 1.12$ could be explained by the possibility of the presence of more Ce^{4+} in $Tl_{8.88}Ce_{1.12(6)}Te_6$ than in $Tl_{8.97}Ce_{1.03(5)}Te_6$ (the possible presence of some percentage of Ce^{4+} in the structure may be indicated by the smaller unit cell volume than expected). When Ce^{3+} goes to Ce^{4+}, an extra electron becomes available hence fewer carriers will be present, consequently *n* decreases and *S* increases. Similar anomalies were observed for the gadolinium phase, $Tl_{10-x}Gd_xTe_6$ and erbium phase $Tl_{10-x}Er_xTe_6$. The *S* values of $Tl_{9.32}Gd_{0.68(8)}Te_6$ increase from 33 μV/K to 72 μV/K and that of $Tl_{9.05}Gd_{1.0(1)}Te_6$ increases from 28 μV/K to 67 μV/K, indicating that unexpectedly, *S* values of $Tl_{9.32}Gd_{0.68(8)}Te_6$ were greater than that of $Tl_{9.0}Gd_{1.0(1)}Te_6$ throughout the temperature range studied. The most plausible explanation for this might be presence of more gadolinium in the structure base on the EDX data for $Tl_{9.32}Gd_{0.68(8)}Te_6$, and in the worst case scenario, with an error of 3σ, the formula could be $Tl_{9.05}Gd_{0.96}Te_6$. Moreover, it could also be the smaller gradient $(\partial DOS(E)/\partial E)|_{E = E_F}$ at the Fermi level in the DOS curve for $Tl_{9.0}Gd_{1.0(1)}Te_6$, that would result in a smaller *S*.[27, 28] A similar explanation could be postulated for the fact that *S* of $Tl_{9.92}Er_{0.79(6)}Te_6$ is almost the same as that of $Tl_{9.05}Er_{0.95(5)}Te_6$ over the whole temperature range measured instead of being smaller.

Since σ is directly proportional to *n* according to the equation $\sigma = n\mu e$, where, μ = carrier mobility and *e* = charge of carriers, and as mentioned above, *S* has $n^{-2/3}$ dependence, *S* and σ are related inversely through *n*. Therefore, hypothetically, the opposite observation is expected for the σ trend. The experimental results support this expectation: as *x* increases, σ decreases for a particular series due to the decrease in *n* (*Figure 4.5*, right). Furthermore, as *T* increases, σ decreases. This is because $\mu = \tau/m^*$, where τ is the relaxation time, which decreases with increasing temperature. This leads to a decrease in carrier mobility as *T* increases, hence decreasing σ. At some point, the decrease in μ can be outweighed by the increase in *n* when the carriers have enough energy to overcome the forbidden gap. In this study, none of the compounds reached that point; irrespective of their stoichiometries, σ decreases as *T* increases for all the

compounds throughout the temperature range studied. σ of $Tl_{9.25}Nd_{0.75}Te_6$, $Tl_{8.98}Nd_{1.02(6)}Te_6$ and $Tl_{8.68}Nd_{1.32(6)}Te_6$ decreases from 666/(Ωcm), 520/(Ωcm) and 268/(Ωcm) at 307 K to 341/(Ωcm), 285/(Ωcm) and 123/(Ωcm) at 542 K respectively. The gadolinium phase again showed some anomalies, σ data of $Tl_{9.32}Gd_{0.68(8)}Te_6$ and $Tl_{9.0}Gd_{1.0(1)}Te_6$ were very close, ranging from 868/(Ωcm) at 307 K to 430/(Ωcm) at 545 K and from 856/(Ωcm) at 307 K to 435/(Ωcm) at 545 K respectively, the expected observation (σ of $Tl_{9.32}Gd_{0.68(8)}Te_6$ > σ of $Tl_{9.0}Gd_{1.0(1)}Te_6$) was not made. This was also the case for $Tl_{9.92}Er_{0.79(6)}Te_6$ and $Tl_{9.05}Er_{0.95(5)}Te_6$.

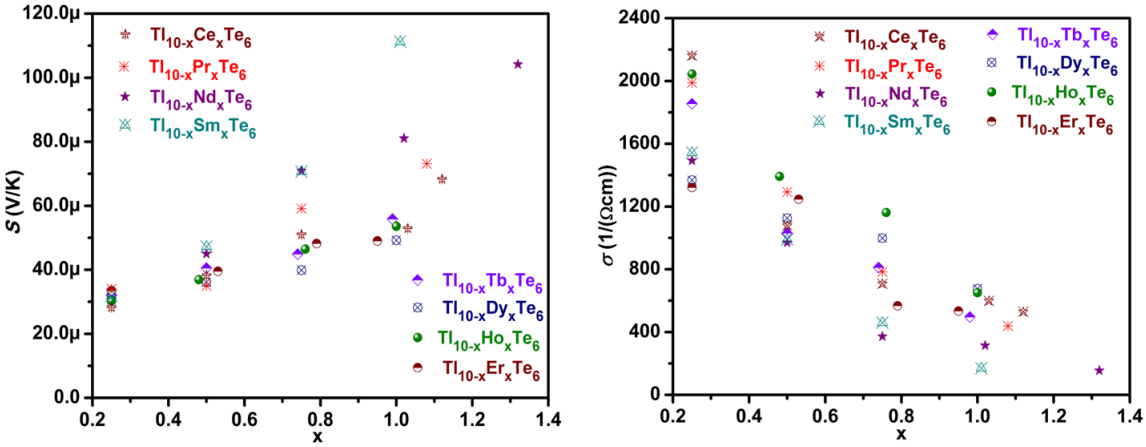

Figure 4.5: Plots of *S* vs. *x* (left) and σ vs. *x* (right) for $Tl_{10-x}Ln_xTe_6$

From the plot, the increase in *S* with *x* could be considered as linear with respect to the increase in σ except for the samarium phase. *S* of $Tl_{8.99}Sm_{1.01(7)}Te_6$ is exceptionally high, which makes the plot non-linear.

The third important parameter in the *ZT* equation is the thermal conductivity, κ, which consists of two components, the electronic thermal conductivity, κ_e, and the lattice thermal conductivity, κ_l. As per the Wiedemann-Franz law, $\kappa_e = L\sigma T$ where *L* is the Lorenz number, which is often assumed to be the Sommerfeld value, 2.44×10^{-8} V^2K^{-2}.[30] On the other hand, $\kappa_l = (/3)C_p v l_t$, where C_p is the specific heat capacity, *v* is the speed of light and l_t is the mean free path. κ_e decreases with increasing *T* and *x*. The Wiedemann-Franz-Lorenz law did not work for most of the compounds with $x \leq 1$ and gave too small

or negative κ_l. This might be because L might vary with temperature from case to case as shown in *Table 1.1*.[31]

Moreover, in defective crystals, which is most probably the case for the compounds in this study, the lattice thermal conductivity may be significantly smaller.[31] Another reason could be presence of pores in the samples as in the studies of the effect of porosity on thermal and electrical properties of polycrystalline bulk ZrN, Adachi and co-workers observed higher electronic thermal conductivity than the total thermal conductivity.[143] The effect of pores on thermal conductivity was extensively studied in the 50s.[34, 35, 144] Furthermore, lightly doped semiconductors experience bipolar thermodiffusion effect that results in higher κ_e.[31] When there are more than one type of carriers contributing to the electronic properties in a material, the κ_e of the material is greater than the sum of the electronic thermal conductivity due to each type of carrier as a third term involving the partial electronic conductivity and partial Seebeck coefficients is included in the sum.[31] A greater κ_e than expected would fail the Wiedemann-Franz-Lorenz law. κ_e of $Tl_{9.25}Nd_{0.75}Te_6$, and $Tl_{8.68}Nd_{1.32(6)}Te_6$ decreases from 0.47 W/(mK) and 0.20 W/(mK) at about 427 K to 0.46 W/(mK) and 0.18 W/(mK) at about 557 K respectively.

κ_l is expected to decrease as T increases due to a decrease in the mean free path, l_t as a result of increasing lattice vibration. However, throughout the whole measurement from 425 K to 550 K, the expected trend was obtained only for seven compounds mentioned below,

- $Tl_{9.25}Nd_{0.75}Te_6$, κ_l varied from 0.47 W/(mK) to 0.26 W/(mK)
- $Tl_{9.25}Ce_{0.75}Te_6$, κ_l varied from 0.33 W/(mK) to 0.25 W/(mK)
- $Tl_{9.75}Dy_{0.25}Te_6$, κ_l varied from 0.49 W/(mK) to 0.34 W/(mK)
- $Tl_{9.5}Dy_{0.5}Te_6$, κ_l varied from 0.45 W/(mK) to 0.23 W/(mK)
- Tl_9DyTe_6, κ_l varied from 0.31 W/(mK) to 0.27 W/(mK)
- $Tl_{9.19}Er_{0.81(6)}Te_6$, κ_l varied from 0.67 W/(mK) to 0.57 W/(mK)
- $Tl_{9.5}Pr_{0.5}Te_6$, κ_l varied from 0.71 W/(mK) to 0.54 W/(mK)

For other compounds, κ_l was either independent of temperature (as the changes in κ_l with temperature were within 0.10 W/(mK)) or gave the opposite trend. κ_l of $Tl_{9.25}Nd_{0.75}Te_6$ increased from 0.36 W/(mK) at 425K to 0.49 W/(mK) at 550 K. This data indicates that the increase in phonon scattering with increasing temperature was not dominant for that temperature range and most probably the temperature at which the heat capacity becomes constant, which is about 100 K for $IrSb_3$,[149] is not yet reached like in the case of Be_2C.[33, 30]

The data for the dysprosium series indicates that as x increases, κ_l decreases. As x increases, the lighter atoms are incorporated in the structure at the *4c* site which was previously occupied by heavier thallium atoms. This substitution increases both the mass fluctuation resulting in phonon scattering and the lattice vibration resulting in decrease of the mean free path, l_t. A similar observation was made for the gadolinium and samarium phases.

The general observations made for the temperature dependence of total thermal conductivity, κ, of the compounds evaluated in this study are mentioned below:

- as for the lanthanum phase range, most of the compounds did exhibit an initial decrease to a minimum in κ followed by an increasing tendency with increasing T, but, since the change was not significant, it can be concluded that κ was basically temperature independent.
- Compounds like $Tl_{9.25}Ln_{0.25}Te_6$, Ln = Ce, Nd, Dy and Er; $Tl_{9.5}Ln_{0.5}Te_6$, Ln = Pr, Dy, Er and $Tl_{9.25}Dy_{0.75}Te_6$ gave a general decreasing tendency, this is understandable as their plots of σ versus T showed a steep smooth decrease with T, reducing κ_e.
- Completely opposite trends were obtained for $Tl_{9.5}Nd_{0.5}Te_6$ and $Tl_{9.25}Nd_{0.75}Te$, where κ increases slightly. This might be due to an increase in κ_e, in which case increasing T is more important than decreasing σ, or due to increasing κ_l as calculated for $Tl_{9.25}Nd_{0.75}Te_6$.

On the other hand, the general observations made for the total thermal conductivity, κ, with increasing x for compounds within a particular phase were in agreement with that of the lanthanum phase for most compounds. κ decreases with

increasing *x* (*Figure 4*, top left) except for the praseodymium, samarium and gadolinium phases discussed below. κ of $Tl_{9.0}Gd_{1.0(1)}Te_6$ (1.13 W/(mK) to 1.08 W/(mK)) was slightly greater than that of $Tl_{9.32}Gd_{0.68(8)}Te_6$ (0.99 W/(mK) to 0.92 W/(mK)). A similar discrepancy was observed for $Tl_{10-x}Ln_xTe_6$, for x = 0.25 and 0.5 of the praseodymium phase and for x = 0.5 and 0.82(8) of the samarium phase. Most probably the decrease in average molar weight as x increases was more important than the increase in both the mass fluctuation and lattice vibration for the $Tl_{9.0}Gd_{1.0(1)}Te_6$ compound.

The power factor ($S^2\sigma$) for the temperatures at which κ were measured, were obtained from the fit of $S^2\sigma$ vs. *T* plots and used to get the *ZT* at *T*. Since *ZT* is directly proportional to *T* ($ZT = S^2\sigma T/\kappa$), for all the compounds *ZT* was observed to increase with increasing *T*. *ZT* was observed to increase as *x* increases for the neodymium, dysprosium and erbium phases, for that of samarium, gadolinium, terbium and holmium phases, the trend has been disrupted (*Figure 4.6*, right). *ZT* of $Tl_{9.5}Sm_{0.5}Te_6$ > $Tl_{9.18}Sm_{0.82(8)}Te_6$, that of $Tl_{8.83}Gd_{1.17(5)}Te_6$ was smaller than $Tl_{9.0}Gd_{01.0(1)}Te_6$ and $Tl_{9.32}Gd_{0.68(8)}Te_6$ throughout the temperature range studied. This is most probably due to the smaller κ values of $Tl_{9.5}Sm_{0.5}Te_6$ and $Tl_{9.32}Gd_{0.68(8)}Te_6$. Comparing the data of $Tl_{9.24}Ho_{0.76(8)}Te_6$ and Tl_9HoTe_6, the difference in their *S* values is about 10 μV/K - 20 μV/K while the difference in their σ values is about 600/(Ω cm) - 800/(Ω cm) throughout the temperature range studied, as a result, the *ZT* of $Tl_{9.24}Ho_{0.76(8)}Te_6$ is greater than Tl_9HoTe_6 despite the lower κ of the latter. Similarly, *ZT* of $Tl_{9.01}Tb_{0.99(5)}Te_6$ is smaller than that of $Tl_{9.26}Tb_{0.74(7)}Te_6$, due to the smaller decrease in *S* for $Tl_{9.01}Tb_{0.99(5)}Te_6$ with respect to that of $Tl_{9.26}Tb_{0.74(7)}Te_6$, despite the increase and decrease in σ and κ respectively.

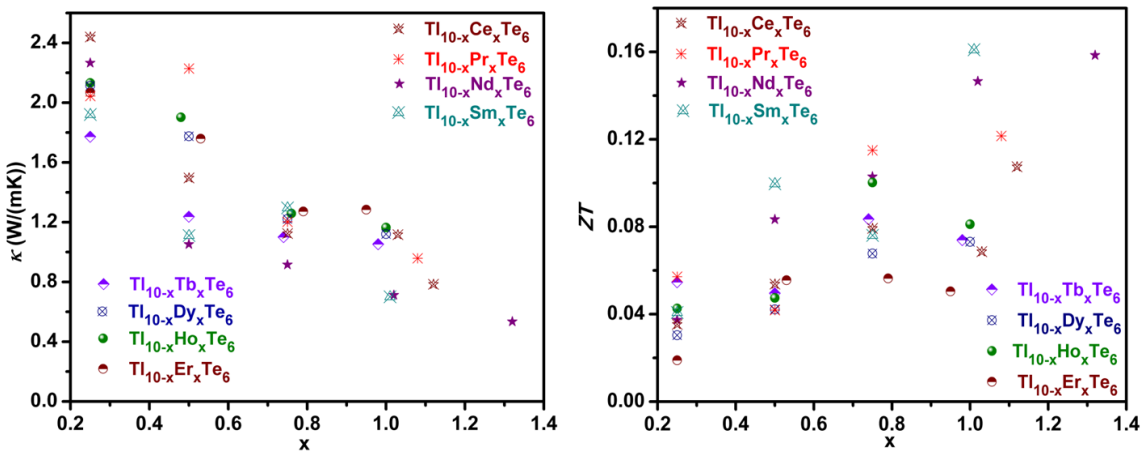

Figure 4.6: Plots of κ vs. x (left) and ZT vs. x (right) for $Tl_{10-x}Ln_xTe_6$

Among all the phases, $Tl_{10-x}Pr_xTe_6$ and $Tl_{10-x}Sm_xTe_6$ were unique in having a disruption in the general trend of κ with increasing x. However, $Tl_{10-x}Gd_xTe_6$ is the only phase which disagreed with the general trend of the rest of the phases with increasing x for all the parameters (S, σ and κ). *Figure 4.7* shows thermoelectric properties with increasing temperature for the gadolinium phase.

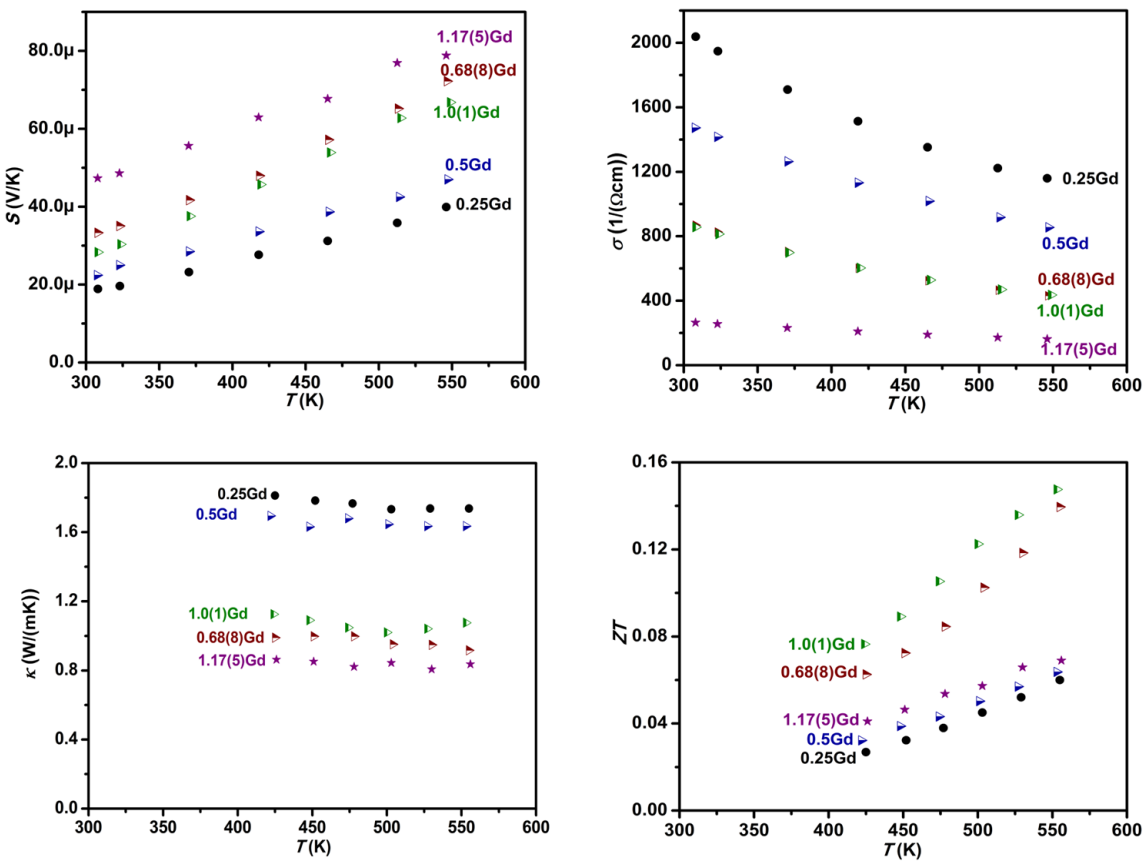

Figure 4.7: TE of $Tl_{10-x}Gd_xTe_6$

4.2.2 Thermoelectric properties of Tl_9LnTe_6 across the series, Ln = Nd, Gd, Tb and Er

In this discussion, the stoichiometry $Tl_{10-x}Ln_xTe_6$, $x \approx 1$ for Ln = Ce, Pr, Nd, Sm, Gd, Tb, Er in particular is taken in consideration because the nominal mole ratios are very close to the ones obtained from the refinements. Tl_9DyTe_6 and Tl_9HoTe_6 did not agree with the σ trend most probably because Tl_9DyTe_6 is off stoichiometry and Tl_9HoTe_6 has a secondary phase as per the EDX data. However, these two phases were considered for this study because S and κ were not as much affected as σ was. The properties of Tl_9CeTe_6, Tl_9PrTe_6 and Tl_9SmTe_6 are discussed separately as they exhibit anomalous properties with respect to the rest of the series.

Across any period of the periodic table, atomic size decreases from left to right, and so do the covalent radii and bond lengths.[97] This hypothesis supports the data for the

lattice parameters and unit cell volume obtained from the refinements. The decrease in unit cell volume for $Tl_{10-x}Ln_xTe_6$, $x \approx 1$ for Ln = Nd, Gd, Tb, Er, across the lanthanoid series is an ultimate result of a decrease in bond lengths, which implies stronger bonds due to better overlap. We postulate that across the series, due to the decrease in atomic size, orbitals involved in bonding would overlap better, resulting in bigger bandwidth, in other words, a smaller band gap.

Unfortunately, we were unable to determine the band gaps of these compounds to confirm our explanations, as their conductivity plots are far from an exponential curve. In the case of an exponential T dependence of σ, the band gap can be obtained from the slope of the Arrhenius plot of $\ln\sigma$ vs./T.

Moreover, the optical properties measurements were not done on thallium lanthanoid tellurides due to the presence to many intrinsic carriers in these compounds. The band gap of a material can also be obtained from the TAUC plot (*Figure 5.8*, plot of $(h\nu\alpha)^{½}$ vs. $h\nu$ where $h\nu$ is the energy of the light and α is the absorption coefficient of the material) which can be obtained from the diffuse reflectance solid state UV-NIR spectroscopic analysis.[150]

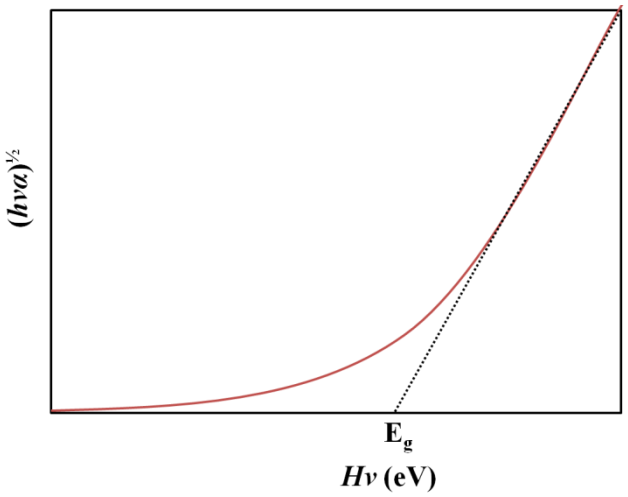

Figure 4.8: Schematic illustration of a TAUC plot

Based on the postulation that the band gap decreases across the series, which is supported by the DOS plots calculated using the LMTO and WIEN2*k* package (*Figure*

3.14 and *Figure 3.15*), and hypothetically, σ depends on band gap, E_g; the decrease in the σ trend from Tl_9LaTe_6 to Tl_9CeTe_6 indicates an increase in band gap. The intrinsic carriers would cross the smaller forbidden energy gap easier as we move across the series. Consequently, σ is expected to increase and this is indeed observed (*Figure 4.9*, top right). At about 500 K, σ of $Tl_{9.98}Nd_{1.02(6)}Te_6$ and $Tl_{9.05}Er_{0.95(5)}Te_6$ are about 315/(Ωcm) and 537/(Ωcm) respectively.

On the other hand, since σ is directly proportional to *n*, *S* is expected to decrease across the lanthanoid series (*Figure 4.9*, bottom right). At about 500 K, *S* of $Tl_{9.98}Nd_{1.02(6)}Te_6$ and $Tl_{9.05}Er_{0.95(5)}Te_6$ are about 81 μV/K and 50 μV/K respectively.

The discontinuity in the σ curve of Tl_9DyTe_6 and Tl_9HoTe_6 is obvious in *Figure 4.9* (top right). Their σ values are higher than that of Tl_9ErTe_6 throughout the measurement (*Figure 4.9*, top left), somewhat, agreeing with the EDX data suggesting that there are about 20% - 25% less Dy in the Tl_9DyTe_6 compound. Hence, the σ data is higher than expected as σ decreases with increasing *x* (*Section 4.3.1*). The reason for the higher σ data of the Tl_9HoTe_6 compound might be its inhomogeneity (as the presence of secondary, Ho rich phase) implying that the compound resulting from that reaction was mainly of the $Tl_{10-x}Ho_xTe_6$ phase, with *x* less than 1; hence higher σ data is justified.

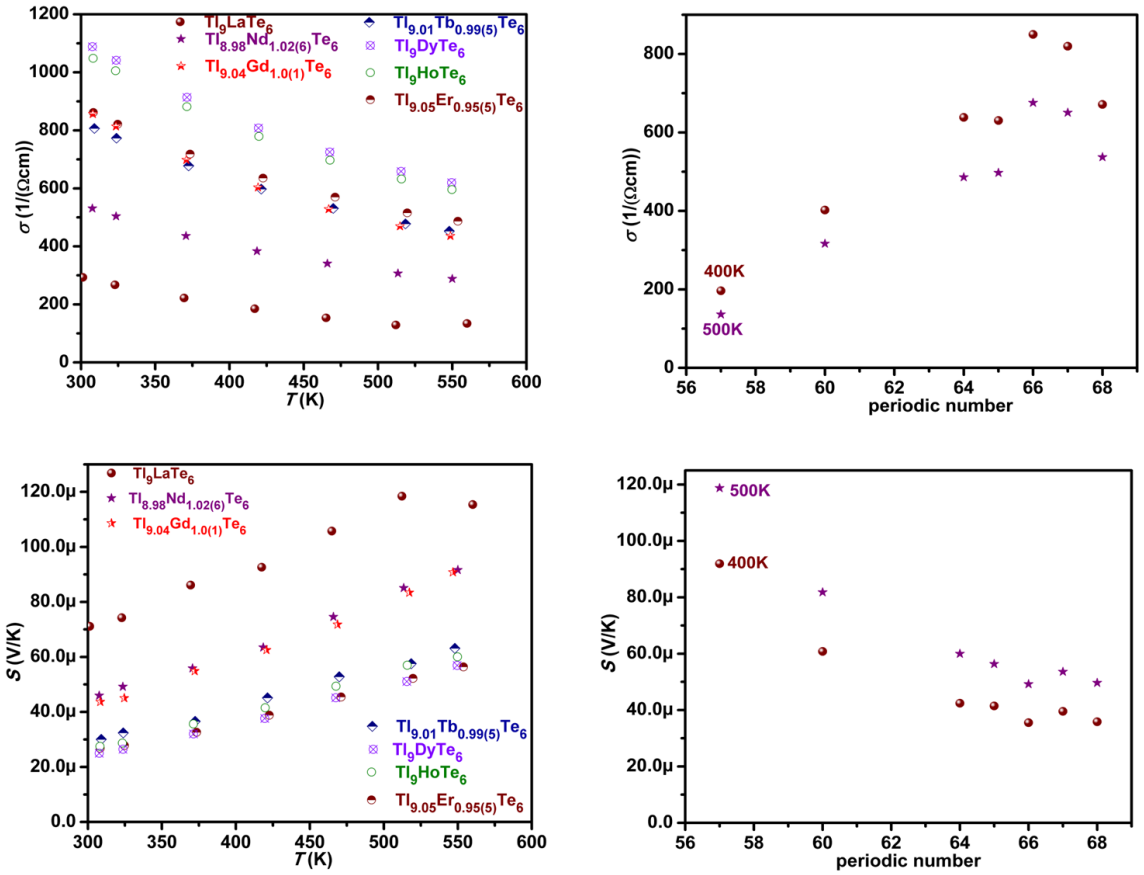

Figure 4.9: Plots of σ vs. T (top left), S vs. T (bottom left); plots of σ (top right) and S (bottom right) vs. periodic number for Tl_9LnTe_6, Ln =La, Nd, Gd, Tb, Dy, Ho and Er

As for κ, it is expected to increase across the lanthanoid series because both the electronic and thermal contribution is expected to increase from the lanthanum compound to erbium compound. The increase in σ increases κ_e; on the other hand, the increase in atomic mass across the period would cause a decrease in mass fluctuation and lattice vibration from Tl_9LaTe_6 to Tl_9ErT_6 in turn results in increase in κ_l. κ_e of of $Tl_{9.98}Nd_{1.02(6)}Te_6$ and $Tl_{9.05}Er_{0.95(5)}Te_6$ are about 0.39 W/(mK) and 0.67 W/(mK) respectively, while their κ_l are about 0.39 W/(mK) and 0.60 W/(mK) respectively. As a result, the overall κ increases across the series from 0.71W/(mK) for $Tl_{9.98}Nd_{1.02(6)}Te_6$ to 1.28 W/(mK) for $Tl_{9.05}Er_{0.95(5)}Te_6$ at about 500 K (*Figure 4.10*, top right).

ZT was calculated in the same way as mentioned in *Section 4.1.1* and *Section 4.2.1*, it was observed to decrease across the series due to the decrease in *S* and increase in κ despite the increase in σ. In accord with the discontinuity in the σ trend, the *ZT* for the Tl_9DyTe_6 and Tl_9HoTe_6 compounds at 500 K did again experience a discontinuity in the trend (*Figure 4.10*, bottom right). At about 500 K, *ZT* of $Tl_{9.98}Nd_{1.02(6)}Te_6$ was 0.15 while that of $Tl_{9.05}Er_{0.95(5)}Te_6$ was 0.05.

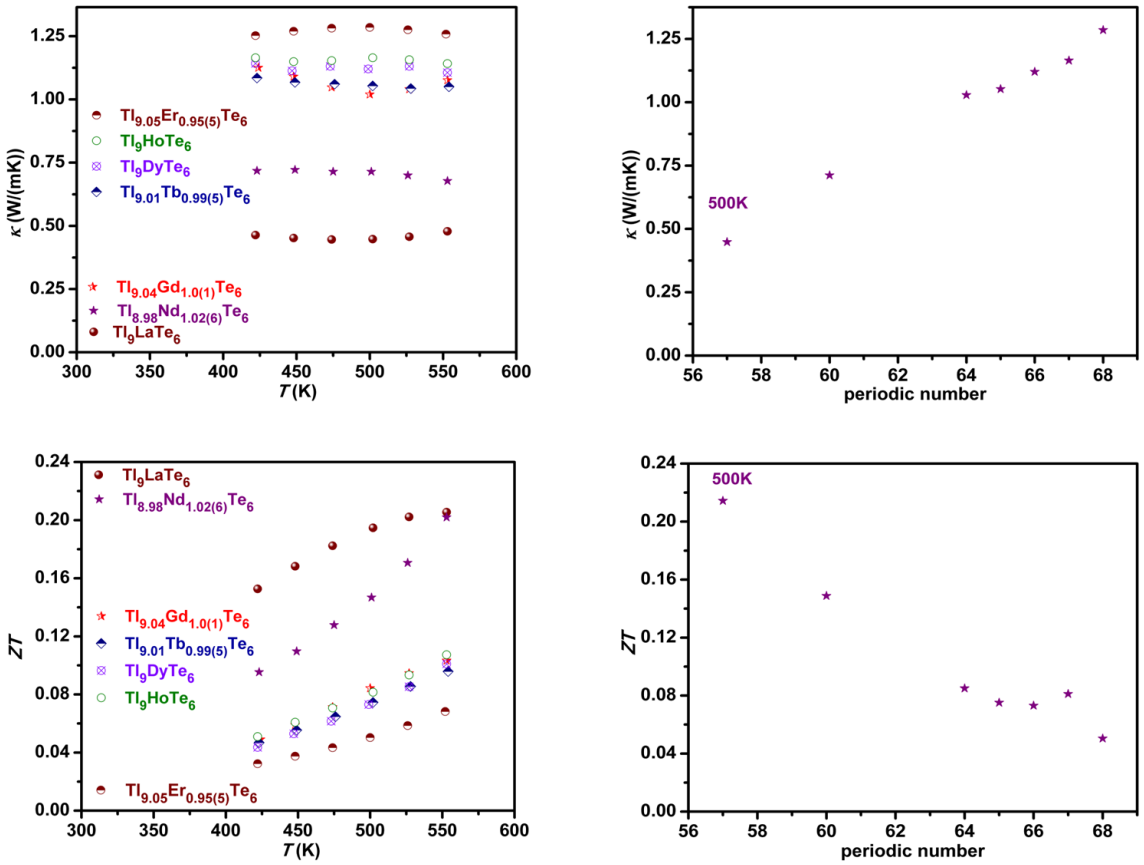

Figure 4.10: Plots of κ vs. *T* (top left), *ZT* vs. *T* (bottom left); plots of κ (top right) and *ZT* (bottom right) vs. periodic number for Tl_9LnTe_6, Ln = La, Nd, Gd, Tb, Dy, Ho and Er

4.3 Anomalous thermoelectric properties of Tl_9LnTe_6 across the series, Ln = Ce, Pr and Sm

According to the hypothesis discussed above, across the lanthanoid series,

- σ is expected to increase due to the decreasing band gap of the compounds of the f-block elements when moving from the left to the right of series
- *S* is expected to decrease due to increasing σ as σ and *S* are inversely related through *n*
- κ is expected to increase if the decrease in mass fluctuation and lattice vibration is less important than the increase in the average molar weight (increasing average molar weight would decrease the specific heat capacity hence κ)

However, the above expected observations were not made; instead, the opposite results were obtained:

- σ of $Tl_{8.97}Ce_{1.03(5)}Te_6 > Tl_{8.98}Pr_{1.08(8)}Te_6 > Tl_{8.99}Sm_{1.01(7)}Te_6$ throughout the whole temperature range (*Figure 4.11*, bottom left).
- Based on the correlation of *S* and σ, *S* did give the opposite trend with respect to σ, *S* of $Tl_{8.97}Ce_{1.03(5)}Te_6 < Tl_{8.98}Pr_{1.08(8)}Te_6 < Tl_{8.99}Sm_{1.01(7)}Te_6$ throughout the whole temperature range (*Figure 4.11*, top left).
- κ of Tl_9LnTe_6 decreases from the cerium compound to the praseodymium compound to the samarium compound (*Figure 4.13*, top left).

The σ and *S* values of the three compounds were calculated at 400 K and 500 K from the fit of previous plots (σ and *S* vs. *T*, *Figure 4.9*, top and bottom left). *Figure 4.11* (top and bottom right) reveals the discontinuity in the expected trend postulated above; the solid lines are the fits for the general trends based on the plots of σ and *S* vs. periodic number (*Figure 4.9*, top and bottom right).

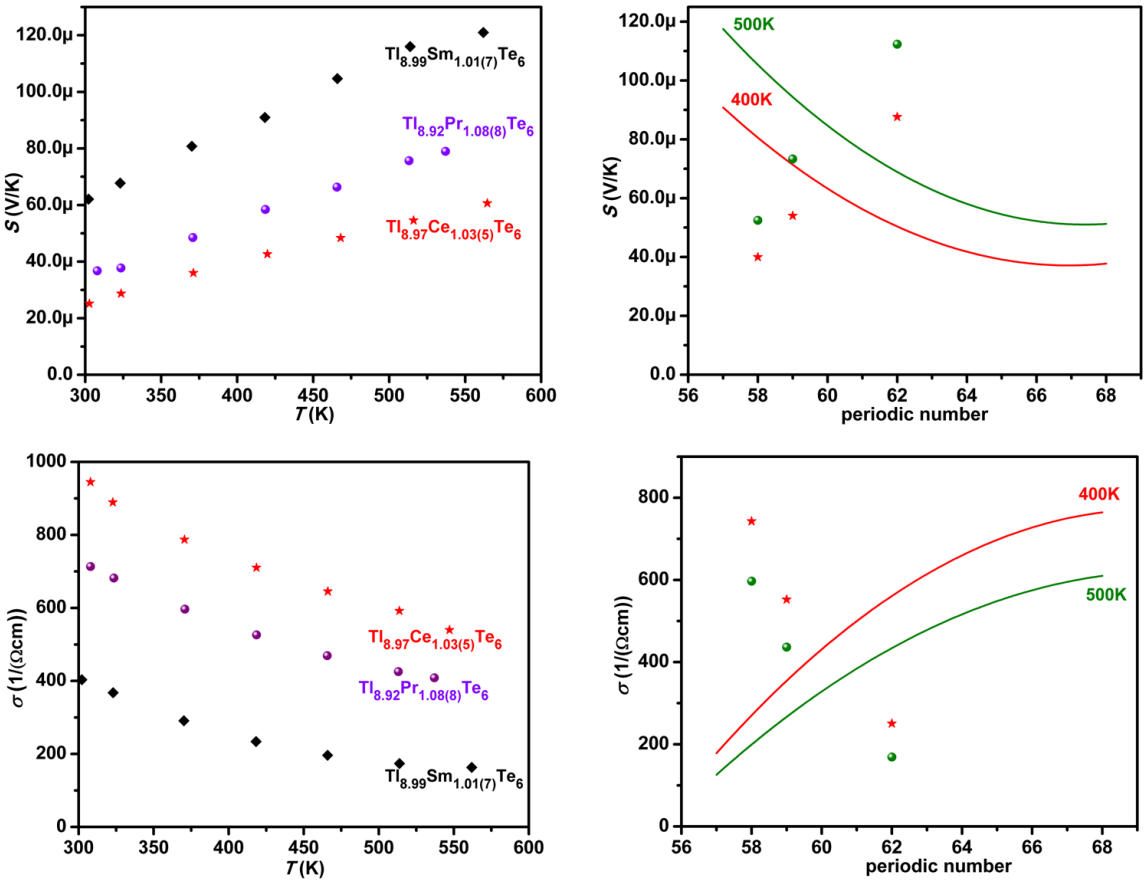

Figure 4.11: Plots of *S* vs. *T* (top left), σ vs. *T* (bottom left); plots of anomalous *S* (top right) and σ (bottom right) vs. periodic number for Tl_9LnTe_6, Ln = Ce, Pr and Sm

The lowest σ value for Tl_9LaTe_6 and highest σ value for Tl_9CeTe_6 at 500 K suggest that Tl_9CeTe_6 has the smallest band gap and Tl_9LaTe_6 has the highest band gap. Based on the DOS plots discussed in *Section 3.4*, Tl_9LaTe_6 does have the highest band gap and across the series from La to Er, the band gap of Tl_9LnTe_6 decreases justifying the increase in σ. However, the increase in σ across the series is not smooth most probably due to the discontinuity in the decrease in the band gap; a similar discontinuity in band gap is observed for the Ln_2Q_3 (Q = O, S, Se).

The variation of band gaps of Ln_2Q_3 (Q = O, S and Se)[139] supports the trend we postulate for the band gaps of Tl_9LnTe_6 across the series. The band gaps of La_2Q_3 were the largest in the series due to the empty 4f-levels in La^{3+} lying much higher than the bottom of the 5d-band. On the other hand, the smallest band gap for the Ce_2Q_3

compounds were proposed to be due to the presence of Ce^{4+}.[139] Ce^{4+} has a stabilised [Xe] configuration, hence the 4f-orbitals are stabilised and become lower than the d-shell, as a result the 4f band falls in the forbidden gap and the band gap is determined from the 4f-5d transition.[92, 139] *Figure 4.12* shows the variation in band gap of Ln_2S_3 and Ln_2Se_3 across the series, La_2S_3 and La_2Se_3 have the greatest band gap, Ce_2S_3 and Ce_2S_3 exhibit the smallest band gap and Sm_2S_3 and Sm_2Se_3 had band gaps off the trend for the series. Therefore, we postulate that $Tl_{8.97}Ce_{1.03(5)}Te_6$ has the smallest band gap (highest σ) most probably due to the presence of Ce^{4+} in the structure.

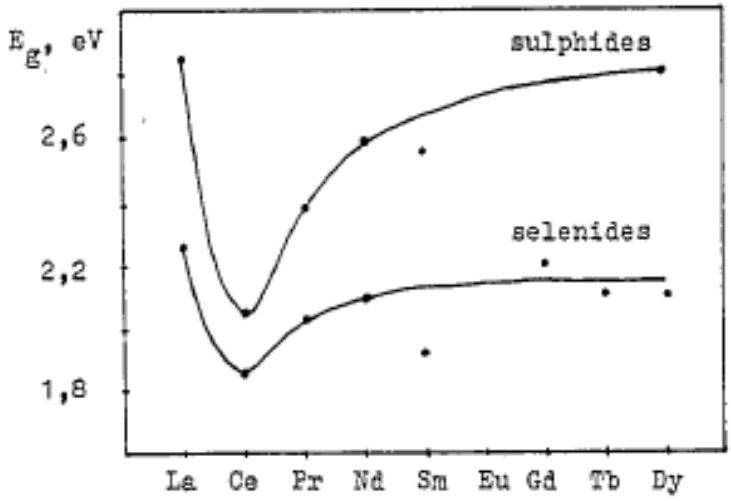

Figure 4.12[139]: E_g for Ln_2Q_3, Q = S and Se across the period

σ of $Tl_{8.98}Pr_{1.08(8)}Te_6$ is also higher than expected, probably due to the presence of more than 6.25% of Pr in the structure as per its unit cell volume and EDX data, discussed in *Section 3.2*. $Tl_{8.99}Sm_{1.01(7)}Te_6$ was a homogenous compound which showed the expected atomic percent as per the EDX data; moreover, its unit cell volume correlates nicely with the general tendency across the Tl_9LnTe_6 series, yet the physical properties do not fit the general trend. The discrepancy in the $Tl_{8.99}Sm_{1.01(7)}Te_6$ electrical conductivity and Seebeck coefficient data might be due to the band gap of the latter being off the trend with respect to the rest of the series, as is the case for Sm_2S_3 and Sm_2Se_3 in the Ln_2S_3 and Ln_2Se_3 series respectively.

Given the anomalous *S* and σ data of the $Tl_{8.97}Ce_{1.03(5)}Te_6$, $Tl_{8.92}Pr_{1.08(7)}Te_6$ and $Tl_{8.99}Sm_{1.01(7)}Te_6$ phases with respect to the rest of the Tl_9LnTe_6 series, it is not a surprise to have κ data that would not fit in the trend across the lanthanoid series or that would even be completely opposite to the expected trend. *Figure 4.13* shows the general trend at 500 K for the rest of the Tl_9LnTe_6 series (solid line), there is an obvious increase in κ on moving from left to the right of the f-block element, however, the κ decreases from $Tl_{8.97}Ce_{1.03(5)}Te_6$ to $Tl_{8.92}Pr_{1.08(7)}Te_6$ to$Tl_{8.99}Sm_{1.01(7)}Te_6$, this is true for any temperature ranging from 400 K to 600 K (*Figure 4.13,* top left).

Since κ depends on κ_e, which depends on σ, and κ_l depends on phonon scattering, average molar weight and lattice mean free path, the fact that κ of $Tl_{8.97}Ce_{1.03(5)}Te_6$ > $Tl_{8.98}Pr_{1.08(8)}Te_6$ > $Tl_{8.99}Sm_{1.01(7)}Te_6$ can be justified in two ways.

- Since there is an abrupt increase in σ from Tl_9LaTe_6 to $Tl_{8.97}Ce_{1.03(5)}Te_6$, the κ_e also would exhibit a sudden increase, which would result in a sudden increase in κ data. Since σ decreases from cerium to samarium ($Tl_{8.97}Ce_{1.03(5)}Te_6$ > $Tl_{8.98}Pr_{1.08(8)}Te_6$ > $Tl_{8.99}Sm_{1.01(7)}Te_6$), κ_e would behave similarly and so would κ.
- A second scenario might be that he increase in molar average weight is more important from $Tl_{8.97}Ce_{1.03(5)}Te_6$ to $Tl_{8.99}Sm_{1.01(7)}Te_6$; hence, resulting in decreasing κ due to a decrease in κ_l as C_p will go down (0.1444 J/K, 0.1457 J/K and 0.1459 J/K for Ce, Pr and Sm compound respectively).

However, after scrutinizing the κ_l data, this second postulation should be rejected as κ_l increased instead from $Tl_{8.97}Ce_{1.03(5)}Te_6$ (~ 0.38 W/(mK)) to $Tl_{8.98}Pr_{1.08(8)}Te_6$ (~ 0.45 W/(mK)) to $Tl_{8.99}S_{m1.01(7)}T_{e6}$ (~ 0.50 W/(mK)). Therefore, the decrease in mass fluctuation and lattice vibration is more important in this case. Therefore the decrease in κ_e is more significant than the increase in κ_l from cerium to samarium compound.

According to the anomalies in the σ, *S* and κ trend for these three compounds, their off trend *ZT* values with respect to the rest of the series is understandable. Across the series from Tl_9CeTe_6 to Tl_9SmTe_6, the expected decrease in *ZT* was not obtained, instead an increase was observed. Tl_9SmTe_6 had the maximum *ZT* (0.12 – 0.22) among them

while Tl_9CeTe_6 had the minimum (0.04 - 0.08), comparable to those of the late compound of the series (Tl_9HoTe_6).

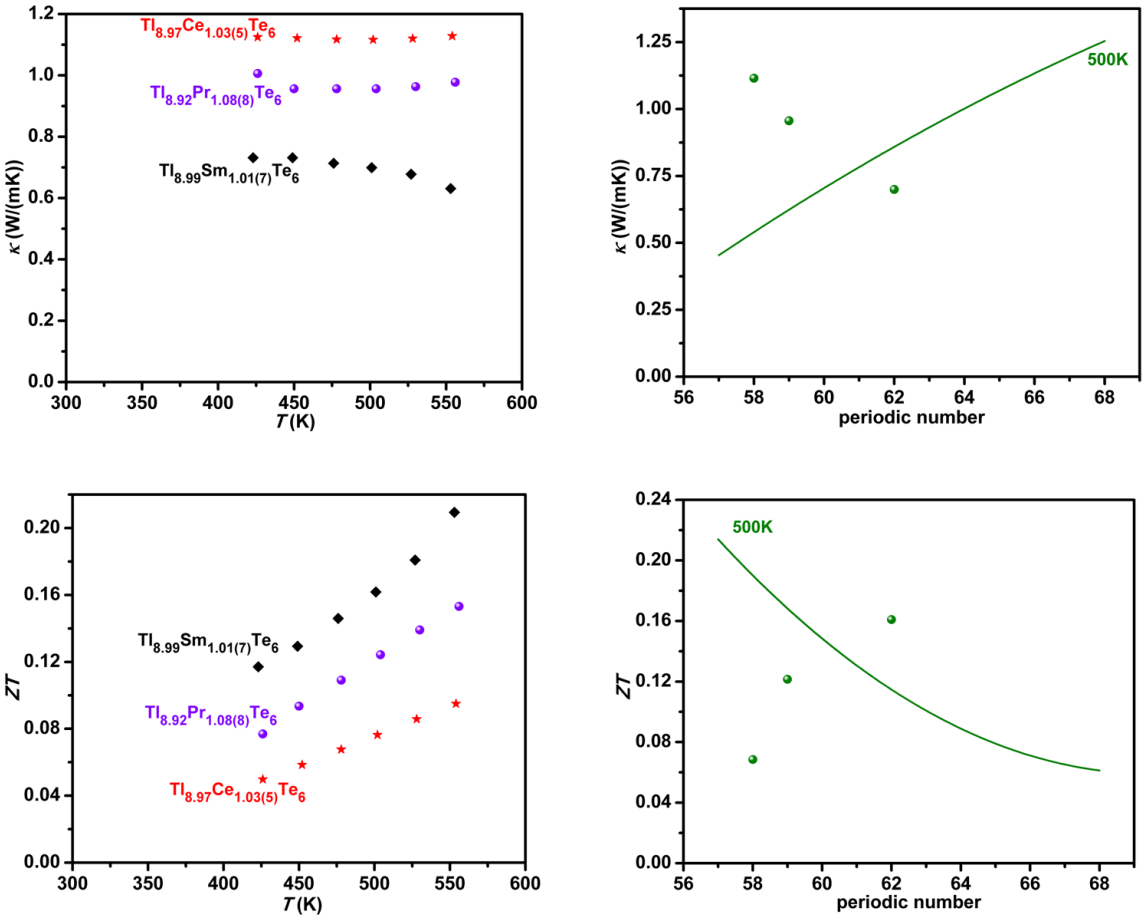

Figure 4.13: Plots of κ vs. T (top left), ZT vs. T (bottom left); plots of anomalous κ (top right) and ZT (bottom right) vs. periodic number for Tl_9LnTe_6, Ln = Ce, Pr and Sm

On the other hand, as T increases

- S increases, indicating that increasing T was more important, and n did not increase within the measurement temperature range as $S \propto T\, n^{-2/3}$.
- σ decreases due to increasing S ($S \propto /\sigma$) or due to decrease in carrier mobility as a result of increasing lattice vibration

- κ is generally independent with respect to *T*.
  - $Tl_{0.25}Ce_{0.75}Te_6$, $Tl_{9.75}Pr_{0.25}Te_6$, $Tl_{0.25}Pr_{0.75}Te_6$, $Tl_{8.98}Pr_{1.08(8)}Te_6$, $Tl_{9.5}Sm_{0.5}Te_6$ and $Tl_{9.18}Sm_{0.82(8)}Te_6$ behaved like the lanthanum compound
  - $Tl_{0.75}Ce_{0.25}Te_6$, $Tl_{8.88}Ce_{1.12(6)}Te_6$ and $Tl_{9.5}Pr_{0.5}Te_6$ behaved like $Tl_{9.25}Ln_{0.25}Te_6$, Ln = Nd, Dy and Er, and $Tl_{9.47}Er_{0.53(6)}Te_6$
  - $Tl_{9.5}Ce_{0.5}Te_6$, $Tl_{8.97}Ce_{1.03(5)}Te_6$, $Tl_{9.75}Sm_{0.25}Te_6$ and $Tl_{8.99}Sm_{1.01(7)}Te_6$ behaved like $Tl_{8.98}Nd_{1.02(6)}Te_6$, $Tl_{9.28}Gd_{0.72(8)}Te_6$, $Tl_{9.5}Dy_{0.5}Te_6$ and $Tl_{8.95}Er_{0.95(5)}Te_6$.
- *ZT* increases with increasing *T* like for typical thermoelctrics

4.4 Conclusion

The physical properties of the $Tl_{10-x}Ln_xTe_6$ compounds synthesized in this study were measured and it was observed that as *x* increases, *S* increases, and σ and κ decrease, except for the Gd and Er phases. For $Tl_{10-x}Ln_xTe_6$, $x \approx 1$ across the Ln series, *S* decreases while σ and κ increase across the series. However, $Tl_{8.97}Ce_{1.03(5)}Te_6$, $Tl_{8.92}Pr_{1.08(8)}Te_6$ and $Tl_{8.99}Sm_{1.01(7)}Te_6$ showed deviations from the decreasing trend for *S* and increasing trends for σ and κ. One possible reason for that could be the discontinuity in the band gap trend of those compounds with respect to the other Tl_9LnTe_6 compounds across the series. We postulate this scenario based on the discontinuity in the band gap trend of the Ln_2Q_3 compounds (*Q* = O, S and Se): La_2Q_3 with highest band gap, Ce_2Q_3 with smallest band gap due to presence of Ce^{4+} with Sm_2Q_3 having band gap off the trend with respect to the rest of the compounds. Therefore, as indicated by the unit cell volume, the possible presence of Ce^{4+} in the structure of $Tl_{8.97}Ce_{1.03(5)}Te_6$ compound could be the reason for the deviation in the properties. The anomalous properties of $Tl_{8.92}Pr_{1.08(8)}Te_6$ compound is due to the presence of more than 6.25 % of Pr, as indicated by its EDX data and higher unit cell volume.

Overall, the dimensionless figure of merit, *ZT* increases as *x* increases for $Tl_{10-x}Ln_xTe_6$ and decreases across the series for $Tl_{10-x}Ln_xTe_6$, $x \approx 1$. The best *ZT* values (~ 0.22 at about 550 K) on cold pressed pellets were achieved for the stoichiometric compounds, Tl_9LnTe_6 with Ln = La, Nd and Sm.

The effect of hot pressing on the thermoelectric properties of the best compound of this series, Tl_9LaTe_6, was studied. There was not much difference in the Seebeck coefficient data of the hot pressed sample compared to the sintered sample; nevertheless, both the electrical and thermal conductivity values increased as expected. However, the increase was small: at 500 K, σ of the hot-pressed sample was 247/(Ωcm), while that of the cold-pressed sintered sample was 137/(Ωcm), and κ of the hot-pressed pellet was 0.51 W/(mK) compared to the sintered pellet, which was 0.45 W/(mK). The dimensionless figure of merit was improved from 0.22 at 555 K for the sintered pellet to 0.32 at 555 K for the hot-pressed pellet, an improvement factor of only 1.5.

5 MAGNETIC PROPETIES OF $Tl_{10-x}Ln_xTe_6$, x ≈ 1, Ln = Ce, Pr, Sm and Tb

From the Tl_9LnTe_6 series, Tl_9CeTe_6, Tl_9PrTe_6 and Tl_9SmTe_6 compounds deviated from the normal trend discussed in *section 4.3.3*. The anomalous behaviour of rare earth compounds, especially those of cerium and samarium compounds, with respect to the rest of the compounds from the f-block series has been observed previously.[139, 151-155] Generally, rare earths exhibit similar physical properties unless the 4f-electrons are directly involved in the 5d - 6s conduction state.[119]

The off trend unit cell volumes and thermoelectric properties of the above mentioned compounds led us to their magnetic properties measurements; however, that of Tl_9TbTe_6 was also analysed by this techniques as Tb may also exhibit variable oxidation states. In *Section 3.2*, the unit cell volume and in *Section 4.2.3*, the thermoelectric properties of latter have already been discussed and it was concluded that Tb obeys the expected trends as we move across the lanthanoid series. As a result, it was assumed that Tb exhibited the most common oxidation state of +3 in the 9-1-6 compound. The magnetic properties of the latter would be able to confirm the oxidation state of terbium in Tl_9TbTe_6 and serve as both a model for the rest of the series and a proof of the reliability of the magnetic data to conclude the oxidation state of Ce, Pr and Sm in their respective compounds.

The common and stable oxidation state of the f-block elements is +3; however, some elements like Ce, Pr, Sm and Tb may also exhibit variable oxidation states. Occurrence of variable oxidation states depends on the electronic configurations, divalent or tetravalent ions are obtained if in so doing the ions achieve a more stable electronic configuration like f^0, f^7 (half filled shell), f^{14} (completely filled shell).[118] *Table 5.1* shows the possibilities for cerium and terbium with their respective configurations.

Table 5.1[118]: Electronic configuration of Ce^{3+}, Ce^{4+}, Tb^{3+} and Tb^{4+}

Name	Ions	Electronic configuration	Name	Ions	Electronic configuration
Cerium	Ce^{3+}	[Xe] $4f^1$	Terbium	Tb^{3+}	[Xe] $4f^8$
	Ce^{4+}	[Xe]		Tb^{4+}	[Xe] $4f^7$

However, Pr^{4+} and Sm^{2+} do not have the more stable half filled or completely filled f-shell (*Table 5.2*), yet they exist in some compounds like PrO_2, SmO, SmF_2. This implies that there might be other thermodynamic and kinetic factor that governs the stability of the ions.[118]

Table 5.2[118]: Electronic configuration of Pr^{3+}, Pr^{4+}, Sm^{2+} and Sm^{3+}

Name	Ions	Electronic configuration	Name	Ions	Electronic configuration
Praseodymium	Pr^{3+}	[Xe] $4f^2$	Samarium	Sm^{3+}	[Xe] $4f^5$
	Pr^{4+}	[Xe] $4f^1$		Sm^{2+}	[Xe] $4f^6$

Therefore, the possibility of having mixed valent ions is more feasible for $Tl_{8.97}Ce_{1.03(5)}Te_6$ as Ce^{4+} has a more stable configuration with respect to Pr^{4+} and Sm^{2+}.[92, 118] Mixed valent cerium compounds are quite common; some examples are $CeSn_3$, Ce_2Sn_5, $CeSn_7$.[124] Ce_2Se_3 is also thought to have mixed-valent cerium based on its band gap with respect to the rest of the Ln_2Se_3 series (discussed in *Section 4.3*). Ternary systems like $CeNi_5Sn$,[125] $CeFe_4Sb_{12}$[126] and $Ce_3Pt_3Sb_4$[127] were also reported to be mixed valent compounds.

5.1 Magnetic nature of $Tl_{10-x}Ln_xTe_6$, Ln = Ce, Pr, Sm and Tb, $x \approx 1$

As mentioned earlier in *Section 2.3.3*, all the Ln^{3+} ions contain unpaired electrons and are paramagnetic except Y^{3+}, La^{3+} and Lu^{3+}.[92] The magnetic nature of the lanthanoid compounds can be deduced from the plots of magnetic susceptibility, χ vs. *T*, as mentioned in *Section 2.3.3.1*, by applying a Curie-Weiss or Modified Curie-Weiss fit.

M of Tl_9CeTe_6 and Tl_9TbTe_6 was measured as a function of *H*, at 2 K and as a function of *T* in a magnetic field of 100 Oe, samples of Tl_9SmTe_6 and Tl_9PrTe_6 were measured at 2 K and 1000 Oe. The plots of *M* versus *H* for the four compounds subjected to this measurement are shown in *Figure 5.1*. χ at various temperatures were calculated from the *M* at the fixed *H*, ($\chi = M/H$) to get the plot of χ-*T* (*Figure 5.2*).

Based on the shape of the plot of χ-T, one can determine the nature of magnetism exhibited by the compound as discussed in *Section 2.3.3*. According to *Figure 5.2*, all the compounds are paramagnetic as expected.[92]

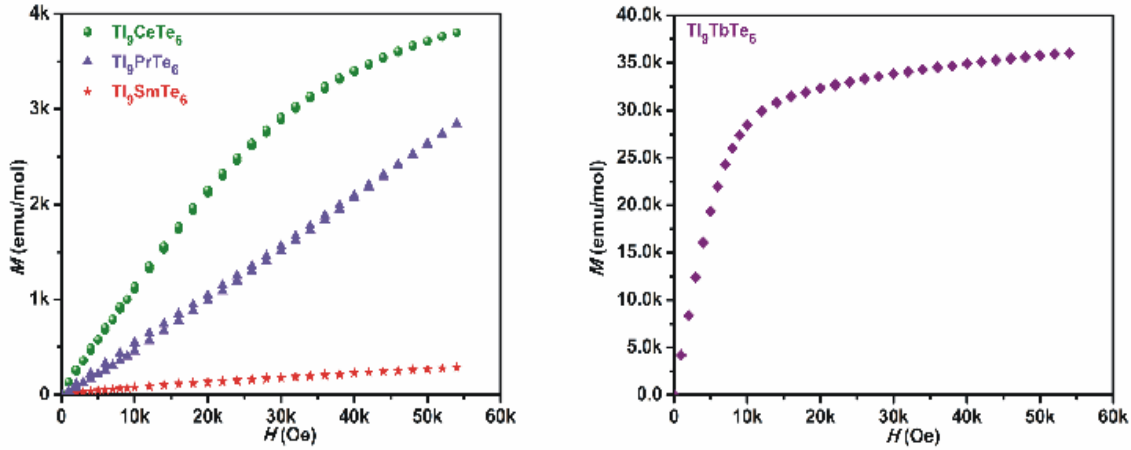

Figure 5.1: Plots of *M*-*H* at 2 K for Tl_9LnTe_6, Ln = Ce, Sm, Pr and Tb

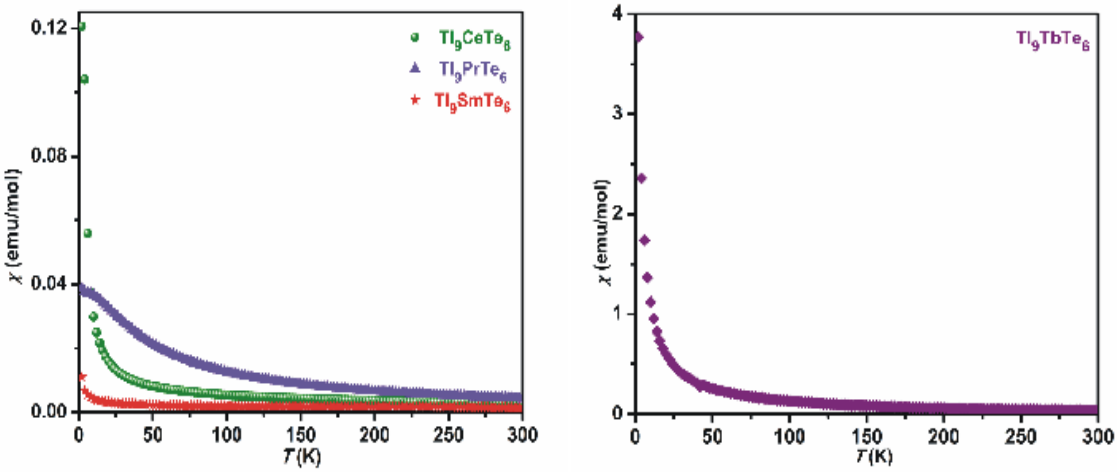

Figure 5.2: Plots of χ-T of Tl_9LnTe_6, Ln= Ce, Pr, Sm and Tb

5.2 Oxidation state of Tb in Tl_9TbTe_6

The plot of χ versus *T* reveals that the compound is paramagnetic and there is no ordering at any temperature. This data was used to obtain a plot of/χ versus *T* to be able to apply the Curie-Weiss Law[29, 118, 156] as follows.

$$\chi = \frac{C}{T - \theta} \tag{5.1}$$

Where, χ = magnetic susceptibility

T = temperature

C = Curie constant

θ = Weiss Constant

Hence,

$$\frac{1}{\chi} = \frac{T}{C} - \frac{\theta}{C} \tag{5.2}$$

A plot of/χ vs. *T* would give

- /*C* = slope, hence, *C* =/slope
- θ/*C* = intercept, θ = intercept/slope
- μ_{eff} as per the *Equation 5.3*[156, 157]

$$\mu_{\text{eff}} = 2.83\sqrt{C} \tag{5.3}$$

Figure 5.3 shows the plot of/χ versus *T* for Tl_9TbTe_6 with the Curie-Weiss fit and the experimental and theoretical μ_{eff}.

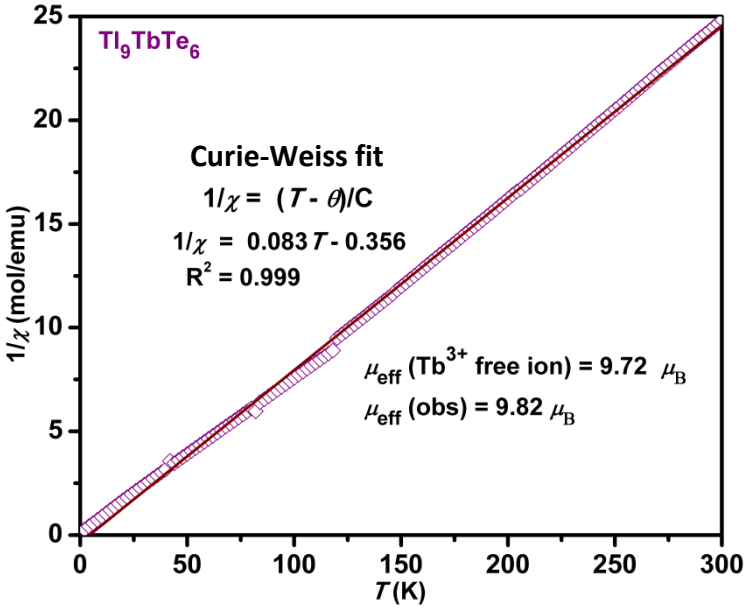

Figure 5.3: Plot of/χ vs. *T* for Tl_9TbTe_6

Since the theoretical μ_{eff} for a free Tb^{3+} ion is 9.72 μ_B[92, 118] from the *Equation 2.19*, the expected range is 9.5 μ_B - 9.8 μ_B.[158] The observed μ_{eff} of 9.82 μ_B in Tl_9TbTe_6 is very close to the theoretical μ_{eff} and to those observed in $Tb(phen)_2(NO_3)_3$ (9.81 μ_B)[118] and $Tb_6Zn_{1.46}Sb_{14}$ (10.0 μ_B)[157]. It could therefore be safely concluded that Tb was indeed in the oxidation state +3 in Tl_9TbTe_6.

5.3 Oxidation states of Ce and Pr in Tl_9CeTe_6 and Tl_9PrTe_6

Unlike in case of Tl_9TbTe_6, where the Curie-Weiss fit worked out perfectly, the magnetic data of Tl_9CeTe_6 and Tl_9PrTe_6 were processed differently: the/χ versus *T* plots were fitted to the Modified Curie-Weiss law (MCW)[159] as per *Equation (5.4)*.

$$\chi = \chi^*_{TIP} + \frac{C^*}{T - \theta} \qquad (5.4)$$

Where χ^*_{TIP} = the temperature-independent susceptibility

C^* = Curie constant and θ = Weiss constant

χ^*_{TIP} includes the diamagnetic core contribution, the Pauli paramagnetism and the Van Vleck correction.[160-162] Similar fits were done for $PrCr_2Si_2C$[163] and many cerium containing compounds like $CeNiBi_2$[164], Ce_2Ni_2Cd[161] and $CeRuGe_3$,[165] however, the latter had an anti-ferromagnetic phase transition at 6 K. Similarly, $CeRhIn_5$ experienced an anti-ferromagnetic transition at 3.8 K, unlike the others of that family, $CeCoIn_5$ and $CeIrRn_5$.[166]

Figure 5.4 shows the plots of/χ vs. *T* for the Tl_9CeTe_6 and Tl_9PrTe_6 compounds, the solid lines show the MCW fit. The temperature range considered for the fits were from 100 K to 300 K for Tl_9CeTe_6 and 75 K to 300 K for Tl_9PrTe_6, as below the 100 K and 25 K respectively, Tl_9CeTe_6 and Tl_9PrTe_6 deviate from the MCW behaviour. This deviation could be attributed to a crystalline electric-field (CEF) effect on the ground state.[164] *Table 5.3* shows the parameters of the MCW and the μ_{eff} values.

Table 5.3: Comparison of experimental and calculated μ_{eff}/μ_B for Tl_9LnTe_6, Ln = Ce and Pr

	C*	θ	χ^*_{TIP}	μ_{eff} (expt.)/ μ_B	μ_{eff} (free ion)/ μ_B	μ_{eff}/μ_B Expected range
Tl_9CeTe_6	0.546	-31.317	0.00128	2.09	2.46[92, 118]	2.3 – 2.5[158]
Tl_9PrTe_6	1.316	-0.913	0	3.25	3.48[92, 118]	3.4 – 3.6[158]

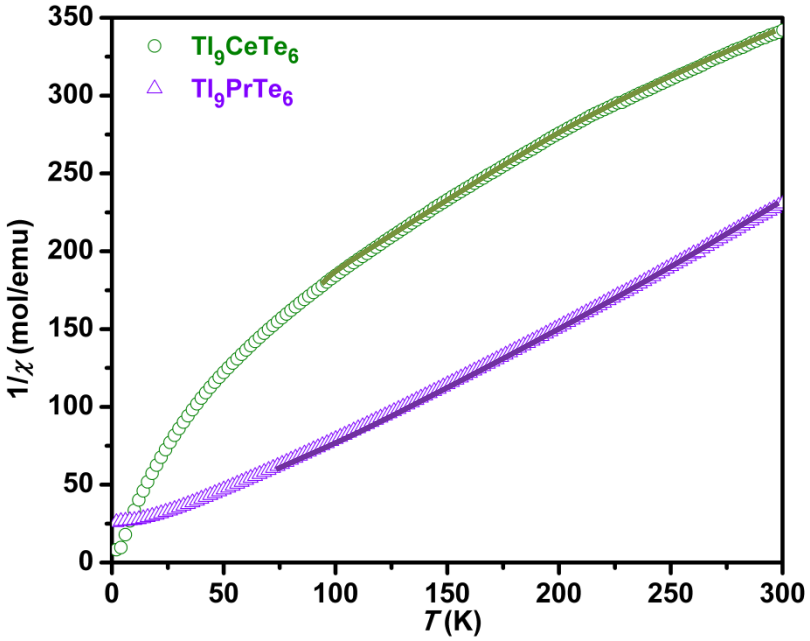

Figure 5.4: Plot of/χ vs. *T* for Tl_9LnTe_6, Ln= Ce and Pr

The measured μ_{eff} = 2.09 of Ce is lower than the expected range for Ce^{3+} (2.4 μ_B - 2.5μ_B)[158]. Therefore, it is postulated that there might be indeed some mixed valent ion of Ce^{3+} (major ions) and Ce^{4+} (minor ions) in Tl_9CeTe_6 which justifies the smaller unit cell volume. Many other cerium compounds exhibited μ_{eff} not close to the expected range like Ce_2CoSn_2[160] and $CeNiBi_2$ which gave a μ_{eff} of 2.89 μ_B and 2.83 μ_B respectively which is higher than the expected range most probably due to the localised magnetic moments of Ce ions in the compounds.[164] CeIrGe[162], $Ce_3Ru_4Ge_{13}$ and CeRuGe3[165] exhibited μ_{eff} of 0.27 μ_B, 1.06 μ_B and 1.23 μ_B respectively, due to presence of Ce^{4+} as minor ions in the system.

The μ_{eff} of Tl_9PrTe_6 seems to be within the expected range, hence the oxidation state of praseodymium in the system is assumed to be +3 just like that of Tb. Therefore, the higher volume than expected from *Figure 3.10* is most probably due to more Pr in the structure. On the contrary, $PrCr_2Si_2C$[163] and $PrVO_3$[167] exhibited a measured μ_{eff} of 4.4 and 4.0 μ_B respectively and yet they were considered to have only Pr^{3+} in the systems.

Since, the χ^*_{TIP} for Tl_9PrTe_6 is 0 according to the Modified Curie-Weiss fit, the μ_{eff} of the latter can also be calculated by applying Curie-Weiss law from fit from 75 K to 300 K. This resulted in a Curie-Weiss fit of/χ = 0.749 *T*+ 3.059 with R^2 of 0.999 and μ_{eff} of 3.27 μ_B. The magnetic data of $YbRh_2Pb$ was treated by a similar approach.[168]

5.4 Inconclusive oxidation state of Sm in Tl_9SmTe_6

Magnetic data for the Tl_9SmTe_6 compound was measured in a similar manner as for the Ce, Pr and Tb compounds using the same SQUID magnetometers; *Figure 5.5* shows the plot of/χ vs. *T*. Unlike the magnetic data of Tl_9TbTe_6, which fit to the Curie-Weiss Law, and the data for Tl_9CeTe_6 and Tl_9PrTe_6, which fit to the Modified Curie-Weiss Law, neither the Curie-Weiss nor the Modified Curie-Weiss Law were applicable for Tl_9SmTe_6. Similar observations were made for $Sm_6Zn_{1.38}Sb_{14.10}$, where the plot of/χ vs. *T* was distinctively non-linear. This implies that the effective magnetic moment from the 4f electrons depends on temperature as the ^6H ground term of Sm^{3+} gets split due to spin-orbit coupling. This is typical for Sm^{3+} containing compounds.[157] Hence, μ_{eff} of Sm in Tl_9SmTe_6 was not determined. This is similar to the cases of $LaCr_2Si_2C$ and $CeCr_2Si_2C$, (compounds containing Ln elements), which also exhibited strong deviations from the Curie-Weiss Law, unlike another member of the family, $PrCr_2Si_2C$.[163]

Therefore, it is quite common for compounds containing rare earth elements to exhibit unusual behaviour; hence, one can expect some exceptions from the normal trends of the rest of the lanthanoid series. Therefore, anomalous thermoelectric properties of Tl_9LnTe_6, Ln = Ce, Pr and Sm, with respect to the rest of the lanthanoid series can be explained and understood.

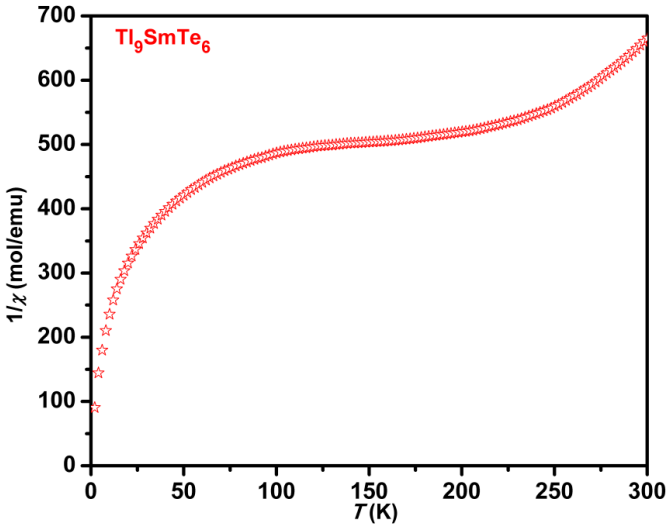

Figure 5.5: Plot of/χ vs. *T* for Tl_9SmTe_6

5.5 Conclusion

Magnetic properties of those four compounds (Tl_9LnTe_6, Ln = Ce, Pr, Sm and Tb) were studied. They were all found to be paramagnetic, as expected due to the presence of unpaired electrons. Based on the observed magnetic moment data, Tl_9TbTe_6 (9.82 μ_B) and Tl_9PrTe_6 (3.25 μ_B) could be safely concluded to have only M^{3+} present. On the contrary, Tl_9CeTe_6 exhibited a lower magnetic moment of 2.09 μ_B compared to the theoretical magnetic moment of 2.54 μ_B. Such an observation is common in cerium compounds due to presence of some Ce^{4+} in the structure. The magnetic data of Tl_9SmTe_6 was inconclusive, as the plot of/χ vs. *T* deviated significantly from the Curie-Weiss plot.

6 CONCLUSION

Thermoelectrics are one of the potential solutions to the increasing global energy demand. The motivation behind the research about thermoelectrics is to understand better the relationship between the transport properties and structure of thermoelectric materials. Such study helps to tune the important parameters (carrier concentrations, disordered arrangement of atoms in the structure etc. that would affect Seebeck coefficient, electrical and thermal conductivity values of the material) involved in the conversion process. By doing so, an efficient thermoelectric material could be discovered one day.

Conversion of heat loss from industries to electrical energy could be useful in many various ways, for example, powering a house like in Iceland. Similarly, if the electrical energy generated from the heat loss from the exhaust is used to power the accessories or even propel the engine, the fuel consumption will decline. This is the reason why automotive industry is also very interested in thermoelectrics and collaborates in relevant research. The General Motors of Canada collaborated in the research carried out in this thesis.

The motivation of this particular research is to contribute scientific information about the structure and transport properties of thallium lanthanoid tellurides, $Tl_{10-x}Ln_xTe_6$, to the field of thermoelectricity. $Tl_{10-x}Ln_xTe_6$ compounds are thallium based semiconductors. Thallium based semiconductors are thermoelectric materials with quite low thermal conductivity which is one of the criteria for a good thermoelectric material. Among the thallium based semiconductors, Tl_9BiTe_6 is one of the most promising materials with a *ZT* value of 1.2 at 580 K on a zone refined pellet; hence, it is the main focus point of this research. In this thesis, improvement of the thermoelectric properties of materials of this family is attempted.

Tl_9BiTe_6 has a body centred tetragonal structure with space group, *I4/mcm*, and random distribution of Tl/Bi at the 4c site. In the thallium lanthanoid tellurides, Ln and Tl occupy the *4c* site randomly. The random distribution of Ln/Tl at the *4c* site results in two phenomena: the phonon scattering due to random distribution and mass fluctuation

due to difference in atomic number of Ln and Tl. Consequently, the thermal conductivity of the $Tl_{10-x}Ln_xTe_6$ is expected to be lower than that of Tl_9BiTe_6; hence, the *ZT* value of the $Tl_{10-x}Ln_xTe_6$ series is expected to be better than that of Tl_9BiTe_6. This study revealed that the series $Tl_{10-x}Ln_xTe_6$ could not out perform Tl_9BiTe_6 despite low thermal conductivity of the compounds synthesized in this study because of their low Seebeck coefficient values compared to the large Seebeck Coefficient value of Tl_9BiTe_6. The lower Seebeck Coefficient values of the compounds studied in this thesis are most probably due to shape of their DOS plots (smaller slope of the DOS plot at the Fermi level results in smaller Seebeck Coefficient value). The best *ZT* obtained in this study on cold-press was ~0.20 and on a hot- pressed pellet was ~0.32. However, the *ZT* of 1.2 was on a zone refined sample of Tl_9BiTe_6, therefore, future work could involve study of the thermoelectric properties of Tl_9LnTe_6, Ln = La, Nd, Sm on zone refined samples.

Overall, the results of this work can be interpreted in two ways:

a) For a given Ln, $Tl_{10-x}Ln_xTe_6$
   - *S* increases both with increasing *x* and *T*
   - σ decreases both with increasing *x* and *T*
   - κ is independent of *T* but decreases with increasing *x*
   - *ZT* increases both with increasing *x* and *T*

b) For Tl_9LnTe_6, across the lanthanoid series from La to Er
   - *S* decreases while σ and κ increase across the series
   - *ZT* decrease

Generally, the experimental data agree with the hypothesis involving the thermoelectric properties of the compounds, across the Ln series and within a particular Ln phase. However, Tl_9LnTe_6 with Ln = Ce, Pr and Sm gave contradictory results with respect to the rest of the series. We postulate the possibility of some percentage of Ce^{4+} in the Tl_9CeTe_6 based on its lower magnetic moment of 2.09 μ_{eff}/μ_B and it distinctively smaller unit cell volume of 1019(1) $Å^3$ with respect to that of Tl_9LaTe_6 (V > 1040 $Å^3$) . This possibility need to be confirmed by XANES future work. Moreover, further studies like TEM could be done on those compounds and the other two best samples of the

series, Tl_9LaTe_6 and Tl_9NdTe_6 in the future. TEM images will help to conclude whether or not nanodomains are present in those particular compounds, which could be responsible for the better *ZT* value with respect to the other compounds studied. Moreover, TEM will also reveal whether or not, grain boundaries which results in further phonon scattering, are present in the compounds of interest (Tl_9LaTe_6, Tl_9NdTe_6 and Tl_9SmTe_6).

PAPERS AND CONFERENCE PRESENTATIONS RELATED TO THIS WORK

Papers

S. Bangarigadu-Sanasy, C. R. Sankar, P. Schlender and H. Kleinke, P. Dube and J. Greedan, Magnetic properties of Tl_9LnTe_6, Ln = Ce, Pr, Tb and Sm (in prep.).

S. Bangarigadu-Sanasy, C. R. Sankar, A. Assoud, P. Schlender and H. Kleink, Thermoelectric properties of $Tl_{10-x}Ln_xTe_6$, Ln=Nd, Gd, Tb, Dy, Ho, Er; $0.25 \leq x \leq 1.32$, *J. Alloys Compd.* (accepted).

C. R. Sankar, S. Bangarigadu-Sanasy, A. Assoud and H. Kleinke, Structural and thermoelectric properties of $TlGdQ_2$ (Q = Se, Te) and Tl_9GdTe_6, *J. Electr. Mater.* (in press).

S. Bangarigadu-Sanasy, C. R. Sankar, A. Assoud and H. Kleinke, Crystal Structures and Thermoelectric Properties of the Series $Tl_{10-x}La_xTe_6$ with $0.2 \leq x \leq 1.15$, *Dalton Trans.* **2011**, 40, 862-867.

C. R. Sankar, S. Bangarigadu-Sanasy, H. Kleinke, Thermoelectric Properties of New Thallium Tellurides, *Mater. Res. Soc. Symp.* **2011**, 1309, 67 – 76.

C. R. Sankar, S. Bangarigadu-Sanasy, A. Assoud, H. Kleinke, Crystal structure and physical properties of Tl_4MQ_4 (M = Zr, Hf, Q = S, Se), *Inorg. Chem.* **2011**, 50, 245 - 249.

C. R. Sankar, S. Bangarigadu-Sanasy, A. Assoud, H. Kleinke, Syntheses, Crystal Structures and Thermoelectric Properties of two new Thallium Tellurides: Tl_4ZrTe_4 and Tl_4HfTe_4, *J. Mater. Chem.* **2010**, 20, 7485 - 7490.

Conference presentations

North American Solid State Chemistry Conference 2011

Oral presentation: '*Thermoelectric Properties of Thallium Lanthanoid Tellurides*',

S. Bangarigadu-Sanasy and H. Kleinke

Canada Research Chair Event 2010

Poster Presentation, '*Physical Properties of Tl-Based $Tl_{10}Te_6$ Thermoelectric Materials: La & Sn Doping*',

B. A. Kuropatwa, S. Bangarigadu-Sanasy and H. Kleinke

Guelph Waterloo Centre for Graduate Work in Chemistry and Biochemistry 2010

Poster Presentation, '*Thermoelectric properties of new thallium tellurides, $Tl_{10-x}La_xTe_6$*',

S. Bangarigadu - Sanasy, C. R. Sankar, H. Kleinke, J. R. Salvador and J. Yang

92nd Canadian Chemistry Conference and Exhibition 2009

Poster Presentation, '*Thermoelectric properties of new thallium tellurides, $Tl_{10-x}La_xTe_6$*',

S. Bangarigadu - Sanasy, C. R. Sankar, H. Kleinke, J. R. Salvador and J. Yang

APPENDICES

Table A.1: Atomic positions and equivalent isotropic displacement parameters of $Tl_{9.09}La_{0.91(5)}Te_6$ (Rietveld data) and $Tl_{8.96(3)}La_{1.04}Te_6$ (single crystal data)

atoms	Wyckoff site	$Tl_{9.09}La_{0.91(5)}Te_6$				$Tl_{8.96(3)}La_{1.04}Te_6$			
		x	*y*	*z*	U_{eq} (Å^2)	*x*	*y*	*z*	U_{eq} (Å^2)
M/Tl1	***4c***	0	0	0	0.011	0	0	0	0.0230(3)
Tl2	***16l***	0.1472(2)	*x* + ½	0.1671(3)	0.034(2)	0.14686(5)	*x* + ½	0.15978(5)	0.0403(1)
Te1	***4a***	0	0	¼	0.017(3)	0	0	¼	0.0266(4)
Te2	***8h***	0.3396(5)	*x* + ½	0	0.023(3)	0.33833(9)	*x* + ½	0	0.0222(2)

Table A.2: Lattice parameters and selected interatomic distances of $Tl_{9.09}La_{0.91(5)}Te_6$ and $Tl_{8.96(3)}La_{1.04}Te_6$

		$Tl_{9.09}La_{0.91(5)}Te_6$ (Rietveld data)	$Tl_{8.96(3)}La_{1.04}Te_6$ (single crystal data)
***a* (Å)**		8.917(3)	8.9220(4)
***c* (Å)**		13.115(4)	13.156(1)
***V* (Å^3)**		1042.8(9)	1047.2(1)
M1–Te1	2×	3.2787(9)	3.2890(3)
M1–Te2	4×	3.349(2)	3.3455(4)
Tl2–Te2		3.221(4)	3.202(1)
Tl2–Te2	2×	3.469(4)	3.4660(9)
Tl2–Te1	2×	3.600(2)	3.613(2)
Tl2–Tl2		3.714(5)	3.706(1)
Tl2–Tl2	2×	3.503(6)	3.536(1)
Tl2–Tl2		3.476(6)	3.523(1)
R		0.0496	
wR		0.0572	0.0766
R_F^2		0.1004	0.1814

Table A.3: Lattice parameters and selected interatomic distances of $Tl_{8.68}Nd_{1.32(6)}Te_6$ and $Tl_{9.26}Tb_{0.74(7)}Te_6$

		$Tl_{8.68}Nd_{1.32(6)}Te_6$	$Tl_{9.26}Tb_{0.74(7)}Te_6$
***a* (Å)**		8.8782(2)	8.896(5)
***c* (Å)**		13.0894(4)	12.835(8)
***V* (Å^3)**		1031.74(3)	1015.8(19)
M1–Te1 (Å)	2×	3.27236(9)	3.2088(20)
M1–Te2 (Å)	4×	3.331(2)	3.340(3)
Tl2–Te2 (Å)		3.210(5)	3.158(5)
Tl2–Te2 (Å)	2×	3.471(5)	3.413(5)
Tl2–Te1 (Å)	2×	3.581(2)	3.599(3)
Tl2–Tl2 (Å)		3.699(6)	3.702(6)
Tl2–Tl2 (Å)	2×	3.476(7)	3.520(8)
Tl2–Tl2 (Å)		3.448(8)	3.499(9)
R		0.0639	0.0622
wR		0.0622	0.0573
R_F^2		0.1118	0.0896

Table A.4: Lattice parameters and selected interatomic distances of $Tl_{9.52}Ho_{0.48(4)}Te_6$ and $Tl_{9.24}Ho_{0.76(8)}Te_6$

		$Tl_{9.52}Ho_{0.48(4)}Te_6$	$Tl_{9.24}Ho_{0.76(8)}Te_6$
***a* (Å)**		8.910(2)	8.897(5)
***c* (Å)**		12.701(3)	12.788(7)
***V* (Å^3)**		1008(7)	1012(2)
M1–Te1 (Å)	2×	3.1753(8)	3.197(2)
M1–Te2 (Å)	4×	3.346(2)	3.330(4)
Tl2–Te2 (Å)		3.165(4)	3.157(7)
Tl2–Te2 (Å)	2×	3.418(4)	3.457(8)
Tl2–Te1 (Å)	2×	3.591(2)	3.581(3)
Tl2–Tl2 (Å)		3.712(4)	3.712(8)
Tl2–Tl2 (Å)	2×	3.475(5)	3.46(1)
Tl2–Tl2 (Å)		3.448(6)	3.42(1)
R		0.0477	0.0637
wR		0.0461	0.0860
R_F^2		0.09242	0.0735

Table A.5: Atomic coordinates and equivalent isotropic displacement parameters of $Tl_{9.48}Gd_{0.52(5)}Te_6$ and $Tl_{9.32}Gd_{0.68(8)}Te_6$

atoms	Wyckoff site	$Tl_{9.48}Gd_{0.52(5)}Te_6$				$Tl_{9.32}Gd_{0.68(8)}Te_6$			
		x	*y*	*z*	U_{eq}	*x*	*y*	*z*	U_{eq}
Gd/Tl1	***4c***	0	0	0	0.027	0	0	0	0.018
Tl2	***16l***	0.1473(2)	*x* + ½	0.1604(4)	0.033(1)	0.1471(2)	*x* + ½	0.1604(5)	0.023(2)
Te1	***4a***	0	0	¼	0.045(3)	0	0	¼	0.040(4)
Te2	***8h***	0.3385(5)	*x* + ½	0	0.028(3)	0.3380(7)	*x* + ½	0	0.031(5)

TableA.6: Atomic coordinates and equivalent isotropic displacement parameters of $Tl_{9.0}Gd_{1.0(1)}Te_6$ and $Tl_{8.83}Gd_{1.17(5)}Te_6$

atoms	Wyckoff site	$Tl_{9.0}Gd_{1.0(1)}Te_6$				$Tl_{8.83}Gd_{1.17(5)}Te_6$			
		x	*y*	*z*	U_{eq}	*x*	*y*	*z*	U_{eq}
Gd/Tl1	***4c***	0	0	0	0.011	0	0	0	0.020
Tl2	***16l***	0.1473(3)	*x* + ½	0.1623(7)	0.028(3)	0.1475(2)	*x* + ½	0.1627(3)	0.048(1)
Te1	***4a***	0	0	¼	0.015(5)	0	0	¼	0.044(3)
Te2	***8h***	0.3370(9)	*x* + ½	0	0.032(6)	0.3382(5)	*x* + ½	0	0.051(3)

Table A.7: Atomic coordinates and equivalent isotropic displacement parameters of $Tl_{9.28}Tb_{0.74(7)}Te_6$ and $Tl_{9.01}Tb_{0.99(5)}Te_6$

atoms	Wyckoff site	$Tl_{9.28}Tb_{0.74(7)}Te_6$				$Tl_{9.01}Tb_{0.99(5)}Te_6$			
		x	*y*	*z*	U_{eq}	*x*	*y*	*z*	U_{eq}
Tb/Tl1	***4c***	0	0	0	0.010	0	0	0	0.012
Tl2	***16l***	0.1471(2)	*x* + ½	0.1583(4)	0.046(2)	0.1466(2)	*x* + ½	0.1611(3)	0.034(1)
Te1	***4a***	0	0	¼	0.034(4)	0	0	¼	0.028(3)
Te2	***8h***	0.3392(5)	*x* + ½	0	0.017(4)	0.3365(4)	*x* + ½	0	0.029(3)

Table A.8: Atomic coordinates and equivalent isotropic displacement parameters of $Tl_{9.52}Ho_{0.48(4)}Te_6$ and $Tl_{9.34}Ho_{0.76(8)}Te_6$

atoms	Wyckoff site	$Tl_{9.52}Ho_{0.48(4)}Te_6$				$Tl_{9.34}Ho_{0.76(8)}Te_6$			
		x	*y*	*z*	U_{eq}	*x*	*y*	*z*	U_{eq}
Tb/Tl1	***4c***	0	0	0	0.021	0	0	0	0.03
Tl2	***16l***	0.1473(2)	*x* + ½	0.1604(3)	0.030(1)	0.1475(3)	*x* + ½	0.1620(6)	0.033(3)
Te1	***4a***	0	0	¼	0.028(2)	0	0	¼	0.013(5)
Te2	***8h***	0.3395(5)	*x* + ½	0	0.028(3)	0.3369(8)	*x* + ½	0	0.030(6)

Table A.9: Atomic coordinates and equivalent isotropic displacement parameters of $Tl_{9.47}Er_{0.53(6)}Te_6$ and $Tl_{9.19}Er_{0.81(6)}Te_6$

atoms	Wyckoff site	$Tl_{9.78}Er_{0.53(6)}Te_6$				$Tl_{9.19}Er_{0.81(6)}Te_6$			
		x	*y*	*z*	U_{eq}	*x*	*y*	*z*	U_{eq}
Er/Tl1	***4c***	0	0	0	0.023	0	0	0	0.012
Tl2	***16l***	0.1472(2)	*x* + ½	0.1603(4)	0.040(1)	0.1480(2)	*x* + ½	0.1618(3)	0.037(2)
Te1	***4a***	0	0	¼	0.029(3)	0	0	¼	0.039(3)
Te2	***8h***	0.3395(5)	*x* + ½	0	0.039(3)	0.3385(5)	*x* + ½	0	0.038(3)

Table A.10: Atomic coordinates and equivalent isotropic displacement parameters of $Tl_{9.05}Er_{0.95(5)}Te_6$

atoms	Wyckoff site	$Tl_{9.05}Er_{0.95(5)}Te_6$			
		x	*y*	*z*	U_{eq}
Er/Tl1	***4c***	0	0	0	0.033
Tl2	***16l***	0.1475(2)	*x* + ½	0.1627(3)	0.041(1)
Te1	***4a***	0	0	¼	0.044(3)
Te2	***8h***	0.3380(5)	*x* + ½	0	0.048(3)

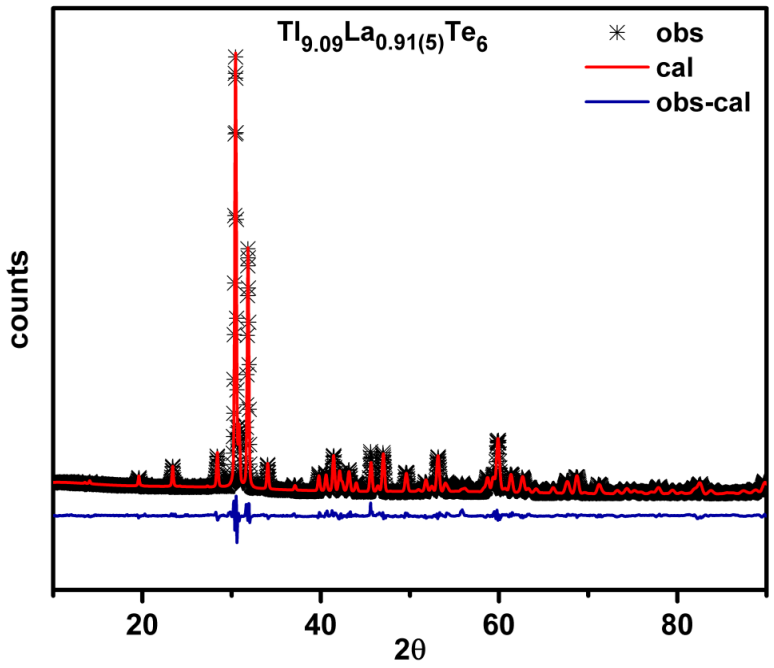

Figure A.1: Rietveld refinement of $Tl_{9.09}La_{0.91(5)}Te_6$

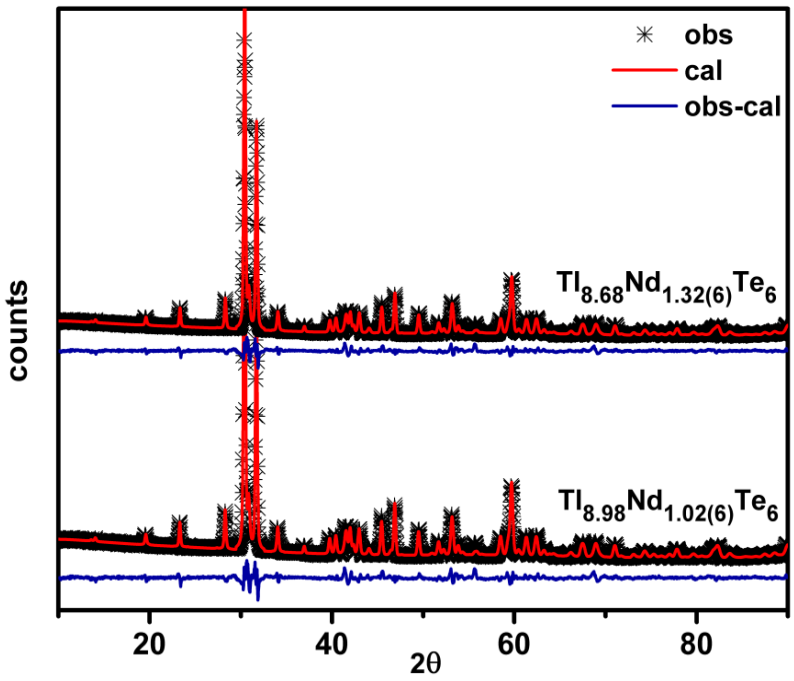

Figure A.2: Rietveld refinement of $Tl_{10-x}Nd_xTe_6$, $x \approx 1, 1.3$

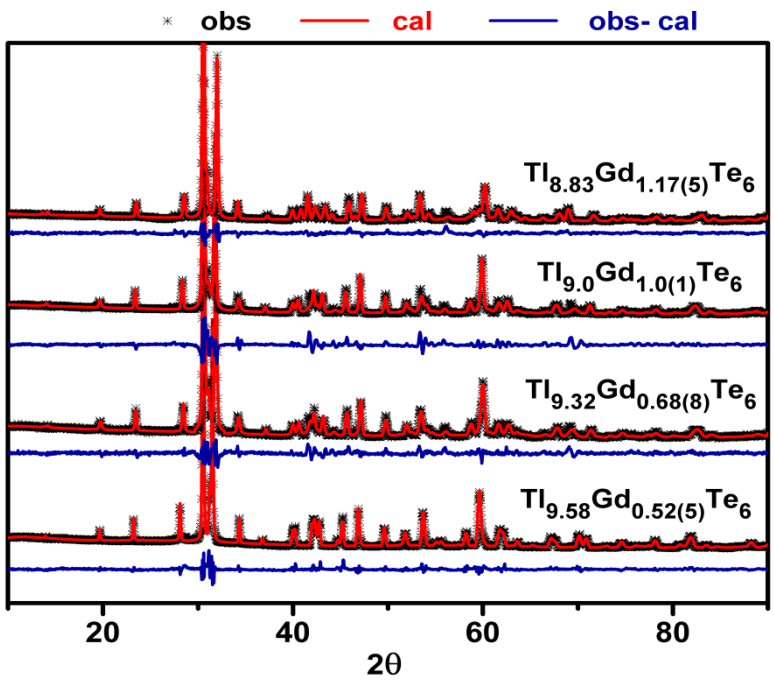

Figure A.3: Rietveld refinement of $Tl_{10-x}Gd_xTe_6$, $x \approx 0.52$, 0.68, 1.0 and 1.17

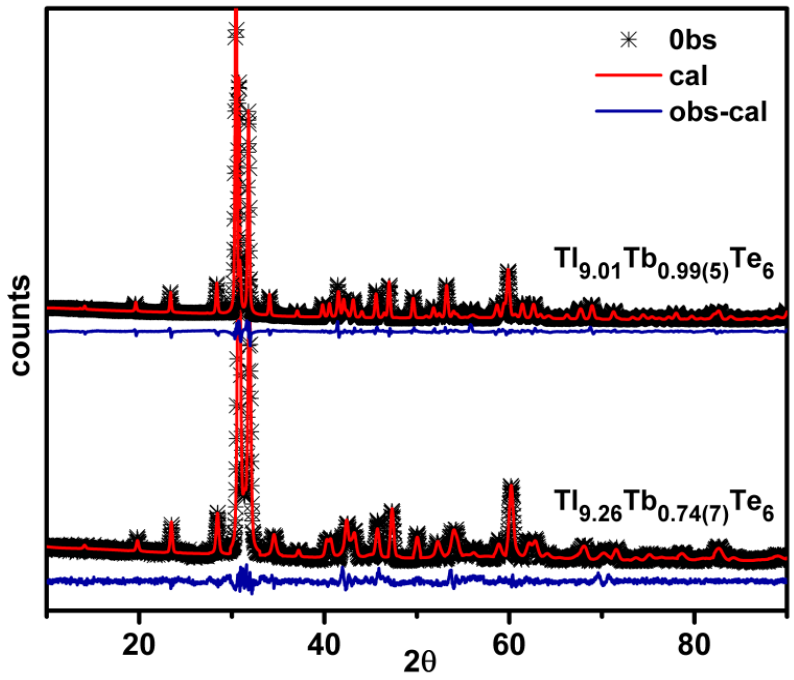

Figure A.4: Rietveld refinement of $Tl_{10-x}Tb_xTe_6$, $x \approx 0.74$ and 0.9

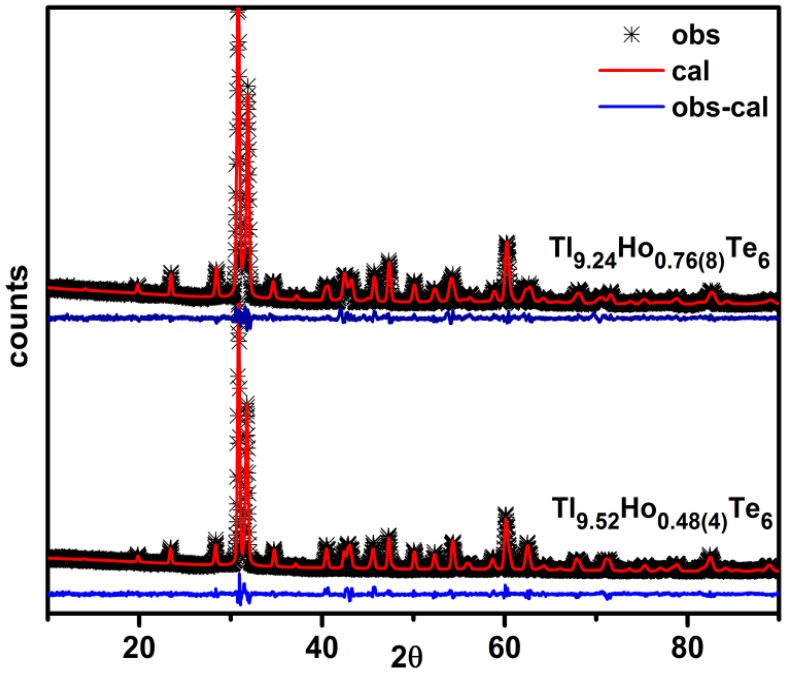

Figure A.5: Rietveld refinement of $Tl_{10-x}Ho_xTe_6$, $x \approx 0.48$ and 0.76

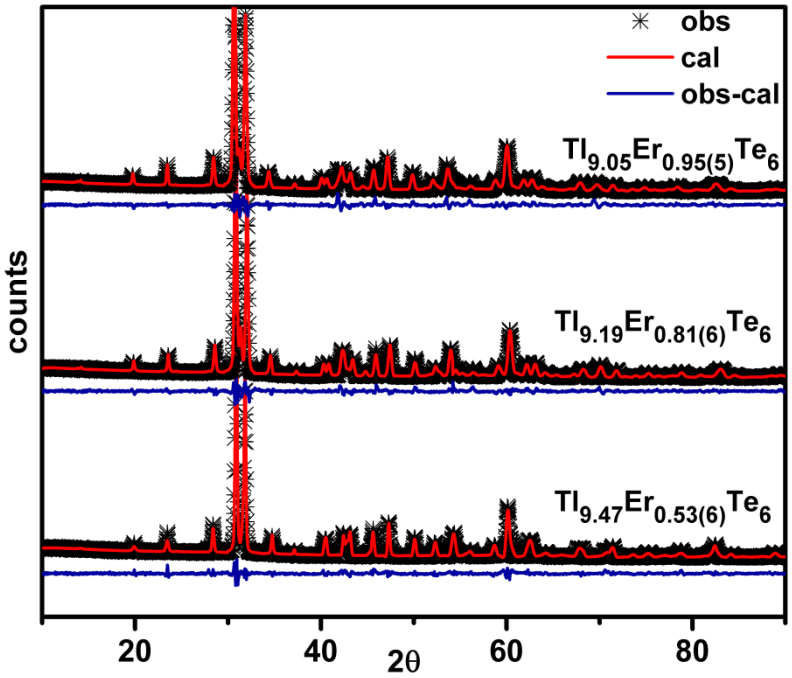

Figure A.6: Rietveld refinement of $Tl_{10-x}Er_xTe_6$, $x \approx 0.53$, 0.81 and 0.95

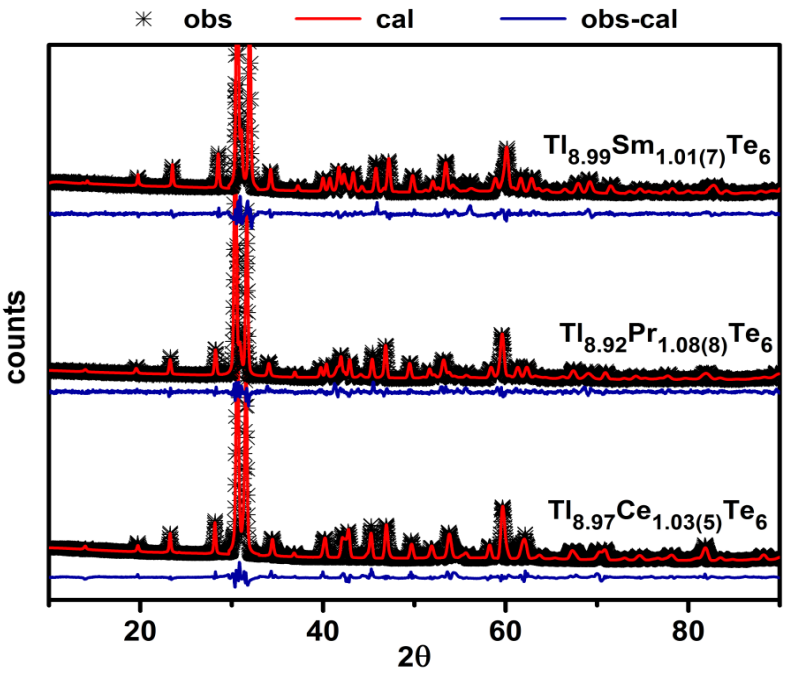

Figure A.7: Rietveld refinements of Tl_9LnTe_6, Ln = Ce, Pr, Sm

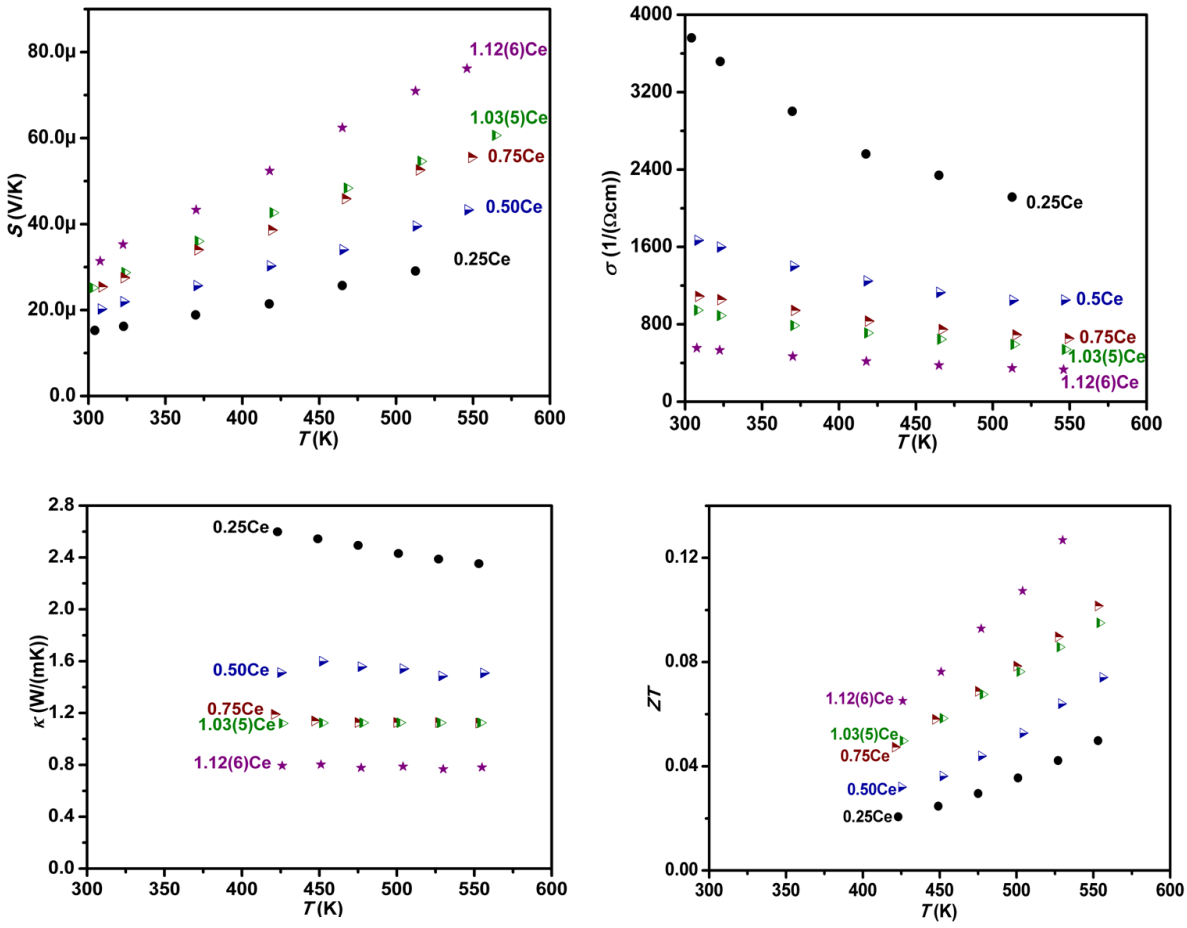

Figure A.8: Thermoelectric properties of $Tl_{10-x}Ce_xTe_6$, $0.25 \leq x \leq 1.12$

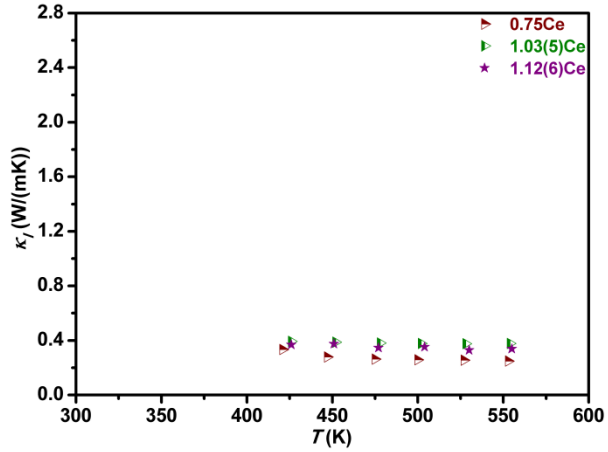

Figure A.9: Plot of κ_l vs. T of $Tl_{10-x}Ce_xTe_6$, x ~ 0.75, 1.03 and 1.12

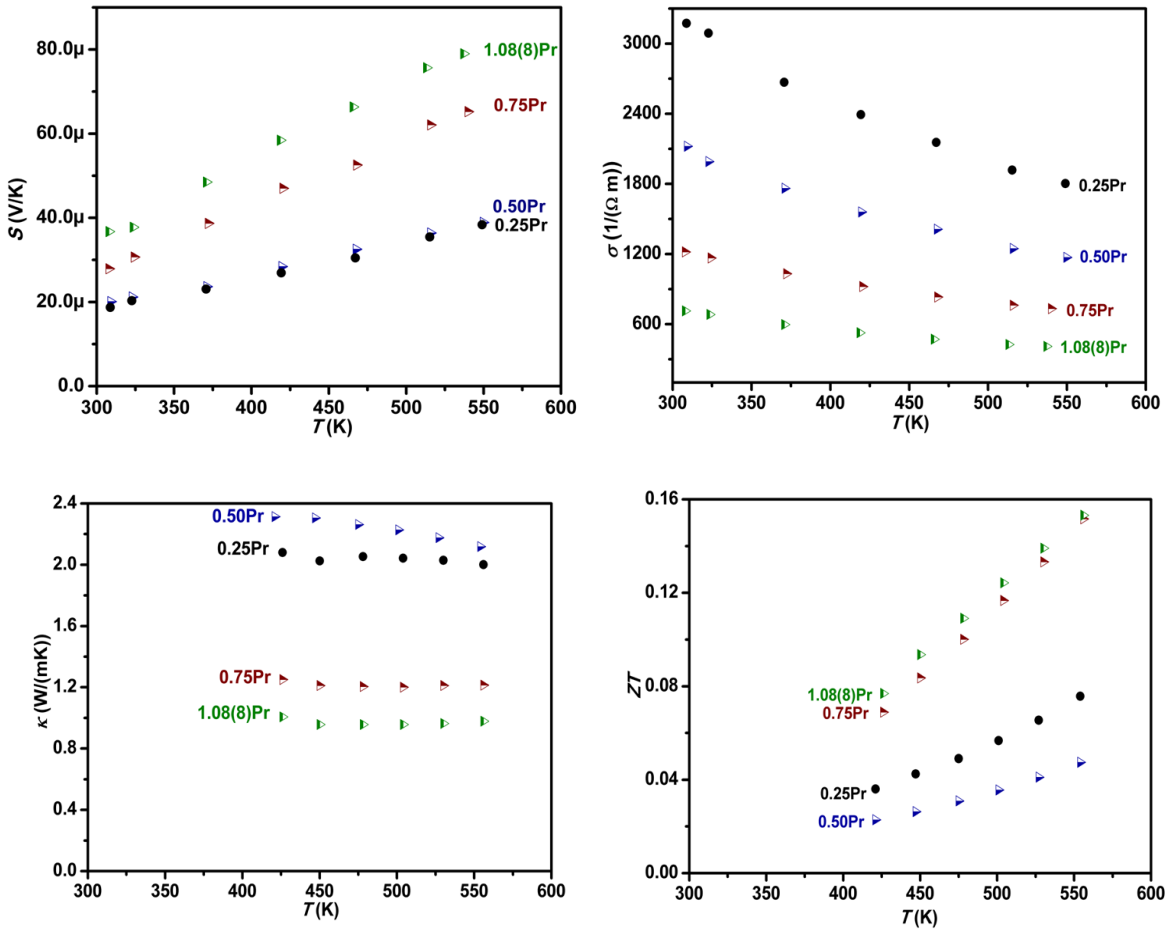

Figure A.10: Thermoelectric properties of $Tl_{10-x}Pr_xTe_6$, $0.25 \leq x \leq 1.08$

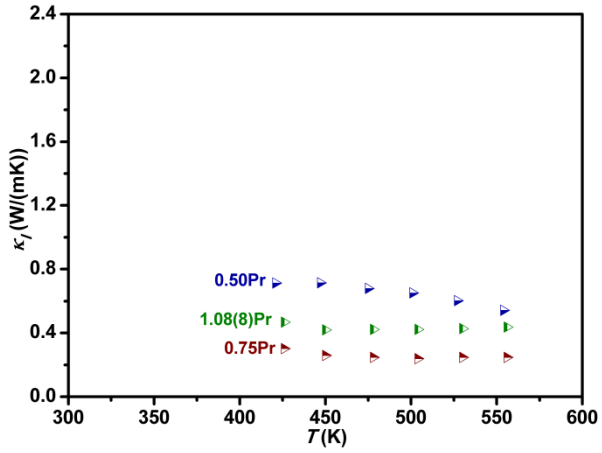

Figure A.11: Plot of κ_l vs. T of $Tl_{10-x}Pr_xTe_6$, x ~ 0.5, 0.75 and 1.08

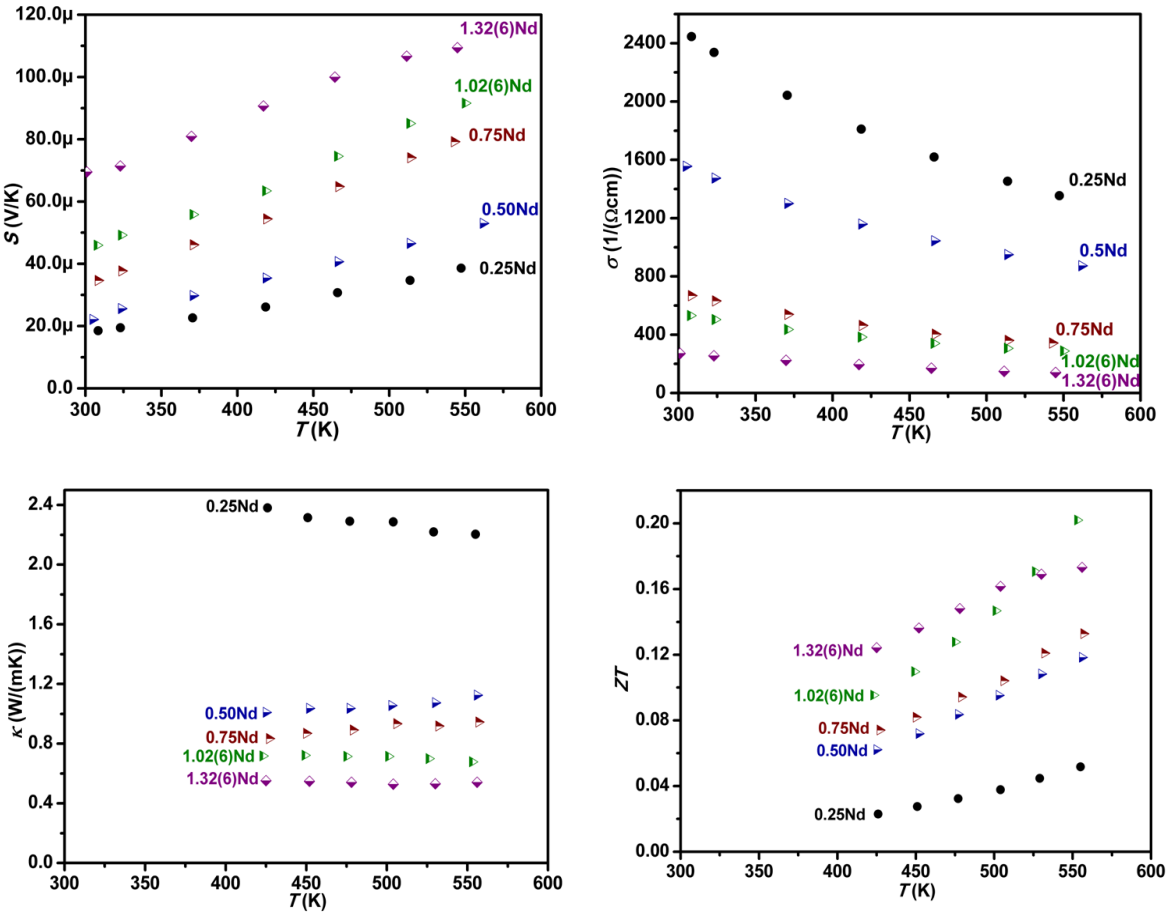

Figure A.12: Thermoelectric properties of $Tl_{10-x}Nd_xTe_6$, $0.25 \leq x \leq 1.32$

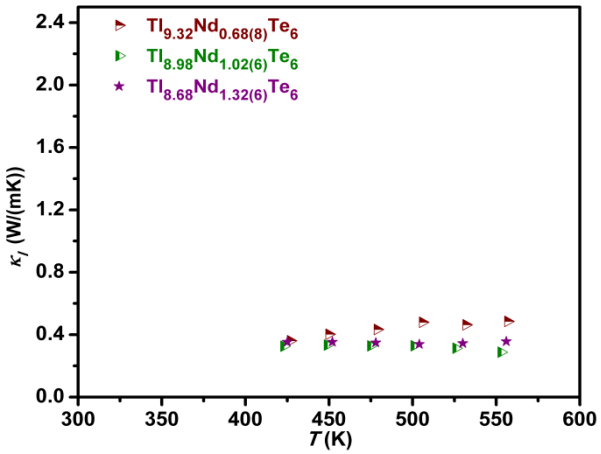

Figure A.13: Plot of κ_l vs. T of $Tl_{10-x}Nd_xTe_6$, $x \sim 0.68$, 1.02 and 1.32

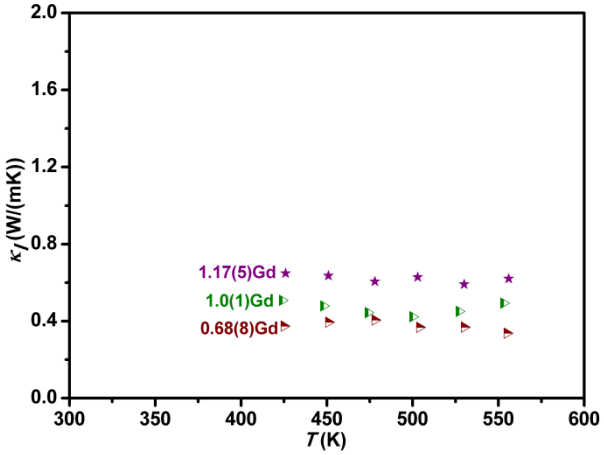

Figure A.14: Plot of κ_l vs. T of $Tl_{10-x}Gd_xTe_6$, x ~ 0.68, 1.01 and 1.17

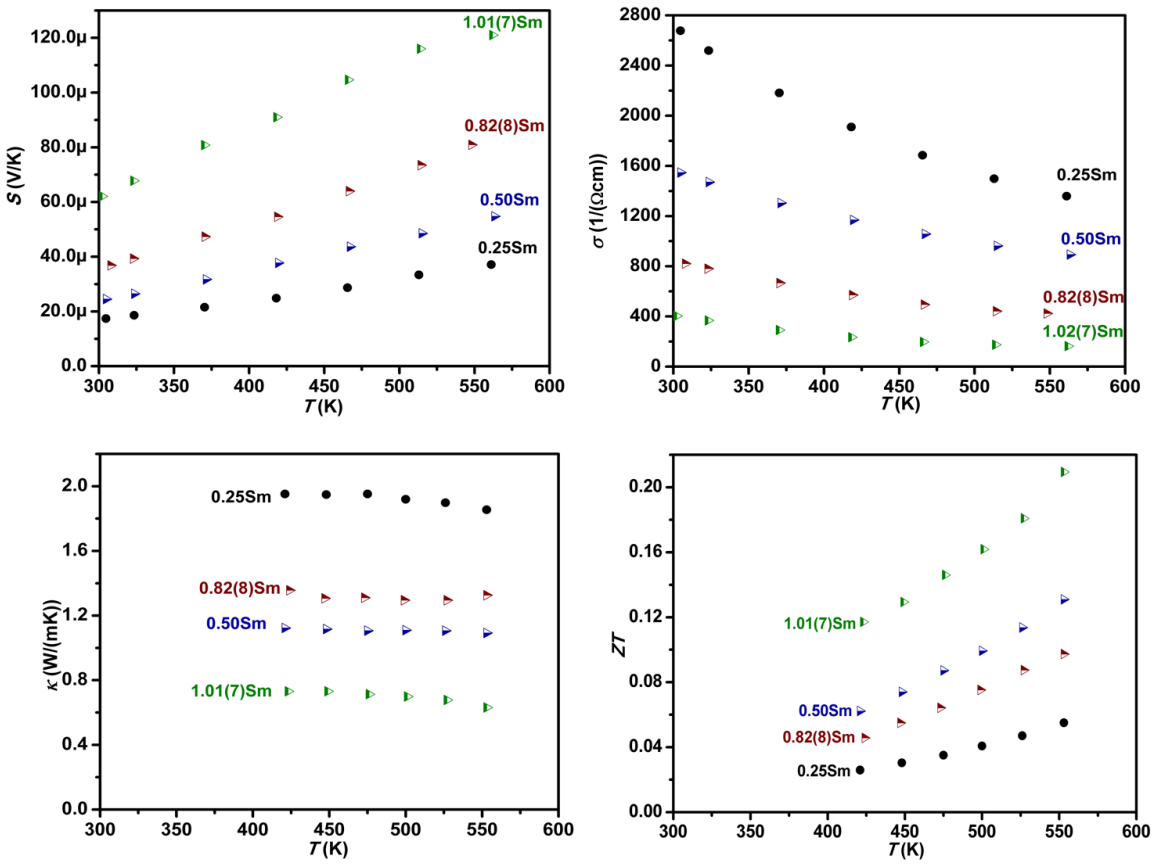

Figure A.15: Thermoelectric properties of $Tl_{10-x}Sm_xTe_6$, $0.25 \leq x \leq 1.01$

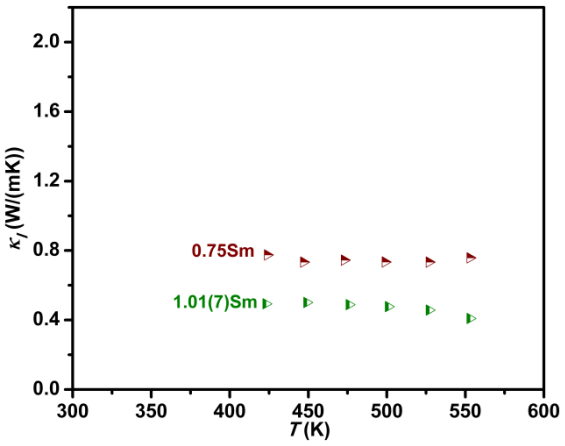

Figure A.16: Plot of κ_l vs. T of $Tl_{10-x}Sm_xTe_6$, $x \sim 0.75$ and 1.01

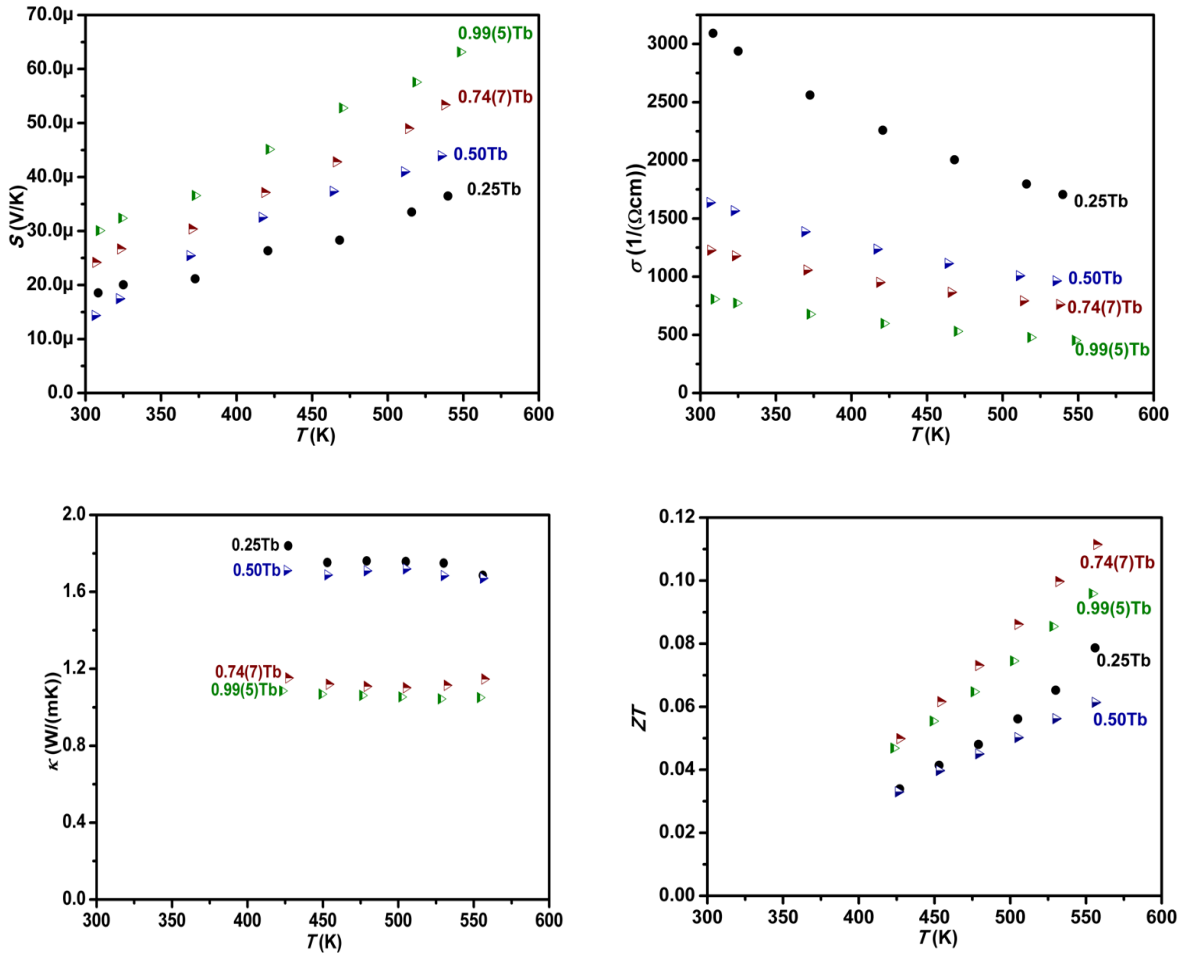

Figure A.17: Thermoelectric properties of $Tl_{10-x}Tb_xTe_6$, $0.25 \leq x \leq 0.99$

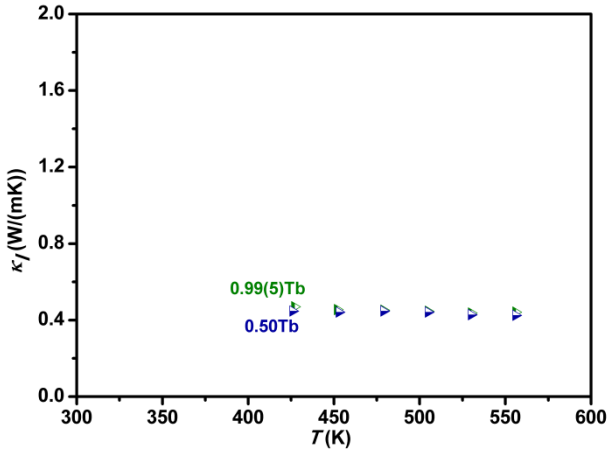

Figure A.18: Plot of κ_l vs. T of $Tl_{10-x}Tb_xTe_6$, $x \sim 0.5$ and 1

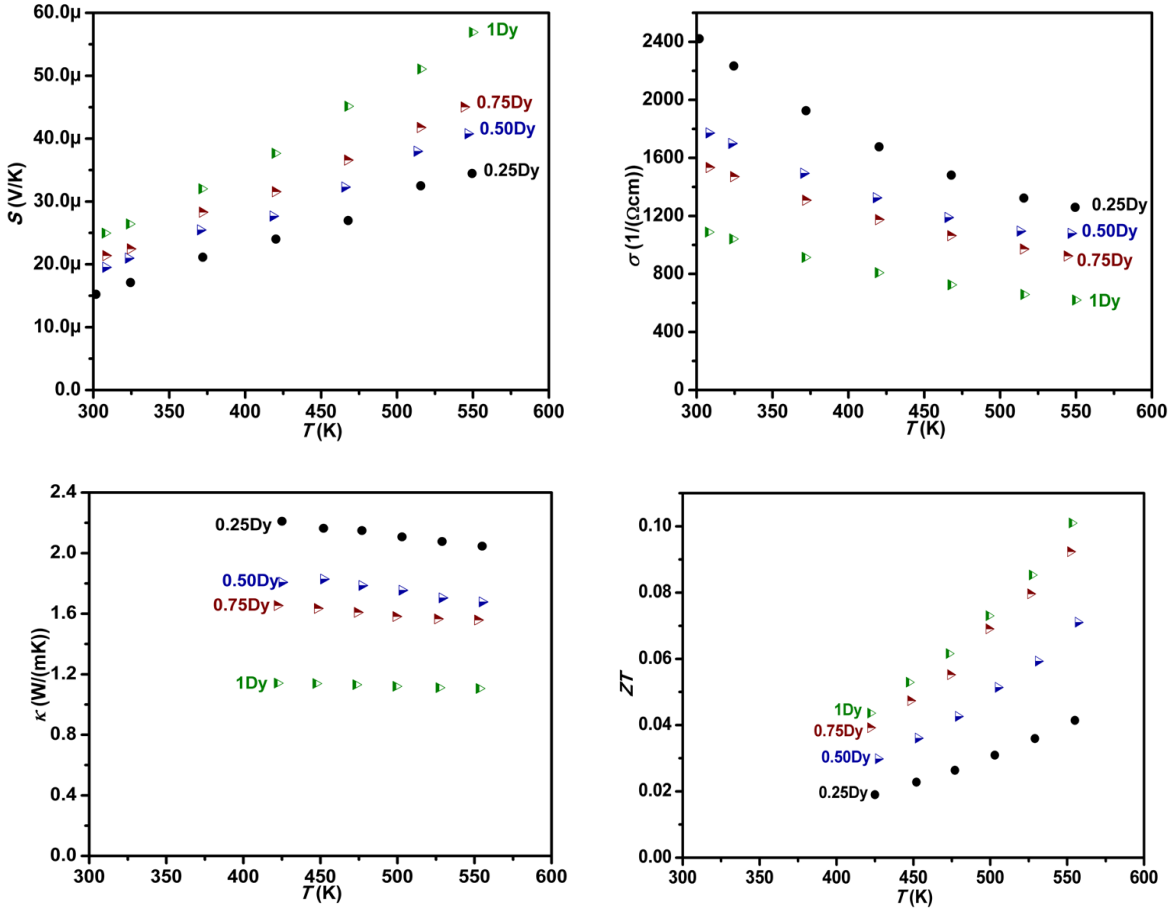

Figure A.19: Thermoelectric properties of $Tl_{10-x}Dy_xTe_6$, $0.25 \leq x \leq 1$

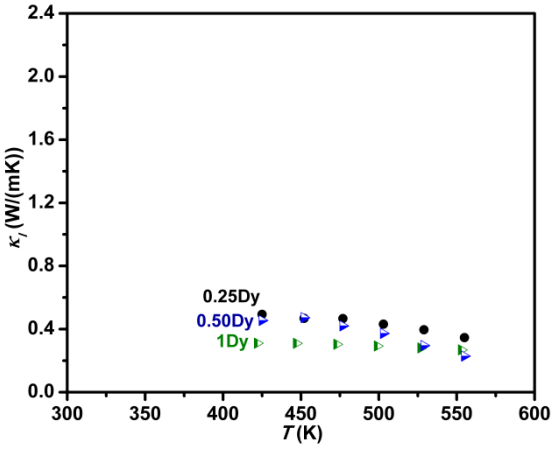

Figure A.20: Plot of κ_l vs. T of $Tl_{10-x}Dy_xTe_6$, $x \sim 0.25$, 0.5 and 1

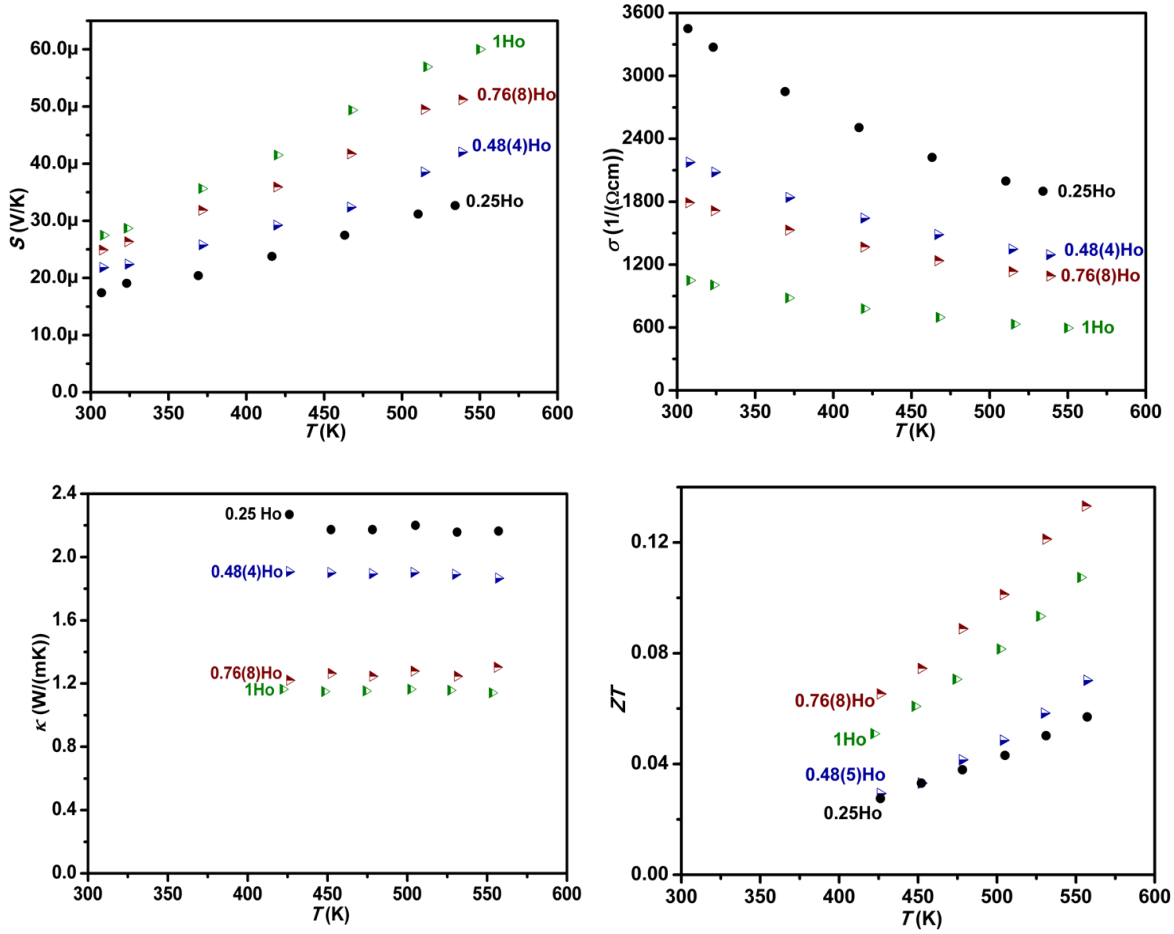

Figure A.21: Thermoelectric properties of $Tl_{10-x}Ho_xTe_6$, $0.25 \leq x \leq 1$

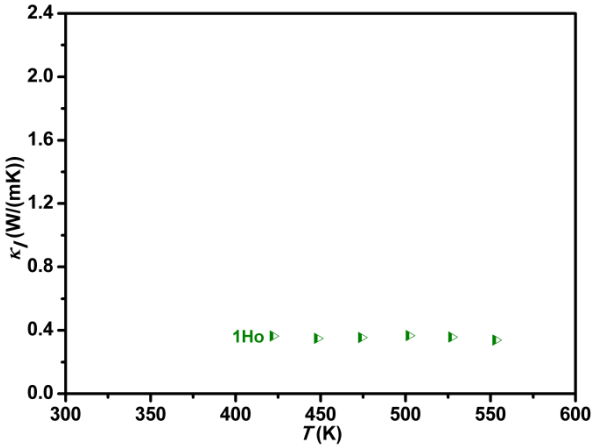

Figure A.22: Plot of κ_l vs. T of Tl_9HoTe_6

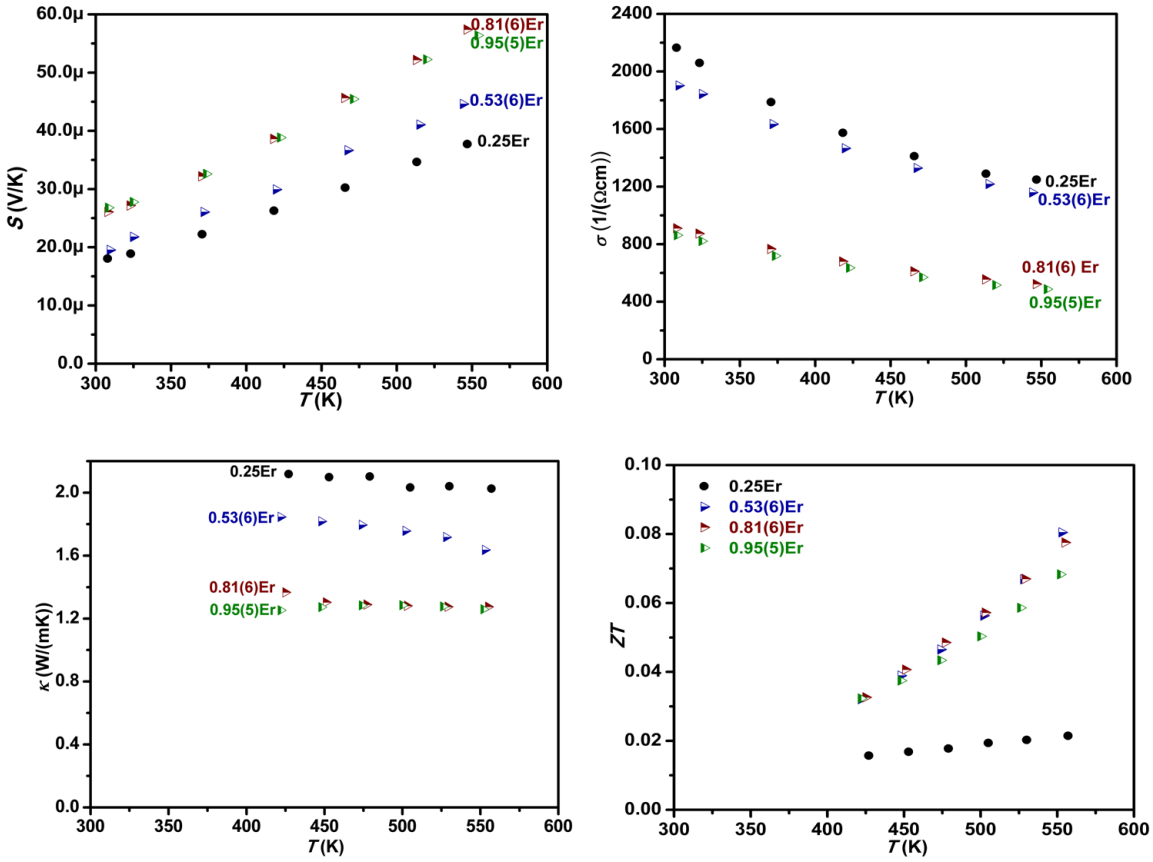

Figure A.23: Thermoelectric properties of $Tl_{10-x}Er_xTe_6$, $0.25 \leq x \leq 0.95$

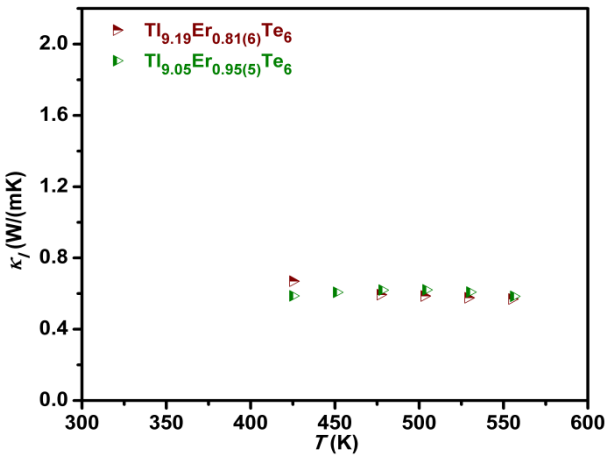

Figure A.24: Plot of κ_l vs. T of $Tl_{10-x}Er_xTe_6$, $x \sim 0.81$ and 0.95

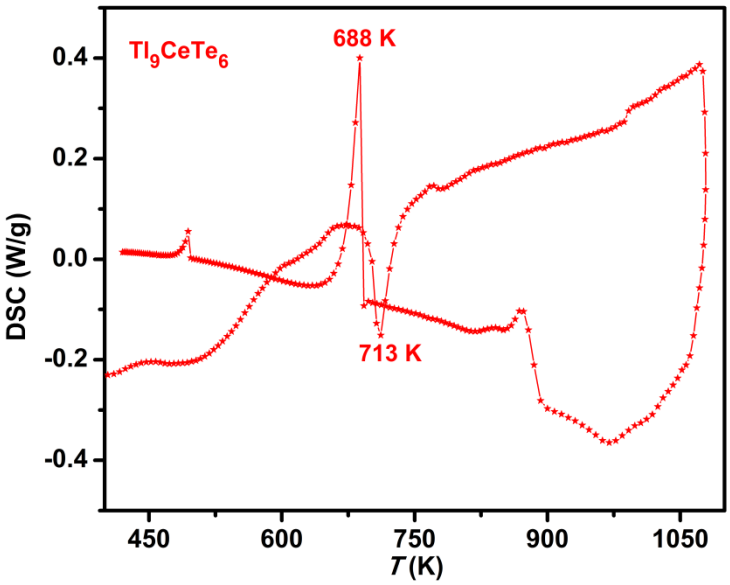

Figure A.25: DSC plot of Tl_9CeTe_6

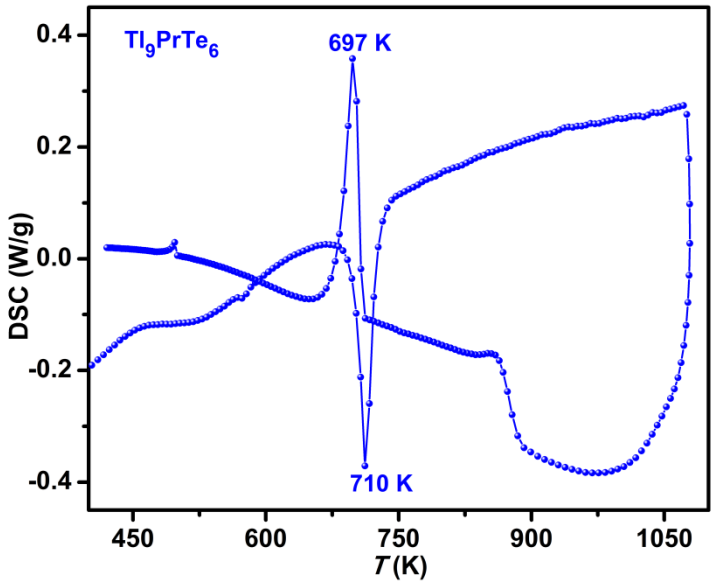

Figure A.26: DSC plot of Tl_9PrTe_6

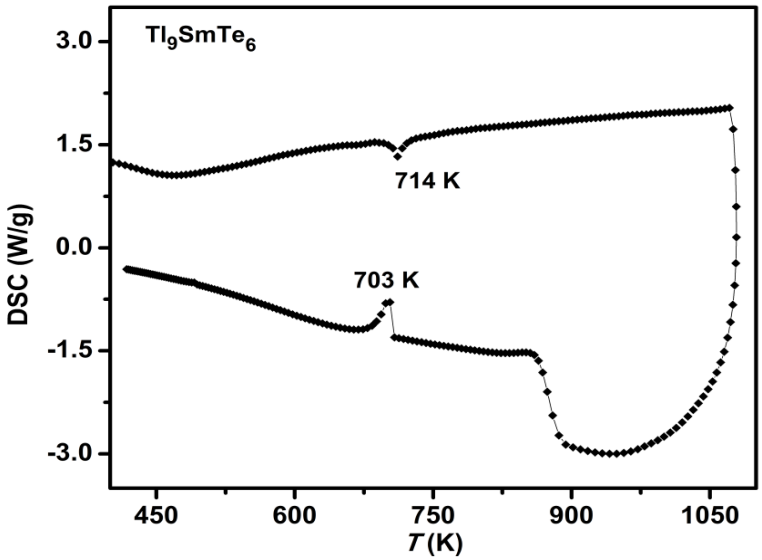

Figure A.27: DSC plot of Tl_9SmTe_6

REFERENCES

1. N. Lior, *Energy* **2008**, 33, 842-857.
2. M. Balat, *Energy Sources* **2010**, B, 50-62.
3. B. I. Ismail and W. H. Ahmed, *Recent Patterns on Electrical Engineering* **2009**, 2, 27-39.
4. S. S. Verma, *Resonance* **2001**, 6, 57-67.
5. K. M. Saqr and M. N. Musa, *Thermal Science* **2009**, 13, 165-174.
6. J. H. Yang and T. Caillat, *Mat. Res. Bull.,* **2006**, 31, 224-229.
7. G. J. Snyder and E. S. Toberer, *Nat. Mater.* **2008**, 7, 105-114.
8. D. M. Rowe, *Thermoelectrics Handbook: Macro to Nano*. CRC Press, Taylor & Francis Group: Boca Raton, FL, USA, 2006.
9. J.-F. Li, W.-S. Liu, L.-D. Zhao and M. Zhou, *NPG Asia Mater.* **2010**, 2, 152-158.
10. L. E. Bell, *Science* **2008**, 321, 1457-1461.
11. E. J. Winder, A. B. Ellis and G. C. Lisensky, *J. Chem. Educ.* **1996**, 73, 940-946.
12. H. Y. Zhang, *Int. J. Refrig.* **2010**, 33, 1187-1196.
13. A. A. Aivazov, Y. I. ShternI., B. G. Budaguan, K. B. Makhrachev and M. Pastor, *Thermoelectric Materials - New Directions and Approaches*, T. M. Tritt; M. G. Kanatzidis; H. B. Lyon.; G. D. Maham, **1997**, 478, 279-284.
14. M. R. Holman and S. J. Rowland, *J. Med. Eng. Technol.* **1997**, 21, 106-110.
15. B. T. Hafsteinsson and A. Geirsson, *Home power* **2004**, 99, 48-53.
16. http://www.thermonamic.com/Generator.html
17. http://www.huimao.com/
18. http://computershopper.com/shoptalk/components/ultra-products-chilltec-thermo-electric-cpu-cooler
19. http://www.tradeeasy.com/supplier/25070/products/p622726/thermoelectric-wine-cooler-and-warmer.html
20. F. J. DiSalvo, *Science* **1999**, 285, 703-706.
21. C. B. Vining, *Nat. Mater.* **2009**, 8, 83-85.
22. M. Xie and D. M. Gruten, *J, Phys. Chem.* **2101**, B, 14339-14342.
23. T. M. Tritt and M. A. Subramanian, *Mat. Res. Bull.*, **2006**, 31, 188-194.
24. http://upload.wikimedia.org/wikipedia/en/d/d8/Seebeck_effect.png

25. http://book.boot.users.btopenworld.com/thermo2_files/image002.jpg
26. Y. Pei, X. Shi, A. LaLonde, H. Weng, L. Chen and G. J. Snyder, *Nature* **2011**, 473, 66-69.
27. G. D. Mahan and J. O. Sofo, *Proc. Natl. Acad. Sci.* **1996**, 93, 7436-7439.
28. N. F. Mott and H. Jones, *The theory of the properties of metals and alloys*. Dover Publications: New York, NY, **1958**.
29. C. E. Housecroft and A. G. Sharpe, *Inorganic Chemistry*. third ed.; Pearson Education Limited: Essex, UK, **2008**.
30. C. Kittel, *Introduction to solid state physics*. John Wiley & Sons, Inc.: New York, **1986**.
31. T. M. Tritt, *Thermal conductivity: Theory, Properties and Applications*. Kluwer Academic/Plenum Publishers: New York, **2004**.
32. L. V. Prokof'eva, A. A. Shabaldin, V. A. Korchagin, S. A. Nemov and Y. I. Ravich, *Semiconductors* **2008**, 42, 1161-1170.
33. J. J. Neely, C. E. Teeter and J. B. Trice, *J. Am. Ceram. Soc.* **1950**, 33, 363-364.
34. J. Francl and W. D. Kingery, *J. Am. Ceram. Soc.* **1954**, 37, 99-107.
35. A. L. Loeb, *J. Am. Ceram. Soc.* **1954**, 37, 96-99.
36. C. B. Vining, *Nat. Mater*. **2008**, 7, 765-766.
37. C. Wood, *Rep. Prog. Phys.* **1988**, 51, 459-539.
38. A. M. Rao, X. Ji and T. M. Tritt, *Mat. Res. Bull.*, **2006**, 31, 218-223.
39. H. Böttner, G. Chen and R. Venkatasubramanian, *Mat. Res. Bull.*, **2006,** 31, 211-217.
40. B. C. Sales, R. Jin and D. Mandrus, *J. Phys. Soc. Jpn.* **2008**, 77, 48-53.
41. S. M. Kauzlarich, S. R. Brown and G. J. Snyder, *Dalton Trans.* **2007**, 2099-2107.
42. E. S. Toberer, A. Zevalkink, N. Crisosto and G. J. Snyder, *Adv. Funct. Mater.* **2010**, 20, 4375-4380.
43. G. S. Nolas, M. Kaeser, R. T. Littleton IV and T. M. Tritt, *Appl. Phys. Lett.* **2000**, 77, 1855-1857.
44. G. S. Nolas, D. T. Morelli and T. M. Tritt, *Annu. Rev. Mater. Sci.* **1999**, 29, 89-116.
45. G. S. Nolas, J. Poon and M. Kanatzidis, *Mat. Res. Bull.*, **2006**, 31, 199-205.

46. L. D. Chen, T. Kawahara, X. F. Tang, T. Goto, T. Hirai, J. S. Dyck, W. Chen and C. Uher, *J. Appl. Phys.*, **2001**, 90, 1864-1868.
47. H. Kleinke, *Chem. Mater.* **2010**, 22, 604-611.
48. A. San-Miguel and P. Toulemonde, *High Pressure Res.*, **2005**, 25, 159-185.
49. P. Rogl, *Formation of clathrates*, ICT, **2005**,443-448.
50. M. Christensen, A. B. Abrahamsen, N. B. Christensen, F. Juranyi, N. H. Andersen, K. Lefmann, J. Andreasson, C. R. H. Bahl and B. B. Iversen, *Nat. Mater.* **2008**, 7, 811-815.
51. D.-Y. Chung, T. Hogan, P. Brazis, M. Rocci-Lane, C. Kannewurf, M. Bastea, C. Uher and M. G. Kanatzidis, *Science* **2000**, 287, 1024-1027.
52. D.-Y. Chung, T. P. Hogan, M. Rocci-Lane, P. Brazis, J. R. Ireland, C. R. Kannewurf, M. Bastea, C. Uher and M. G. Kanatzidis, *J. Am. Chem. Soc.* **2004**, 126, 6414-6428.
53. R. Venkatasubramanian, E. Siivola, T. Colpitts and B. O'Quinn, *Nature* **2001**, 413, 597-602.
54. P. F. P. Poudeu, J. D'Angelo, H. Kong, A. Downey, J. L. Short, R. Pcionek, T. P. Hogan, C. Uher and M. G. Kanatzidis, *J. Am. Chem. Soc.* **2006**, 128, 14347-14355.
55. K. F. Hsu, S. Loo, F. Guo, W. Chen, J. S. Dyck, C. Uher, T. Hogan, E. K. Polychroniadis and M. G. Kanatzidis, *Science* **2004**, 303, 818-821.
56. J. Androulakis, K. F. Hsu, R. Pcionek, H. Kong, C. Uher, J. J. D'Angelo, A. Downey, T. Hogan and M. G. Kanatzidis, *Adv. Mater.* **2006**, 18, 1170-1173.
57. S. R. Brown, S. M. Kauzlarich, F. Gascoin and G. J. Snyder, *Chem. Mater.* **2006**, 18, 1873-1877.
58. H. Matsumoto, K. Kurosaki, H. Muta and S. Yamanaka, *Mater. Trans.* **2009**, 50, 1582-1585.
59. B. C. Sales, B. C. Chakoumakos and D. Mandrus, *Phys. Rev. B: Condens. Matter* **2000**, 61, 2475-2481
60. K. Kurosaki, H. Uneda, H. Muta and S. Yamanaka, *J. Alloys Compd.*, **2004**, 376, 43-48.
61. K. Kurosaki, A. Kosuga and S. Yamanaka, *J. Alloys Compd.*, **2003**, 351, 279-282.

62. K. Kurosaki, A. Kosuga, H. Muta and S. Yamanaka, *Mater. Trans.* **2005**, 46, 1502-1505.
63. K.Kurosaki, A. Kosuga, K. Goto, H. Muta and S. Yamanaka, *Mater. Trans.* **2006**, 47, 1938-1940.
64. k. Kurosaki, K. Goto, H. Muta and S. Yamanaka, *J. Appl. Phys.,* **2007**, 102, 023707-1 - 023707-5.
65. J. W. Sharp, B. C. Sales, D. G. Mandrus and B. C. Chakoumakos, *Appl. Phys. Lett.*, **1999**, 74, 3794-3796.
66. B. Wölfing, C. Kloc, J. Teubner and E. Bucher, *Phys. Rev. Lett.,* **2001**, 86, 4350-4353.
67. B. Wölfing, C. Kloc and E. Bucher, *Mat. Res. Soc. Symp.* **2000**, 626, Z3.4.1-Z3.4.6.
68. I. Schewe, P. Böttcher and H. G. v. Schnering, *Z. Kristallogr.,* **1989**, 188, 287-298.
69. P. Böttcher, T. Doert, C. Druska and S. Bradtmoller, *J. Alloys Compd.,* **1997**, 246, 209-215.
70. K. Kurosaki, K. Goto, A. Kosuga, H. Muta and S. Yamanaka, *Mat. Res. Soc. Symp.,* **2006**, 886, 281-286.
71. A. R. West, *Solid State Chemistry and its applications*. John Wiley & Sons: New York, **1984**.
72. L. Smart and E. Moore, *Solid State Chemistry*. Chapman & Hall: London, UK, **1996**.
73. L. E. Smart and E. A. Moore, *Solid State Chemistry: An Introduction, 3rd ed.* CRC Press: Boca Raton, Fl, **2005**.
74. http://serc.carleton.edu/research_education/geochemsheets/BraggsLaw.html
75. http://chemwiki.ucdavis.edu/Analytical_Chemistry/Intrumental_Analysis/diffraction/Powder_X-ray_Diffraction
76. *SMART: version 4, Siemens Analytical X-ray instruments Inc.* Madison, WI, **1995**.
77. *SAINT: version 4, Siemens Analytical X-ray instruments Inc.* Madison, WI, **1995**.

78. *G. M. Sheldrick, SHELXTL:version 5.12, Seimens ANALYTICAL X-ray systems*. Madison, WI, **1995**.
79. W. Clegg, A. J. Blake, R. O. Gould and P. Main, *Crystal Structure Analysis:" Principle and Practice*. Oxford University Press Inc.: New York, **2001**.
80. R. A. Young, *The Rietveld Method (Ed.: R. A. Young)*. Oxford University Press: New York, **2002**.
81. G. Malmros and J. O. Thomas, *J. Appl. Crystallogr.* **1977**, 10, 7-11.
82. A. C. Larson and R. B. v. Dreele, *Los Alamos National Laboratory: Los Alamos* NM, **2000**.
83. B. H. Toby, *J. Appl. Crystallogr.* **2001**, 34, 210-213.
84. http://www.globalsino.com/micro//micro9999.html
85. http://www.mcswiggen.com/TechNotes/WDSvsEDS.htm
86. R. P. W. Scott, *The Physical Chemistry Resources*. Vol. Book 5: Thermal Analysis.
87. http://pslc.ws/macrog/dsc.htm
88. Power Conversion Efficiency Measuring Instrument Instruction Manual, Model ZEM-3, ULVAC-RIKO, Inc.
89. http://staging.electronics-cooling.com/2002/05/flash-diffusivity-method-a-survey-of-capabilities/
90. S. Saini, R. B. Frankel, D. D. Stark and J. T. Ferrucci, *Am. J. Roentgenol.*, **1988**, 150, 735-743.
91. P. W. Atkins, *General Chemistry*. Scientific American Inc.: New York, USA, **1989**.
92. S. Cotton, *Lanthanoid and Actinide Chemistry*. John Wiley & Sons Ltd: West Sussex, **2006**.
93. É. D. Trémolet, *Magnetism: Materials & Applications*. Spinger Science + Business Media Inc.: New York, NY, USA, **2005**.
94. K. H. J. Buschow and F. R. d. Boer, *Physics of magnetism and magnetic materials*. Springer Publishing Company: New York, USA, **2003**.
95. http://ipc.iisc.ernet.in/~magsquid/5.GIF
96. http://www.wmi.badw.de/methods/squid.htm

97. G. L. M. a. D. A. Tarr, *Inorganic Chemistry*. Pearson Education Inc.: New Jersey, **2004**.

98. R. Hoffmann, *Angew. Chem. Int. Ed. Enhl.* **1987**, 26, 846-878.

99. H. L. Skriver, *The LMTO Method*. Spinger: Berlin, Germany, **1984**.

100. P. Blaha, K. Schwarz, G. H. K. Madesn, D. Kvasnika and J. Luitz, *An Augmented Plane Wave + Local Orbital Program for Calculating Crystal Properties*. Technische Universitat WIEN: Austria, **2001**.

101. P. Hohenberg and W. Kohn, *Phys. Rev.* **1964**, 136, B864-B871.

102. W. Kohn and C. J. Sham, *Phys. Rev.* **1965**, 140, A1133-A1138.

103. O. K. Andersen, *Phys. Rev. B: Condens. Matter,* **1975**, 12, 3060-3083.

104. L. Hedin and B. I. Lundqvist, *J. Phys. C: Solid State Phys.* **1971**, 4, 2064-2083.

105. V. I. Anisimov, F. Aryasetiawan and A. I. Lichtenstein, *J. Phys. : Condens. Matter* **1997**, 9, 767-808.

106. J. E. Huheey, E. A. Keiter and R. L. Keiter, *Inorganic Chemistry: Principles of Structure and Reactivity*. HaperCollins: New York, USA, **1993**.

107. H. Matsumoto, K. Kurosaki, H. Muta and S. Yamanaka, *Materials Transactions* **2009**, 50, 1582-1585.

108. S. Yamanaka, A. Kosuga and K. Kurosaki, *J. Alloys Compd.,* **2003**, 352, 275-278.

109. K. Kurosaki, A. Kosuga and S. Yamanaka, *J. Alloys Compd.,* **2003**, 351, 14-17.

110. I. Schewe, P. Böttcher and H. G. von Schnering, *Z. Kristallogr.* **1989**, 188, 287-298.

111. T. Doert and P. Böttcher, *Z. Kristallogr.* **1994**, 209, 95-95.

112. W. L. Cox, H. Steinfink and W. F. Bradley, *Inorg. Chem.* **1966**, 5, 318-319.

113. C. Janiak and R. Hoffmann, *J. Am. Chem. Soc.* **1990**, 112, 5924-5946.

114. P. Pyykkö, *Chem. Rev.* **1997**, 97, 597-636.

115. R. Cerny, J. M. Joubert, Y. Filinchuk and Y. Feutelais, *Acta Crystallogr. C* **2002**, 58, i63-i65.

116. A. Assoud, N. Soheilnia and H. Kleinke, *J. Solid State Chem.* **2006**, 179, 2707-2713.

117. S. Bangarigadu-Sanasy, C. R. Sankar, A. Assoud and H. Kleinke, *Dalton Trans.* **2011**, 40, 862-867.

118. F. A. Cotton and G. Wilkinson, *Advanced Inorganic Chemistry*. Wiley: New York, **1966**.
119. S. P. Sinha, *Systematics and properties of the Lanthanoids*. D. Reidel Publishing company: Dordrecht, Holland, **1982**.
120. M. B. Babanly, J. C. Tedenac, S. Z. Imamalieva, F. N. Guseynov and G. B. Dashdieva, *J. Alloys Compd.*, **2010**, 491, 230-236.
121. R. J. Hill and L. M. D. Cranswick, *J. Appl. Crystallogr.*, **1994**, 27, 802-844.
122. S. Z. Imamalieva, F. M. Sadygov and M. B. Babanly, *Inorg. Mater.*, **2008**, 44, 935-938.
123. M. Duczmal and L. Pawlak, *J. Alloys Compd.*, **1997**, 262-263, 316-319.
124. J. Goraus, A. Ślabarski and M. Neumann, *J. Alloys Compd.*, **2005**, 401, 189-192.
125. B. Chevalier, J. G. Soldevilla, J. I. Espeso, J. R. Fernàndez, J. C. G. Sal and J. Etourneau, *Physica B* **1999**, 259-261, 44-45.
126. M. E. Danebrock, C. B. H. Evers and W. Jeitschko, *J. Phys. Chem. Solids* **1996**, 57, 381-387.
127. K. Katoh and M. Kasaya, *Physica B* **1993**, 186-188, 428-430.
128. O. K. Andersen, *Phys. Rev. B* **1975**, 12, 3060-3083.
129. W. R. L. Lambrecht and O. K. Andersen, *Phys. Rev. B* **1986**, 34, 2439-2449.
130. P. E. Blöchl, O. Jepsen and O. K. Andersen, *Phys. Rev. B* **1994**, 49, 16223-16233.
131. J. O. Sofo and G. D. Mahan, *Phys. Rev. B* **1994**, 49, 4565-4570.
132. V. I. Anisimov, J. Zaanen and O. K. Anderson, *Phys. Rev. B* **1991**, 44, 943-954.
133. Sandeep, M. P. Ghimire and R. K. Thapa, *Journal of magnetism and magnetic materials* **2011**, 323, 2883-2887.
134. R. C. Albers, N. E. Christensen and A. Svane, *J. Phys. : Condens. Matter* **2009**, 21, 343201-343211.
135. B. N. Harmon, V. P. Antropov, A. I. Liechtenstein, I. V. Solovyen and V. I. Anisimov, *J. Phys. Chem. Solids* **1995**, 56, 1521-1524.
136. X. B. Liu and Z. Altounian, *J. Phys.: Condens. Matter* **2009**, 21, 416002-416008.
137. Z. Huang, L. Ye, Z. Q. Yang and X. Xie, *Phys. Rev. B* **2000**, 61, 12786-12791.
138. Y. Fu, Z. Huang, X. Wang and L. Ye, *J. Phys.: Condens. Matter* **2003**, 15, 1437-1444.

139. A. V. Prokofiev, A. I. Shelykh and B. T. Melekh, *J. Alloys Compd.*, **1996**, 242, 41-44.

140. B. Wölfing, C. Kloc, J. Teubner and E. Bucher, *Phys. Rev. Lett.* **2001**, 86, 4350-4353.

141. S. Yamanaka, A. Kosuga and K. Kurosaki, *J. Alloys Compd.* **2003**, 352, 275-278.

142. J. C. Ronfard Hared, *Solid State Ionics* **2004**, 167, 355-366.

143. J. Adachi, K. Kurosaki, M. Uno and S. Yamanaka, *J. Alloys Compd.*, **2007**, 432, 7-10.

144. W. D. Kingery and M. C. McQuarrie, *J. Am. Ceram. Soc.* **1954**, 37, 67-72.

145. K. Kurosaki, A. Kosuga, K. Goto, H. Muta and S. Yamanaka, *Materials and Technologies for Direct Thermal-to-Electric Energy Conversion*, J. Yang; T. P. Hogan; R. Funahashi; G. S. Nolas, (Eds.) Materials Research Society: Warrendale, **2006**, 886, 349-354.

146. D. M. Babanly, S. V. Askerova, I. M. Babanly and Y. A. Yusibov, *Inorg. Mater.*, **2010**, 46, 17-21.

147. A. H. Edwards, A. C. Pineda, P. A. Schultz, M. G. Martin, A. P. Thompson and H. P. Hjalmarson, *J. Phys.: Condens. Matter* **2005**, 17, L329-L335.

148. P. P. Konstantinov, L. E. SHelimova, E. S. Avilov, M. A. Kretyova and V. S. Zemskov, *Inorg. Mater.*, **2000**, 37, 662-668.

149. G. S. Nolas and D. T. Morelli, *Annu. Rev. Mater. Sci.* **1999**, 29, 89-116.

150. K. Morigaki, *Physics of Amorphous Semiconductors*. Imperial College Press: London, UK, **1998**.

151. I. A. Smirnov, V. S. Oskotskii and L. S. Parfeneva, *J. Less-Common Met.*, **1985**, 111, 353-357.

152. S. H. D. Moore, L. Deakin, M. J. Ferguson and A. Mar, *Chem. Mater.*, **2002**, 14, 4867-4873.

153. B. Coqblin, M. D. Núñez-Regueiro, A. Theumann, J. R. Iglesias and S. G. Magalhães, *Philos. Mag.*, **2006**, 86, 2567-2580.

154. A. Barla, J. P. Sanchez, J. Derr, B. Salce, G. Lapertot, J. Flouquet, B. P. Doyle, O. Leupold, R. Ruffer, M. M. Abd-Elmeguid and R. Lengsdorf, *J. Phys. Condens. Matter*, **2005**, 17, S837-S848.

155. A. Barla, J. Derr, J. P. Sanchez, B. Salce, G. Lapertot, B. P. Doyle, R. Ruffer, R. Lengsdorf, M. M. Abd-Elmeguid and J. Flouquet, *Phys. Rev. Lett.,* **2005**, 94, 166401-1-166401-4.

156. N. N. Lubinskii, L. A. Bashkirov, A. I. Galyas, S. V. Shevchenko, G. S. Petrov and I. M. Sirota, *Inorg. Mater.,* **2008**, 44, 1015 - 1021.

157. Y. Liu, L. Chen, L.-H. Li and L.-M. W, *Inorg. Chem.*. **2008**, 47, 11930 - 11941.

158. R. L. Carlin, *Magnetochemistry*. Springer, New York, **1986**.

159. G. Amoretti and J. M. Fournier, *J. Magn.Magn.Mater.* **1984**, 43, L217 - L220.

160. S. Cirafici, F. Canepa, P. Manfrinetti and M. Napoletano, *J. Alloys Compd.*, **2001**, 317-318, 550-555.

161. D. Niepmann, R. PÖttgen, B. Künnen and G. Kotztba, *J. Solid State Chem.*, **2000**, 150, 139-144.

162. P. Rogl, B. Chevalier, M. J. Besnus and J. Etourneau, *J. Magn.Magn.Mater.* **1989**, 80, 305-310.

163. M. Janatova, J. Vejpravova, M. Divis and V. Sechovsky, *Physica B: Condensed Matter* **2008**, 403, 2338-2343.

164. M. H. Jung and A. H. Lacerda, *Phys. Rev. B: Condens. Matter*, **2002**, 65, 132405-1 - 132405-3.

165. K. Ghosh, S. Ramakrishnan, S. K. Dhar, S. K. Malik and G. Chandra, *Phys. Rev. B: Condens. Matter,* **1995**, 52, 7267-7277.

166. A. D. Christianson, E. D. Bauer, J. M. Lawrence, P. S. Riseborough, N. O. Moreno, P. G. Pagliuso, J. L. Sarrao, J. D. Thompson, E. A. Goremychkin, F. R. Trouw, M. P. Hehlen and R. J. McQueeney, *Phys. Rev. B: Condens. Matter,* **2004**, 70, 134505-1-134505-9.

167. S. Takaaki, G.-Y. Adachi and J. Shiokawa, *J. Appl. Phys.,* **1977**, 48, 379-381.

168. D. A. Sokolv, M. S. Kim, M. C. Aroson, C. Henderson and P. W. Stephens, *Los Alamos National Laboratory* **2007**, 1-5.